In vivo Electrochemical Sensors

by

Robert K. Franklin

A dissertation submitted in partial fulfillment
of the requirements for the degree of
Doctor of Philosophy
(Electrical Engineering)
in The University of Michigan
2010

Doctoral Committee:

Professor Richard B. Brown, Chair
Professor Yogesh B. Gianchandani
Professor Daryl R. Kipke
Professor Mark E. Meyerhoff
Professor Kensall D. Wise

2010

Acknowledgements

I would like to thanks my wife, Christina, without whose constant support and encouragement I never would have finished this work and Dr. Richard Brown whose support and advice made this work possible.

Portions of this work were also funded by an NSF Graduate Research Fellowship and the NSF sponsored Engineering Research Center for Wireless Integrated Microsystems (WIMS) under award number EEC-9986866.

Table of Contents

List of Figures

List of Tables

Chapter 1

Introduction

Electrical and chemical signals are generally inextricable at every level in the nervous system. In the myriad of interconnected sub-systems, chemical events and electrical events interact in complex cascades (see Fig. 1.1). While microelectrodes are reasonably

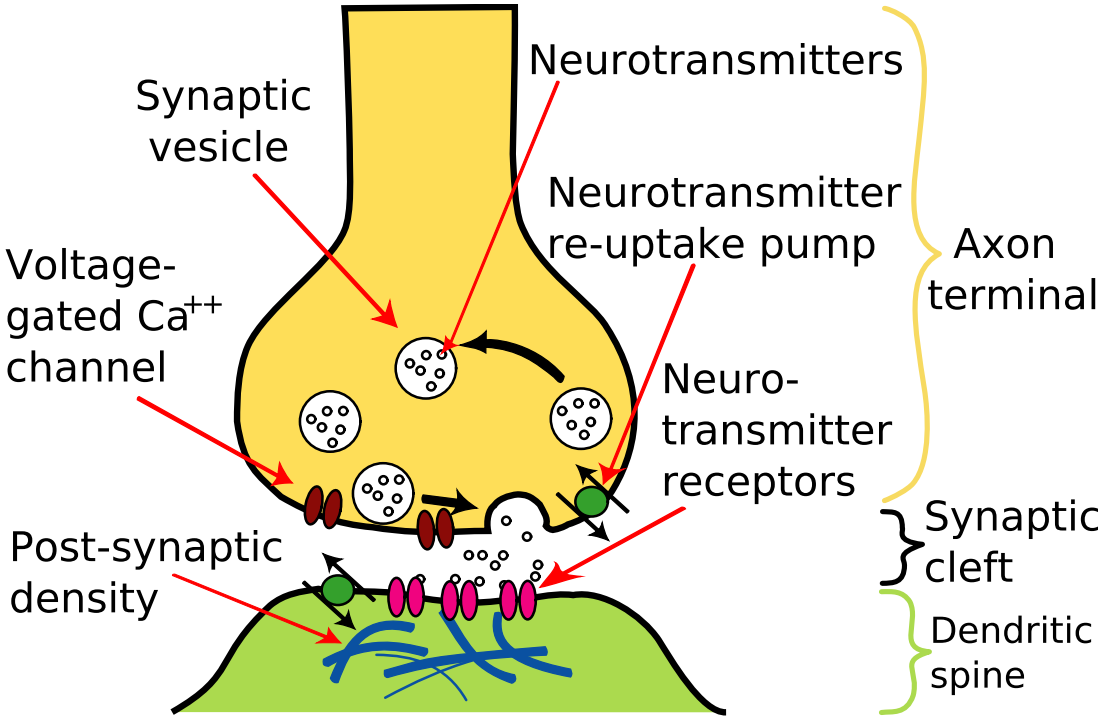

Figure 1.1: Synapse. Illustration of a neuron synapse showing synaptic cleft and neurotransmitter pathways. (Illustration by Nrets. License Creative Commons Attribution ShareAlike 3.0)

well developed for many electrophysiological measurements and chemical sensors and delivery systems are in active development, few devices to date have demonstrated the ability to establish multiple electrical and chemical interfaces with brain tissue in a specific, controlled, and chronic manner. Yet this multi-modal functionality is likely to be an enabling technology for progressively more powerful investigations at the intersection of neurophysiology, neuropharmacology, and molecular biology. The overall objective of this work is to broaden the field of neurochemical sensing by developing and characterizing materials and circuits designed to enable concurrent neurochemical and neurophysiological sensing at highly localized areas of the brain.

This project rests on an existing platform of neural probe technology that has been developed over the last 30 years at the University of Michigan. The first prototypes of the Michigan style intracortical neural probe arrays were developed by Wise et al. in the 1970's, culminating in the design of a deep boron diffusion defined probe in 1985. In many labs throughout the world, these probes are the gold standard for electrophysiology experiments. Since 1994 they have been distributed by the Center for Neural Communication Technology (CNCT), which was originally funded as a P41 Biotechnology Resource Center by the NIH/NCRR (National Institutes of Health/National Center for Research Resources). Their development has led to several key discoveries in the areas of hearing, vision, and memory. Inspired by their success, several labs have attempted to either duplicate the fabrication process or develop new processes for producing similar probes. Additionally, since July of 2004 the probes have been available commercially through NeuroNexus, a successful spin-off from the University of Michigan.

Given the tremendous success of the Michigan style neural probes, this work proposed to extend the capabilities of the Michigan probe platform by developing neurochemical sensors that can be fully integrated with the probe technology's present modalities: electrical recording, stimulation, and fluid delivery. The proposed work included components of engineering design and development, as well as experimental analysis and validation. In particular, the work presented in this dissertation had two specific aims:

Aim 1: Fabricate and characterize multi-modal neural probes for sensing electroactive neurochemicals. This aim was directed at integrating currently available amperometric techniques for sensing electroactive neurochemicals with existing silicon probe technology. The primary tasks included:

1. Designing and fabricating brain probes capable of in vivo neurochemical detection.

2. Investigating the suitability of various electrode site materials and geometries for neurochemical detection.

3. Characterizing the developed probes through in vitro and in vivo experiments.

The primary goal of this aim was a multi-modal silicon probe that specifically senses electroactive neurochemicals such as dopamine and serotonin, as well as their respective metabolites in acute experiments.

Aim 2: Design and fabricate readout circuitry for the probes implementing functions necessary for multi-modal recordings. This aim was directed at improving device performance through tight integration of active circuits with the probes. The primary tasks included:

1. Designing and fabricating circuitry necessary to perform chemical recordings in vivo.

2. Investigating various technologies available for integrating circuits with micro-machined silicon probes.

3. Characterizing the developed designs through in vitro and in vivo experiments. The primary outcome of this aim is an analog circuit design capable recording from the chemical domain.

The major findings of this dissertation are the development and characterization of a multi-modal neural probe platform for concurrent neurophysiological recording and sensing of select neurochemicals, providing a comprehensive first step in bridging electro-physiology and neurochemistry in the Michigan silicon probe technology. The long-term goal is to develop integrated microdevices that will provide duality of sensing/actuation between the electrical and chemical domains for acute and chronic animal preparations.

Chapter 2

Electrochemical Review[1]

A basic knowledge of electrochemical theory is needed to understand or design liquid chemical sensors. While an in-depth discussion of this topic is beyond the scope of this dissertation, the basic concepts of electrochemistry will be presented here in sufficient detail to allow the reader to grasp the principles of operation behind these sensors. For a more detailed explanation of the electrochemical theory, there are several excellent texts devoted to the subject, including [Kissinger96] and [Bard00].

2.1 The electrode-electrolyte interface

All electrochemical measurements rely on the behavior of analyte in a heterogeneous environment. When an electrode is placed in a solution, a phase boundary exists between the solid electrode and the bulk solution. Additionally, a barrier to charge transfer exists between the two phases due to a difference in charge carriers (charge is carried by electrons in solid conductors and ions in solutions). Charge can only cross this barrier when a molecule in the solution is either reduced, thereby receiving an electron from the

1. Most of this chapter was originally published as a book chapter in [Franklin07]. The text and some of the figures have been updated to flow with the dissertation. Many of the figures that were published in that chapter (and are subsequently reprinted here) were originally from [Strong04] and are reused here with permission from the original author.

electrode, or oxidized by giving up an electron to the electrode. A generic reduction-oxidation (redox) reaction follows the form

$$O + ne^- \Leftrightarrow R \qquad (2.1)$$

where ***O*** is the oxidized form of the analyte, ***R*** is the reduced form, and *n* is the number of electrons (e^-) exchanged in the reaction. This reaction has two components, a forward reaction and a reverse reaction, and the reaction may be either reversible or irreversible. If the reaction is reversible, then the reaction can proceed in both directions, and neither ***O*** nor ***R*** is ever present without the other species being present, although the amount of one of the two reactants may be very small. Reversible reactions eventually reach an equilibrium point where the rate of the forward reaction equals the rate of the reverse reaction. Irreversible reactions proceed in only one direction and given enough time, one of the two reactants (either ***O*** or ***R***) will be completely consumed by the reaction. Eq. 2.1 represents the simplest form of a redox reaction. In practice, more complex reactions involving three or more products with intermediate reactions are often encountered. However, for simplicity's sake, a discussion of these more complex reactions is omitted from this review.

2.2 The Nernst equation

A result of the barrier to charge transfer between electrodes and ions in solution is that almost all electrodes, when placed in solution, develop a surface charge. At equilibrium, the potential difference, E_M, that develops between the electrode and solution depends upon the electrode material and the concentration of the analyte in the solution. This potential is known as the Nernst Potential and is given by the Nernst equation,

$$E_M = E^0 + \frac{RT}{nF} \ln\left(\frac{C_o}{C_R}\right), \qquad (2.2)$$

where E^0 is the standard potential of the reaction, R is the molar gas constant (8.3145 J K^{-1} mol^{-1}), T is temperature, n is the number of electrons exchanged in the reaction, F is Faraday's constant (9.6485×10^4 C mol^{-1}), C_o is the concentration of the oxidized form of the species, and C_R is the concentration of the reduced form of the species [Bard00]. In this form, the Nernst relationship applies only to dilute solutions; in more concentrated solutions, the concentrations, C_R and C_o, must be replaced by their respective chemical activities. For solid phase reactants (such as a metal electrode placed in solution), $C = 1$. At $T = 298$ K the Nernst equation can be rewritten in a simpler form using the common log instead of the natural log:

$$E_M = E^0 + \frac{59.2 \text{ mV}}{n} \log\left(\frac{C_o}{C_R}\right). \qquad (2.3)$$

The standard potential of the electrode, E^0, needs special consideration. Since direct measurement of the potential of a solution is impossible, all electrode potentials must be given relative to the potential of a second electrode. The electrode normally used for measuring standard values for E^0 is the Normal Hydrogen Electrode (NHE) which has an E^0 defined to be 0 V. E^0 values for a few common electrode materials are listed in Table 2.1. For a more comprehensive table of values, the reader is directed to the many extensive texts on the subject such as [Bard01] and [Sawyer95]. If an electrode other than the NHE is used, the E^0 value used in calculating the Nernst potential must be adjusted to include the additional potential due to the E^0 of the measurement electrode.

The Nernst equation relates the potential between an electrode and the surrounding solution to a simple logarithmic ratio of two species in solution. For metal electrodes, one species is the metal at the surface of the electrode and the other is the oxidized form of the

Table 2.1: Standard potentials for several common electrode materials

Electrode Half Reaction	E^0 for reaction (V)
$Au^+ + e^- \Leftrightarrow Au(s)$	1.691
$Hg^{2+} + 2\ e^- \Leftrightarrow Hg(l)$	0.852
$Ag^+ + e^- \Leftrightarrow Ag(s)$	0.799
$Hg_2Cl_2 + 2\ e^- \Leftrightarrow 2\ Hg + 2\ Cl$	0.268
$AgCl(s) \Leftrightarrow Ag(s) + Cl^-$	0.222
$2\ H^+ + 2\ e^- \Leftrightarrow H_2(g)$	0.000

metal ion in solution. For example, when a copper electrode is placed in a solution containing 0.02 M Cu^{2+}, the potential difference that exists between the metal and solution phases can be calculated using the Nernst equation. $Cu^{2+} + 2e^- \Leftrightarrow Cu(s)$ describes the redox reaction between the two reactants. E^0 for the copper electrode is 0.339 V. Using Eq. 2.3 with $n = 2$, $C_O = 0.02$ and $C_R = 1$ the value of E_M can be calculated to yield a value of 0.239 V.

The Nernst equation is foundational for the electrochemical techniques described in this chapter. Potentiometric sensors measure the value of E_M and use the measured value of E_M to determine the ratio of C_O to C_R. Voltammetric sensors control the value of E_M, and drive the value of the ratio of C_O to C_R to either infinity or zero and then measure the current resulting from the associated redox reaction.

2.3 The capacitive double layer

Under equilibrium conditions, no net current flows across the solid-liquid interface and a charge builds up on both sides of the interface in much the same way as charge gathers on the two plates of a parallel plate capacitor. On the electrode side of the interface, all

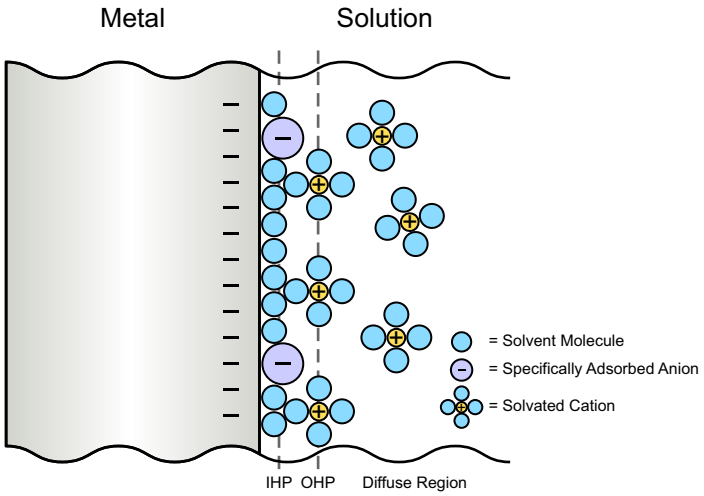

Figure 2.1: Electrical double layer. Depiction of the electrical double layer that builds up at the electrode solution interface when a metal is placed in solution. In the solution there are three distinct layers: the Inner Helmholtz Plane (IHP), the Outer Helmholtz Plane (OHP), and the diffuse layer.

of the charge gathers at the surface of the electrode. However, in a solution, the charge carriers are ions, not electrons, and ions cannot pack as densely as the electrons in a conductor. In order to counterbalance the charge on the electrode and preserve charge neutrality, ions pack as densely as possible forming a dense layer of ions near the surface of the electrode known as the capacitive double layer (see Fig. 2.1). The ions composing the capacitive double layer are normally grouped into three distinct regions. The first region, known as the Inner Helmholtz Plane (IHP), is composed primarily of polar water molecules and specifically adsorbed anions. The second layer is composed mostly of fully hydrated cations and is called the Outer Helmholtz Plane (OHP). The final region, the diffuse layer, extends from the OHP to the bulk of the solution and is composed of hydrated anions and cations. The capacitive double layer is very thin (normally less than 1 μm and often less than 0.1 μm) and functions similarly to a capacitor with a capacitance, C_{dl}, of approximately 10 to 100 μF cm^{-2} of electrode surface. However, the behavior of the dou-

ble layer capacitance varies from that of a true capacitor in that the capacitance of the layer may vary with the external potential applied to the system.

2.4 Polarizable and non-polarizable electrodes

The relative ease with which electrons transfer across the electrode-solution interface defines whether the electrode is considered polarizable or non-polarizable. Electrodes for which the electron transfer takes very little energy are referred to as being non-polarizable, while those for which the transfer is nearly impossible are referred to as polarizable. No electrode is purely polarizable or non-polarizable. Real electrodes fall somewhere in between the two extremes; however, close approximations of these ideal electrodes do exist.

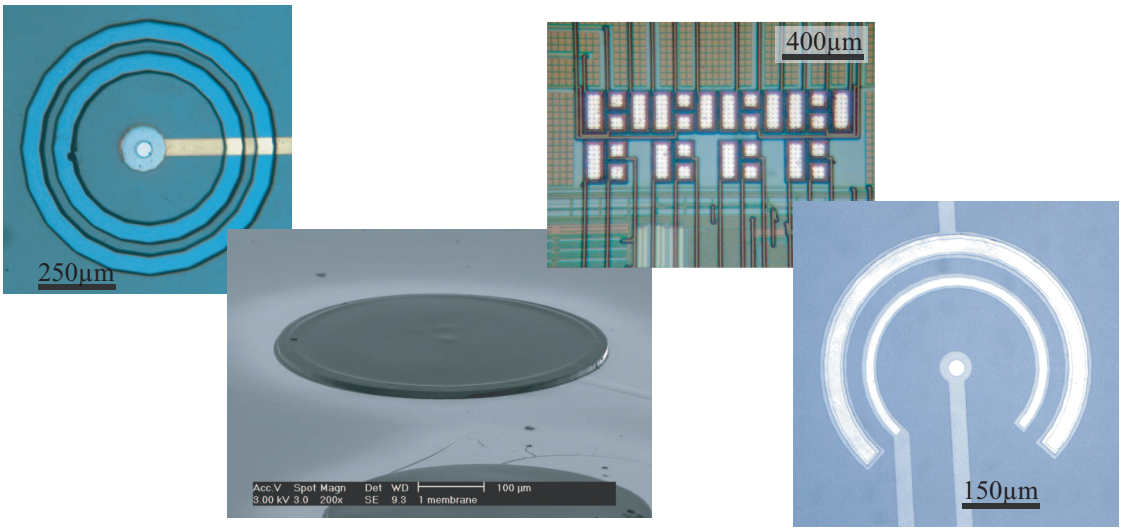

Figure 2.2: Several example electrodes. From left to right: A platinum voltammetric electrode with SU-8 well for enzyme selective coatings; an SEM of a polymer-based ISE membrane using an SU-8 ring for containment during membrane dispense (Nam, H. *et al.* 2003 used with permission); an active voltammetric array with Pt working and counter electrodes and Ag/AgCl reference electrodes fabricated on top of CMOS circuitry; and a voltammetric sensor with Pt working (inner) and counter (outer) electrodes and integrated Ag/AgCl reference electrode (middle).

Polarizable electrodes pass very little current when a voltage is applied across them. Most noble metals such as platinum and gold are examples of nearly ideal polarizable electrodes. An ideal polarizable electrode behaves similar to an electrical capacitor with one plate being the electrode and the other consisting of the ions and solvent molecules collected near the electrode surface which form the capacitive double layer.

Non-polarizable electrodes are characterized by a very fast electrode reaction that allows the electrode's potential to remain close to the equilibrium potential even when current is flowing through the electrode. The most common nearly ideal non-polarizable electrode is the Ag/AgCl electrode which is formed by coating a silver electrode with silver chloride. An ideal non-polarizable electrode behaves similarly to an electrical resistor, with the resistance modeling the difficulty of the transfer of electrons across the interface. In practice, most non-polarizable electrodes are only non-polarizable for small current densities (< 10 $\mu A/mm^2$).

2.5 The electrochemical cell

The apparatus used to carry out an electrochemical experiment is known as an electrochemical cell. Most electrochemical cells consist of either two or three electrodes (see Fig. 2.3). Two electrodes are always present in every electrochemical cell, the indicator or working electrode and the reference electrode. Normally, the reaction at the indicator/working electrode is of interest. The conditions at this electrode are carefully controlled in order to favor detection of a single analyte. If little or no current flows through the electrode as in potentiometry, then this electrode is referred to as the indicator

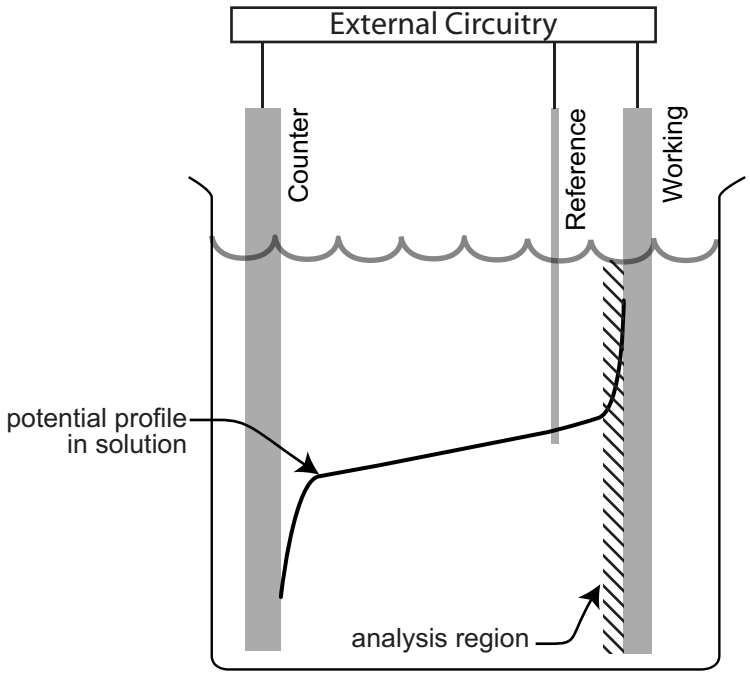

Figure 2.3: Three electrode electrochemical cell. Electrochemical cells normally contain at least two electrodes: the working and reference electrodes. In experiments that draw significant amounts of current, a third electrode, the counter electrode may be added to the cell. The profile of an applied potential is also depicted. Most of the potential drop occurs at the surface of the electrodes. However, when current is flowing between two of the electrodes, there may also be a potential drop in the bulk of the solution due to the resistance of the solution.

electrode. In cases where significant current flows through the electrode as in voltammetry, the electrode is called the working electrode [McNaught97].

The second electrode, the reference electrode, is designed to develop a well defined and reproducible potential when placed in solution. A good reference electrode should be stable over long periods of time and should show very little hysteresis when small currents are passed through it or after temperature cycling [Sawyer95]. The NHE discussed previously is a reference electrode that is formed by bubbling hydrogen across the surface of a platinum electrode. However, due to the complexity of the NHE, self-contained reference electrodes such as the saturated calomel electrode (SCE) and the Ag/AgCl electrode are more commonly used. These self-contained reference electrodes

normally consist of an inner element (either Hg/Hg_2Cl_2 (calomel) or Ag/AgCl) in an appropriate filling solution (often saturated KCl) connected to the external solution by a liquid junction such as a capillary or porous glass frit [McNaught97]. Of these two electrodes, the Ag/AgCl electrode is used almost exclusively in microsystems and there is an extensive body of literature describing the manufacture and characterization of miniature Ag/AgCl electrodes [Bousse86, Dendo94, Huang02, Strong04].

The third electrode, the counter or auxiliary electrode, is normally used with methods that involve a significant current flow through the working electrode. This electrode is normally significantly larger than the working electrode and made from a polarizable, inert material such as platinum. The only purpose of the counter electrode is to provide a complete circuit allowing current to flow between the working electrode and the counter electrode as reference electrodes are not normally well suited to sourcing or sinking significant amounts of current due to non-idealities (e.g. concentration polarization effects can cause shifts in the reference electrode's potential)

2.6 Voltammetry

Many chemical species are electroactive and will be either reduced or oxidized when an electrical potential is applied between a set of electrodes immersed into a solution containing the species. These redox reactions transfer electrons, generating a current flow between the electrodes through the solution. This current, referred to as the faradaic current, i_f, is related to the concentration of the material undergoing the redox reaction by the equation:

$$i_f = -nFAD\left(\frac{\partial C(x,t)}{\partial x}\right)\Bigg|_{x=0}, \qquad (2.4)$$

where A is the area of the electrode involved in the reaction, D is the diffusion coefficient, and $C(x,t)$ is a function describing the concentration of analyte at a distance x from the electrode at time t.

2.6.1 Principal of operation

To perform a voltammetric analysis, an excitation voltage is typically applied between two electrodes, and the current flowing through the cell is measured. Redox reactions must occur at both of the electrodes in order to support the current flow; however, only the reaction at the working electrode is important. In most voltammetric analyses, the working electrode is a polarizable electrode, and the test solution is a strong electrolyte and thus a good ionic conductor. If the test solution is not a strong electrolyte, a background electrolyte such as NaCl may be added to increase conductivity. Under these conditions, the voltage applied to the solution is primarily dropped across the double layer. Since the double layer at the working electrode is extremely thin («1 μm), large electrical fields are developed in this area, providing the energy necessary to cause electron transfer and to drive the resulting redox reaction of the analyte material.

As discussed previously, a generic redox reaction follows the form described by Eq. 2.1 and the applied potential at which the rates for the forward and reverse reactions are equal and no net current flows in the cell is determined by the Nernst equation (Eq. 2.2). If an external voltage is applied to the cell using the counter electrode, the forward and reverse rates for the redox reaction change, resulting in an increase of either $\boldsymbol{O}$ or $\boldsymbol{R}$ at the surface of the electrodes and a net current flow. Although Eq. 2.2 applies only to a system at equilibrium, when the cell is driven away from equilibrium, the basic relation-

ship described by Eq. 2.2 still holds and the approximate ratio of ***O*** to ***R*** can be found by rearranging terms to arrive at:

$$\frac{C_O}{C_R} = \exp\left(\frac{(E^0 - E)nF}{RT}\right) \qquad (2.5)$$

From this relation, it is apparent that the input voltage required to push the reaction entirely to one side would be infinite. However, since the relationship is logarithmic, the change from having nearly all ***O*** to nearly all ***R*** at the surface is a very small change in voltage. In fact, if the material exhibits a single electron reaction, an E that is only 177mV greater than E^0 is large enough to make the ratio of one material one thousand times greater than the other at the surface of the electrode [Kissinger96].

The rate at which the reaction proceeds and the magnitude of the faradaic current that flows is controlled by: the potential applied between the working and counter electrodes; the electron transfer kinetics of the redox reaction; adsorption of ions on the surface of the electrode; and mass transfer of reactant to the surface of the electrode and product away from the electrode. Mass transfer occurs due to convection, diffusion, and migration. If the cell is mechanically isolated from vibration, mass transfer due to convection can be mostly ignored, and if the background ionic strength of the solution is at least two orders of magnitude larger than that of the analyte, then most of the ionic current will be carried by background ions and mass transfer due to migration can also be ignored. Assuming that mass transfer occurs mostly due to diffusion and that the diffusion of analyte to the electrode surface dominates the other rate controlling steps, a closed form solution of Eq. 2.4 can normally be found that approximates the relationship between the concentration of the analyte and the observed faradaic current.

2.7 Methods

The remainder of this chapter describes several of the voltammetric methods most commonly used with microfabricated sensors. All of these methods adhere to the principles outlined in the preceding paragraphs, but differ in the excitation waveforms applied to the cell. The simplest method, chronoamperometry, which will be presented first, consists of a single voltage step. After chronoamperometry is presented, an analysis of more complex methods such as linear sweep voltammetry, square wave voltammetry, and anodic stripping voltammetry will be presented.

2.7.1 Chronoamperometry

Chronoamperometry is one of simplest voltammetric methods, and yet, it is one of the most frequently used voltammetric methods. Chronoamperometry, in its most basic form, consists of applying a single voltage step at time t_0 and then measuring the current that results from the applied potential. The simplicity of chronoamperometry makes it an ideal technique to analyze as an example of a basic voltammetric operation.

Consider a simple electrochemical cell consisting of a working electrode, a counter electrode, and a beaker of solution containing only the oxidized form of the analyte, ***O***, at a concentration of C_O^*. An initial voltage is applied between the working and the counter electrode such that no electrochemical reactions occur at the working electrode surface and no net current flows in the cell. At time t_0, the applied potential is stepped to a new voltage, E_a, that is 177 mV more negative than E^0, causing almost all of the ***O*** at the surface of the electrode to be instantaneously reduced to ***R***. Any additional ***O*** that arrives at the surface of the electrode via diffusion is immediately reacted so that the concentration of ***O*** at the surface of the electrode is essentially 0. After a period of time, t_s, the applied

potential is stepped back to a voltage that allows the ***R*** at the electrode surface to oxidize back to ***O***, and the experiment is concluded.

If the electrode is much larger than the molecules of ***O*** and if the volume of solution is large compared to the exposed area of the electrode, then a one dimensional approximation may be used. In this case, the concentration profile $C_O(x, t)$ in the solution during the period where the applied voltage is E_a will approximate the series of curves illustrated in Fig. 2.4. During the experiment, the concentration of ***O*** at the surface of the electrode, $C_O(\overline{0, t})$, is essentially zero while the concentration of ***O*** in the bulk solution, $C_O(\overline{\infty, t})$, remains at the original concentration, C_O^*. Unreacted ***O*** diffuses down the concentration gradient to the surface of the electrode where it gains an electron. As time passes, the region depleted of ***O*** by the reaction at the electrode extends deeper into the solution. The thickness of this depletion region is proportional to the diffusion coefficient, *D*.

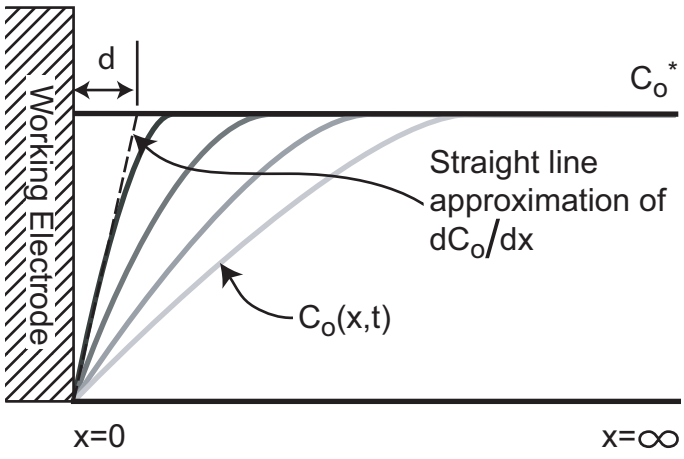

Figure 2.4: Concentration profile. Concentration profile of *O* at various times after the application of E_s. Note that the slope of the concentration profile can be approximated by a straight line.

The amount of charge transferred during the reaction, Q, is related to N, the number of moles of ***O*** reduced to ***R***, by the relationship

$$Q = nFNA. \tag{2.6}$$

Differentiating Q with respect to time, we arrive at an equation for the faradaic current flowing through the electrode at time t

$$i_f = \frac{dQ}{dt} = nFA\left.\frac{\partial N}{\partial t}\right|_{x=0}. \tag{2.7}$$

Material is only diffusing along the x-axis, so by Fick's law of diffusion in one dimension:

$$\left.\frac{\partial N}{\partial t}\right|_{x=0} = -D\left(\frac{\partial C(x,t)}{\partial x}\right)\Bigg|_{x=0}. \tag{2.8}$$

Substituting Eq. 2.8 into Eq. 2.7 results in Eq. 2.4 which was presented in the introduction to this section:

$$i_f = -nFAD\left(\frac{\partial C(x,t)}{\partial x}\right)\Bigg|_{x=0}.$$

The important thing to stress in Eq. 2.4 is that i_f is proportional to the slope of the concentration gradient at the surface of the working electrode and not to the applied voltage. As long as E_a is large enough to convert all of the ***O*** at the surface of the electrode to ***R***, then the current that flows will be independent of E_a. If a straight line approximation for $C_O(x,t)$, as shown in Figure 2.4, is used, then the slope at the electrode is C_O^*/d. Substituting this into Eq. 2.4 gives an approximate relation for the current of

$$i_f \approx nFAD\left(\frac{C_O^*}{d}\right). \tag{2.9}$$

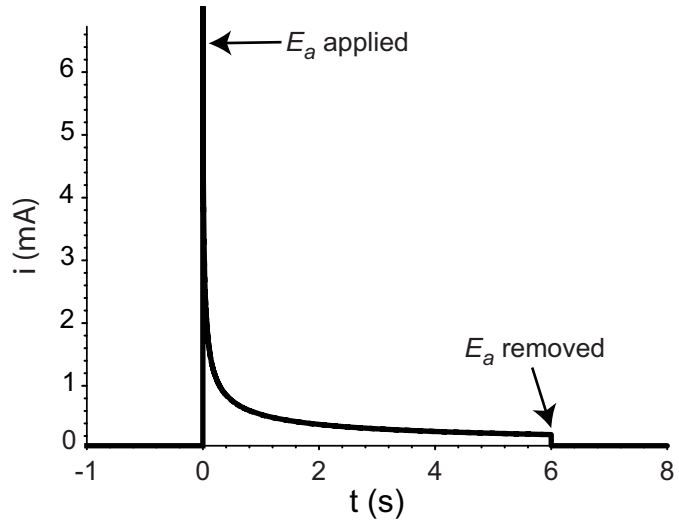

Figure 2.5: Ideal chronoamperometric current. Ideal chronoamperometric current response to step of E_a. Plot assumes a concentration of 1 mM, electrode area 1 cm^2, diffusion coefficient of 10^{-6} cm^2 s^{-1}, and n=1.

While only an approximation, a straight line estimate of a concentration profile is often instructive as to the behavior of a voltammetric system, especially for more complex cases. In this case however, the actual solution of Eq. 2.4 can be found by applying the boundary conditions $C_O(0, 0) = C_O^*$, $C_O(0, t) = 0$, and $C_O(\infty, t) = C_O^*$ providing

$$i_f(t) = \frac{nFAC_O^*\sqrt{D}}{\sqrt{\pi t}}. \qquad (2.10)$$

Eq. 2.10 is commonly referred to as the Cottrell equation and a plot of this response appears in Fig. 2.5. Note that at time t_0, the current is infinite according to Eq. 2.10. In real systems, i_f is limited by the rate of electron transfer at the surface of the electrode and the maximum current supply rate (slew rate) of the electronics applying the input voltage. After time t_0, the current rapidly decays at first and then asymptotically approaches zero.

To determine the concentration of an analyte, the researcher typically chooses a time long enough after t_0 so that the current associated with charging the electrode capaci-

tance is negligible, but soon enough that the current has not decayed too much to take the measurement. The current at this time will be proportional to the concentration of the analyte.

Although chronoamperometry is a very useful technique, it also has several serious shortcomings. The two major drawbacks of chronoamperometry are: (1) chronoamperometry is a relatively slow measurement technique with most measurements requiring perhaps 10 s or longer; and (2) chronoamperometry is not very selective. The current measured during a chronoamperometric scan is the sum of the faradaic currents produced by all ions in solution that are reduced at a potential more positive than E_a. Consequently, measurement of the concentration of a single analyte in a solution containing several different molecules can be difficult.

2.7.2 Linear sweep voltammetry

The excitation waveform for Linear Sweep Voltammetry (LSV) is a linear sweep of the applied voltage, E_a, from an initial voltage, E_i, to a final voltage, E_f. E_i is normally selected to be a voltage where no electrochemical reduction of $\boldsymbol{O}$ occurs, and E_f is selected to be a voltage at which so much reduction occurs that $C_O(x = 0) \approx 0$. The analysis from chronoamperometry applies again here with the exception that $C_O(0, t)$ is no longer assumed to be zero for the entire time period. Instead, a straight-line approximation of the slope of the diffusion profile,

$$\left.\frac{\partial C_O(x, t)}{\partial x}\right|_{x = 0} \approx \frac{C_O^* - C_O(0, t)}{d}, \qquad (2.11)$$

can be used to approximate $\left.\frac{\partial C_O(x, t)}{\partial x}\right|_{x = 0}$. Combining Eq. 2.4 and Eq. 2.11 gives the following approximation for i_f:

$$i_f \approx -nFAD\left(\frac{C_O^* - C_O(0, t)}{d}\right). \tag{2.12}$$

The quotient in this equation is the key to understanding the behavior of linear sweep voltammetry. As time passes and E_a nears and then passes E^0, the value of $C_O(0, t)$ begins to decrease, causing the numerator to increase. At the same time, the denominator is increasing as the depletion region extends into the solution. The result is that i_f rises exponentially to a peak near E^0. These conditions apply until the applied voltage is far enough beyond E^0 that the surface concentration of O is essentially zero; after that point, the response will resemble a chronoamperometric response, tapering off inversely with $\sqrt{t}$.

The height of the peak is related to how fast both the numerator and the denominator of Eq. 2.12 are changing, and the rate of change in the numerator and denominator is in turn dependant on the rate at which the applied potential is swept. A general linear sweep voltammogram is shown in Fig. 2.6. Note that in LSV, rather than plotting the current versus time, the horizontal axis is the applied voltage.

In LSV, the two most important characteristics are E_p, the voltage at which the current peaks, and i_p, the value of the current at that point. If the system is reversible, then the Randles-Sevcik equation applies

$$i_p = 2.69(10)^5 n^{\frac{3}{2}} A C_O^* \sqrt{D\nu}, \tag{2.13}$$

where ν is the scan rate of the applied voltage [Bard00]. If the diffusion coefficients for both ***O*** and ***R*** are approximately equal, then E_p is given by

$$E_p = E^0 - \frac{0.029}{n}. \qquad (2.14)$$

Since the working electrode has a different E^0 for each ion in solution, each ion in the solution will generate a different current peak at an E_p which is dependant on both the electrode material and the ion. The potentials at which these peaks occur can thus be used with Eq. 2.14 to identify the ions in the solution, and then, using Eq. 2.13, the value of i_p can be used to determine C_O^*. Unfortunately, many chemicals have standard potentials that are close enough to each other that this kind of analysis must be done with caution.

As with chronoamperometry, the above analysis will apply equally well to an oxidation reaction if the voltage is swept in the opposite direction, and the subtraction in Eq. 2.14 is changed to an addition. The current will, of course, flow in the opposite direction.

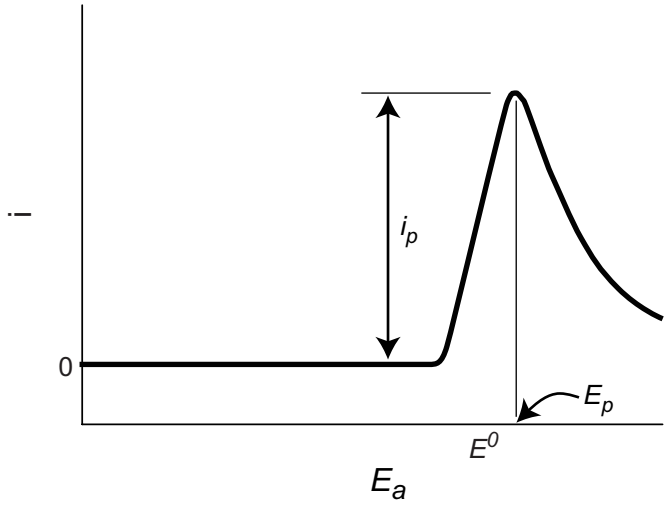

Figure 2.6: Linear sweep voltammogram. The potential at which the current peaks, E_p, and the current at the peak, i_p, are labeled.

2.7.3 Cyclic voltammetry

Cyclic voltammetry is an extension of LSV. Instead of sweeping the voltage in only one direction, after the linear sweep is concluded, the voltage is immediately swept back to the initial voltage at the same rate. If the analysis starts with a solution consisting of only ***O***, at the conclusion of the first sweep, an amount of ***R*** approximately equal to the initial concentration of ***O*** will be present at the surface of the electrode, and the reverse sweep will re-oxidize (if the reaction is reversible) whatever part of this material has not diffused away from the electrode and produce a current peak similar to the reduction peak, but in the reverse direction. A typical cyclic voltammogram appears in Fig. 2.7. The equations for i_p and E_p are the same as in linear sweep voltammetry because the technique is essentially two linear sweeps run back to back.

Cyclic voltammetry has several advantages over linear sweep voltammetry. The reverse sweep provides additional information to help identify materials. It also converts

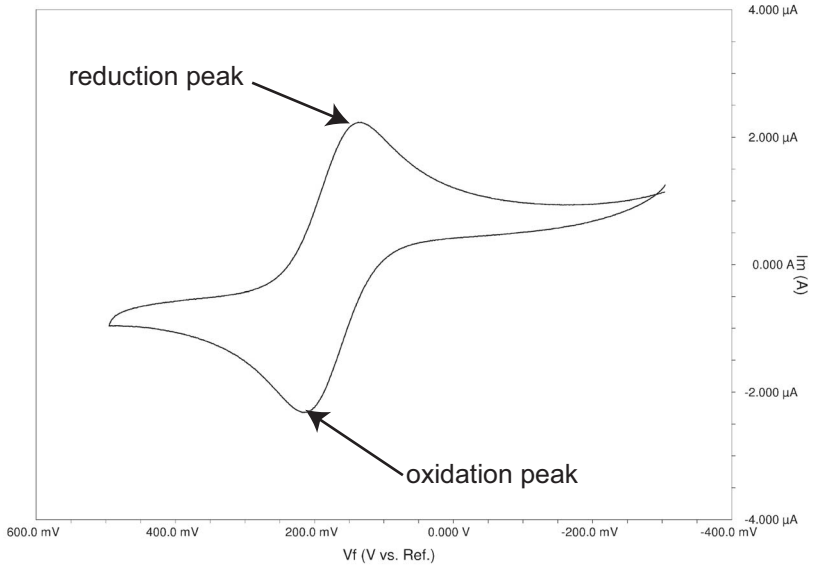

Figure 2.7: Voltammogram of potassium ferricyanide. Voltammogram of potassium ferricyanide showing a separation of 59mV between peaks in the forward and reverse scans. Sweep rate is 1V/s. Note that the x-axis is reversed, the more typical orientation in chemical science texts.

material back into its original form, which can prevent the accumulation of unwanted material. Additionally, many facts about the chemical reactions occurring at the surface of the electrode can be inferred from the observed peaks in the voltammogram. For example, if a peak is observed during the forward sweep indicating the reduction of an ion, then on the reverse sweep, a second peak should be observed indicating the re-oxidation of the ion back to its original form. If the two peaks are separated by 59 mV then Eq. 2.14 indicates that $n = 1$ for this particular redox reaction and that the reaction is reversible. Likewise, if $n = 2$ for the reaction, then the forward and reverse peaks will separated by 29.6 mV. Other analyses are also possible and information regarding intermediate products of the reaction as well as transfer kinetics can be observed using cyclic voltammetry. These methods are well documented and information regarding their application can be obtained in the many texts on the subject [Bard00, Kissinger96].

2.8 The three-electrode system

The analysis so far has described the use of two electrodes in the solution: the working electrode where the reaction of interest is occurring, and the counter which completes the electrical circuit and allows the application of an external potential. In practice, a reference electrode, is often added as illustrated in Fig. 2.8. In a three electrode electrochemical cell, the applied voltage, v_a, is composed of three parts: v_w,the potential drop at the surface of the working electrode; v_s, the potential drop due to the ionic resistance of the solution; and v_c, the potential drop at the surface of the counter electrode. When performing a voltammetric experiment, only the reactions occurring near the surface of the working electrode are of interest, and in order to measure the quantities of reactants at the working electrode surface, v_w and i_f must both be known. If only a counter and working

electrode are used, i_f can be measured; however, v_w cannot be set independently of v_s and v_c, and only v_a is measurable at the external cell connections.

The unknown contributions from v_s and v_c can be minimized by using a reference electrode such as an Ag/AgCl electrode as the counter electrode in order to obtain a well defined reference potential for v_c and by using a high ionic strength solution to minimize the resistance of the solution, R_{sol}, thereby reducing v_s ($v_s = iR_{sol}$). However, in practice, these approaches may not be practical or possible.

Although reference electrodes are normally non-polarizable, no electrode is ideal, and any current passing through a reference electrode will shift the electrode's reference potential away from its equilibrium value. Additionally, the most commonly used reference electrode in microsystems, the Ag/AgCl electrode, normally consists of only a thin layer of AgCl grown on the surface of an Ag electrode, and the faradaic reaction that occurs when current flows through an Ag/AgCl electrode consumes the layer of AgCl,

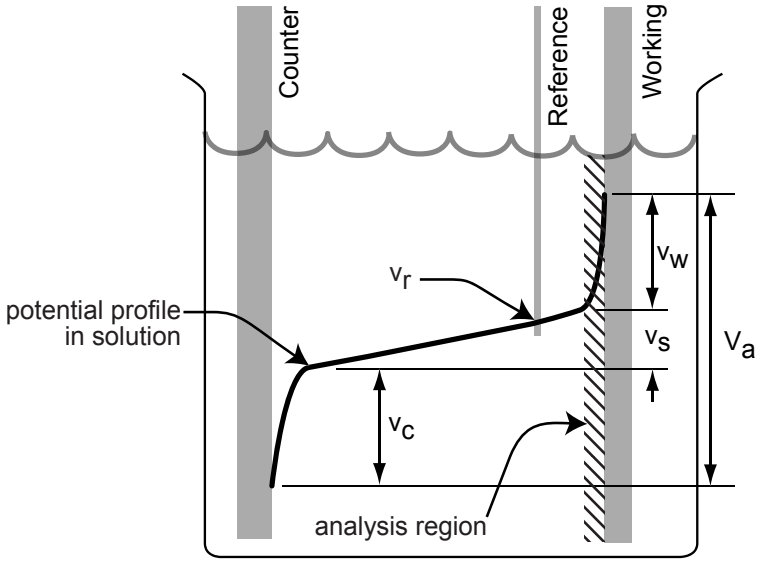

Figure 2.8: Potential drops. Three electrode system with all potential drops labelled. The analysis region is the area where the redox reaction under study is occurring. Note that the interface voltage drops (v_c,v_w) occur in a region near the electrodes that is typically less than a micron thick.

greatly shortening the life of the electrode. Adding a supporting electrolyte to a low ionic strength solution is not always desirable either, as the supporting electrolyte may interfere with the measurement (such as adding NaCl to the test solution for a chloride sensor), and for many simple automated test systems (such as the remote rainwater pollution monitoring station proposed by [Martin05]), requiring the addition of an electrolyte would unnecessarily increase the complexity of the system.

The addition of a reference electrode in close proximity to the working electrode removes most of the measurement error due to v_s, and completely eliminates v_c from the measurement. This removal of v_c is key in microsystems, as the small distance between the counter and the working electrodes in a microelectrode device has already reduced R_{sol} to a nearly negligible value. However, as the counter electrode decreases in size, v_c becomes strongly dependent on the current flowing through the cell, making the removal of its influence important.

2.9 Non-idealities

During the discussion of the more common electrochemical techniques in the previous sections, several assumption were made that glossed over non-idealities of which the reader should be aware. Two of these non-idealities are discussed in the following sections.

2.9.1 Parasitic electrode currents

In addition to the current generated by the redox reaction of interest, parasitic currents are also drawn to charge the electrical double layer capacitance discussed in Section 2.3, and additional current is generated by interfering redox reactions at the electrode surface by ions other than those intended to be measured. Sometimes these addi-

tional currents can be accounted for through calibration, but often they cannot be easily separated from the signal of interest without using a more complex technique such as square wave voltammetry. It is important to note that the current drawn to charge the double layer capacitance and the peak current measured during a voltammetric scan, i_p, are both dependent on the scan rate. The parasitic current drawn to charge the double-layer,

$$i_c = C_{dl}\nu, \tag{2.15}$$

is directly proportional to the scan rate, while the peak current (see Eq. 2.13) is only proportional to the square root of the scan rate. Consequently, while faster scan rates do enhance i_p, i_c increases at a faster rate, negating at least part of the benefit of increasing the scan rate.

On the other hand, both i_c and i_p are also directly proportional to the area of the electrode. However, as the electrode gets very small (less than 25 μm) non-planar diffusion effects discussed in the next section increase the flux of ions to the surface of the electrode, increasing the faradaic current above what would be predicted by Eq. 2.10.

2.9.2 Non-planar diffusion

Eq. 2.10 is derived by assuming the electroactive material diffuses to the electrode in a planar fashion. This assumption holds very well in the center of the electrode as shown in Fig. 2.9; however, near the edges of a planar electrode, material diffuses in a non-planar fashion. As the electrode size is reduced, the contribution from this non-planar diffusion begins to dominate as seen in Figures 2.9b and c. Clearly, for these cases, Eq. 2.10 will not hold. If a redox reaction at an electrode has a duration long enough that the electrode's longest dimension is much smaller than $d = \sqrt{Dt}$, the diffusion layer will

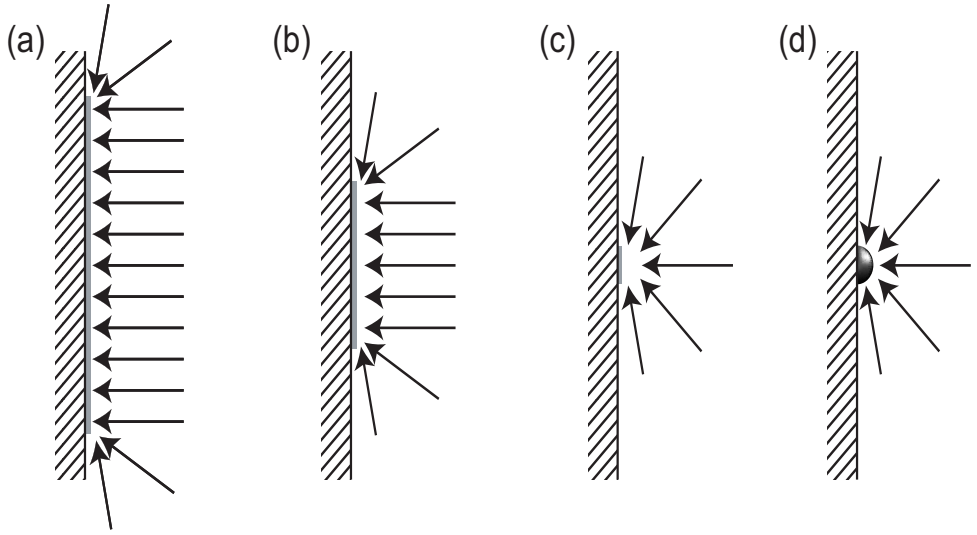

Figure 2.9: Planar and spherical diffusion to an electrode. Arrows represent material diffusing to the electrode a) a large electrode where planar diffusion dominates; b,c) progressively smaller microelectrodes where planar diffusion no longer dominates; and d) diffusion to a spherical electrode. Note the similarity between c and d.

have extended so far beyond the electrode geometry that the shape of the electrode starts to become less important, and material diffuses toward it in a way that is similar to diffusion towards a hemispherical electrode. For chronoamperometry, the equation for the faradaic current to a hemispherical electrode such as that in Figure 2.9d is

$$i_f = \frac{nFAC\sqrt{D}}{\sqrt{\pi t}} + \frac{nFACD}{r} \qquad (2.16)$$

where r is the radius of the hemisphere. The first term is the same as in Eq. 2.10, but the additional term is independent of time. Thus the current starts out similar to the planar case, but instead of decaying to zero it decays to a steady state value when the diffusion layer extends much farther into the solution than r. Absent convection, planar electrodes stimulated long enough will exhibit a very similar current relationship. The case in cyclic voltammetry is similar, with the current being enhanced by the non-planar diffusion to a

higher value. In addition, rather than the current decaying beyond the peak toward zero, it will stabilize at the same steady state value as in the chronoamperometric case. The enhanced currents of non-planar diffusion are extremely beneficial, and as a result, in order to reduce charging currents, the electrode is normally made as small as possible without reducing the peak current below the detection limits of the interface circuitry. As the electrodes become very small and the currents generated at the electrodes get even smaller, significant benefits are realized by integrating the chemical sensors tightly with CMOS circuitry as described in Section 6.2 on page 94 (see also [Kissinger96] and [Marsden84]).

Chapter 3

Neurochemical Sensing

3.1 State of the art in neurochemical sensing

Analyzing the brain's extracellular chemical environment has the potential to provide significant insight into neurotransmission, pharmacology, and behavior [Agnati00, Boulton95]. The first major work on the subject was Johann Thudichumm's "A Treatise on the Chemical Constitution of the Brain" in 1884, but it wasn't until the mid 20th century that significant progress was made in the field [Finlay00]. Although researchers frequently used bulk analysis of post-mortem tissue in early experiments to determine the concentrations of ions, neurotransmitters, and neurotransmitter metabolites, more focused methods which allow on-line, in vivo analysis have generally replaced post-mortem techniques. Currently, the three commonly used techniques for detecting neurochemical concentrations in vivo are push-pull cannulae, microdialysis, and in vivo voltammetry (See Fig. 3.1 for an illustration of the probes used with each of these techniques). Experimental specifications often drive which technique to use (see Table 3.1). The push-pull cannula method, which involves the infusion of fluid through one cannula and extraction of extracellular fluid through a second cannula, was pioneered by Gaddum in the early 1960's

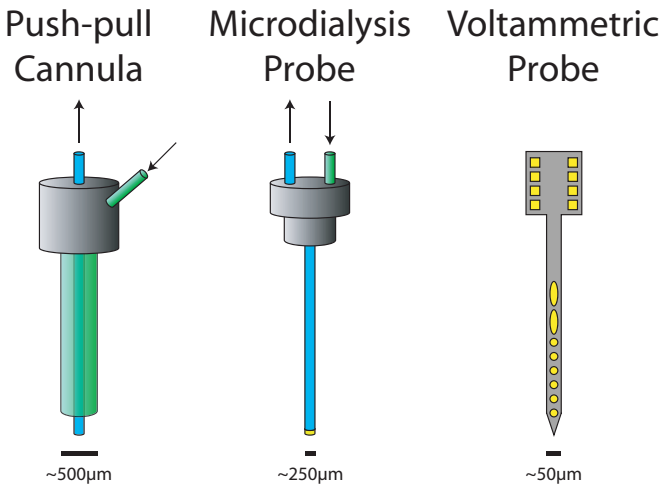

Figure 3.1: Illustration of the three most common types of neurochemical probes.

Table 3.1: Benefits of each neurochemical sensing technique.
Each technique is ranked as either excellent (+), neutral (=), or poor (-).

	Push-Pull	Microdialysis	in vivo Voltammetry
Sensitivity	=	+	=
Selectivity	+	+	-
Spatial resolution	-	-	+
Temporal resolution	-	-	+
Minimal implant disturbance	-	=	+
Minimal tissue disturbance during operation	-	+	+
Multi-analyte analysis	+	+	+
Post implant calibration	+	+	-
Concomitant unit recordings	-	-	+

[Gaddum61]. The microdialysis technique, which involves diffusion of neurochemicals across a dialysis membrane and into a fluidic channel, was pioneered several year later, but didn't become popular until the work of Ungerstedt, et al [Robinson91, Ungerstedt91]. Both of these techniques have similar advantages: high sensitivity and selectivity, the abil-

ity to deliver drugs to targeted locations, and the means for performing periodic calibration since the sensing units are not implanted with the neural probe. However, the same separation between the probe and the sensing units also means that there is a delay between the sampling and the measurement, and while many important experiments (mostly steady state type measurements) are unaffected by this delay, the ability to monitor concentration levels in real time and to record fast transients in the levels of different neurotransmitter is greatly enhanced when the measurement device is included in the implant. Additionally, the large size of both push-pull cannulae and microdialysis probes perturbs the normal function of surrounding neurons causing an inflammatory response. The large size of these probes also precludes the ability to measure small volumes of fluid in close proximity. As a result, when experiments require high spatial and temporal resolution, in vivo voltammetry is the preferred method for neurochemical detection [Finlay00]. This approach is the focus of the present work.

3.2 In vivo voltammetry

In vivo voltammetry, first demonstrated in the early 1970s, is now a proven method for measuring neurochemical concentration basal levels and fluctuations [Adams76, Burmeister01, Ewing83, Kissinger73]. The technique involves using a potentiostat to apply a voltage between a working and reference electrode, while measuring the resulting faradaic and non-faradaic current flow between the working and counter electrode. The faradaic current generated at the electrode-electrolyte interface by the oxidation or reduction of the analyte can be related to the analyte's concentration through a priori calibration curves. In vivo voltammetry normally involves chronoamperometry with occasional voltammetric scans (via cyclic voltammetry or pulsed voltammetry). Chronoamper-

ometry is used to monitor changes in total analyte concentration while voltammetric scans are used to provide information about individual analytes (represented by peaks on the scan). These scans can be sampled at speeds up to 100 kS/s providing high temporal resolution for monitoring fast reactions or more slowly (10 S/s or less) for longer term monitoring of chemical levels [Roham08].

Some of the easily oxidized neurochemicals include catecholamines, indoleamines, and their metabolites [Crespi88]. Many of these substances oxidize at similar potentials making separation of the target analyte signal from interferant noise problematic [Ghasemzadeh91, Phillips03]. Modifying the electrode surface (with an electrochemical pretreatment in the case of carbon-based electrodes or with a membrane such as Nafion) can shift interferant oxidation potentials and thereby improve selectivity [Justice87]. Other neurochemicals such as acetylcholine, glutamate, and glucose require indirect biocatalytic sensing techniques, which often necessitate the use of an enzyme-reaction to create products that can be oxidized. These configurations facilitate greater selectivity since enzymes are inherently selective to their target analyte. A number of methods have been developed to immobilize enzymes on an electrode surface, including covalent bonding through cross-linking agents such as glutaraldehyde, entrapment within a polymeric film such as Nafion, avidin-biotin binding, or even incorporation within the bulk of a composite film such as iridium or carbon [Bartlett87, Garguilo95, Hu94, Wang99].

3.3 Existing in vivo voltammetric probe technologies

The most popular materials for in vivo voltammetric sensors are carbon, platinum, gold, and iridium. These materials are often formed into microwires with a microdisc-shaped tip, which can be mechanically polished. The microwires are then encased in a

pulled-glass micropipette, exposing just the tip of the wire, to improve rigidity and provide insulation. These devices are typically single channel, but can be designed for multichannel recordings with sensing elements 10-15 microns apart [Dressman02]. Although these are proven technologies [Boulton95], the fabrication of such devices relies on handmade, lab-specific techniques. Microfabricated probes are a relatively new technology that was first applied to electrophysiology measurements [Vetter04]. However, during the last decade, researchers have begun applying the same probes with tailored materials to neurochemical measurements as well. These probes have the advantages of batch fabrication, high reproducibility of probe micro-scale features, and flexibility to customize electrode recording site placement and substrate shape [Burmeister00, Johnson03].

Microfabricated probe technology has been developed at the University of Michigan and the University of Utah for electrophysiological recordings. An initial feasibility study for microfabricated neurochemical sensors was undertaken in 1990 [van Horne90]. Since then, Burmeister et al. have published work on a single-shank ceramic-based multichannel sensor [Burmeister00, Burmeister02], as has Johnson et al. on a silicon-based neurochemical sensor with integrated microfluidic channels [Johnson03]. Both devices have merit. For the specific aims of this work, the potential to deliver drugs through the probe and the 2-D site layouts on one or more penetrating shanks of our silicon probe technology provide particular advantages.

3.3.1 Simultaneous electrochemical and electrophysiological recording

A primary advantage of in vivo voltammetric sensing is the potential for simultaneously recording electrophysiological and neurochemical events. Correlating neurochemical levels with electrophysiological unit and local field potential recordings enables

researchers to investigate neurotransmission phenomena and to acquire valuable neural feedback after delivering drugs to precise cellular regions. Previous studies that recorded both signal types have used separate probes (such as a carbon fiber for neurochemical sensing and a platinum-iridium microwire for unit recording) that are stereotaxically positioned close to one another (on the order of 100 μm) to detect the same neuronal environment [Bickford91, Su90]. While this method has yielded good results for single channel recordings, it is not practical for large multichannel recordings due to the difficulty in accurately placing large numbers of individual electrodes [Stamford93].

Other studies have examined using the same electrode to switch between electrochemical and electrophysiological recordings [Stamford93, Armstrong83, Crespi95]. This technique guarantees recordings from the same neuronal environment with less tissue damage due to only a single probe penetration. Yet, the method causes gaps in the electrophysiological recording data and precludes optimized electrode geometries for each type of recording. For instance, increasing dimensions of carbon fiber probes will yield better sensitivity to neurochemicals, but will decrease the selectivity of electrophysiology recordings. A microfabricated approach has the potential for reliably yielding closely spaced electrode sites.

3.3.2 Drug delivery technology platforms

Drug delivery to particular brain regions while monitoring the extracellular neurochemical responses can be useful in studying the effects of certain drugs on neural activity or increasing sensitivity to an analyte of interest (for example, using Merital to inhibit dopamine reuptake). Drug delivery can readily be performed through microdialysis probes and push-pull cannulae due to their inherent use of fluid exchange, but voltammetry

probes lack the fluidic channels which are inherent to the other two types of probes. As a result, fluid delivery with voltammetry probes requires the insertion of a additional small tube near the working electrode. Drawbacks of this additional insertion include damage to the neuronal environment and imprecise distances between the delivery point and the electrode site. Microfabricated voltammetry probes with integrated microfluidic channels have the potential to mitigate these difficulties while providing more specific and timely recordings of neural responses to pharmacological agents [Chen97, Rathnasingham04].

3.4 Preliminary studies

The specific aims of this research have been to advance neurochemical sensor integration into silicon-based probes by building upon previous work done in this area. Since the 1980's, University of Michigan researchers working under the direction of Dr. Wise have focused on refining neural probe implant technology for electrophysiological recording. During the last twenty years they have increased channel counts, fabricated 3-D arrays of probes, integrated microfluidic channels into the probe fabrication process, and investigated geometries and materials for reducing the brain's immune response to neural probe insertion [Wise08, Wise09]. During the same time frame, students in Dr. Brown's chemical sensors research group have worked on the development of chemical sensors for a variety of applications including water quality testing and in situ processes monitoring, and recent research has focused on in vitro dopamine sensors [Strong04] and tight integration of CMOS circuits and chemical sensors [Martin05]. The rest of this chapter summarizes the work done previously by researchers from these two research groups, and then lays out how these prior studies enabled the work described in this dissertation.

3.4.1 Michigan probes

"Michigan" neural probes are silicon microfabricated devices for both acute and chronic implantation in the brain. The probes have several favorable attributes including batch fabrication, high reproducibility of geometrical and electrical characteristics, easy customization of recording site placement and substrate shape, small size. Additionally, probes have been fabricated with integrated flexible micro-ribbon cables and on-chip electronics for signal conditioning. The extensibility of the platform technology enables custom designs for diverse applications. For example, planar probes have been assembled into multiplane arrays for precise three-dimensional placement of recording sites in the brain [Bai00, Perlin09], and the probes have been combined with a parylene ribbon cable to form a hybrid assembly to provide additional mechanical flexibility [Wise08].

3.4.2 In vitro neurochemical sensing

Previously, researchers in Dr. Brown's research group investigated neural arrays for monitoring cultured human neurons using microfabricated arrays of three-electrode devices having sensing areas ranging from 4-10,000 μm^2 (see Fig. 3.2). Each three-electrode device incorporated a platinum working electrode, a platinum counter electrode, and a chloridized silver reference electrode. Fabrication of the devices required a four mask lithographic process on standard 4" silicon wafers, and the final devices were packaged in an autoclavable ceramic PGA assembly as shown in Fig. 3.3. During a 75-day experiment, action potentials and corresponding neurochemical releases were recorded and analyzed from human neuron cultures (hNT cell line from Stratagene, La Jolla, CA, USA). This cell line was selected because it is known to be spontaneously active, releasing dopamine without external stimulation. A sample sensor response showing correlation between neu-

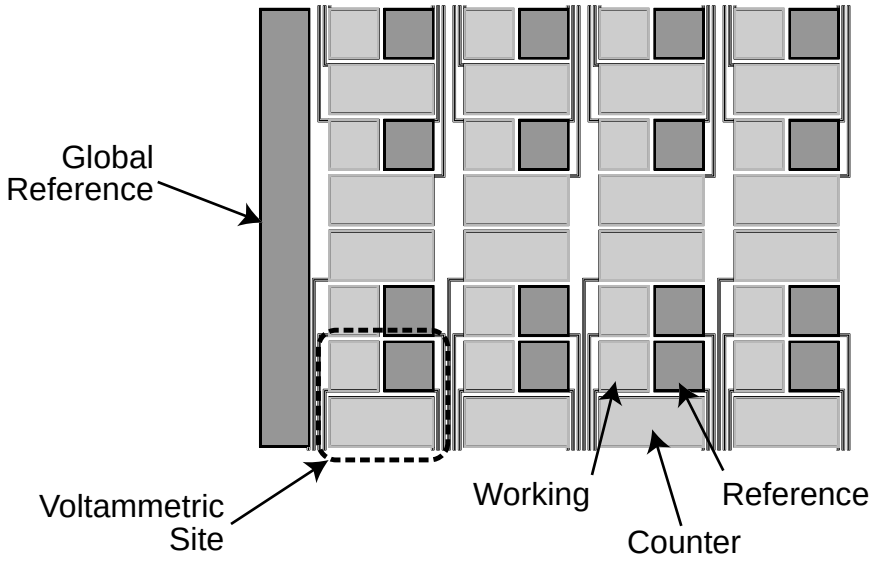

Figure 3.2: Passive sensor array configuration. The schematic is of a 100 μm array. Orientation of the devices is alternated to enable the use of combinations of electrodes as a larger macro electrode if desired [Strong04].

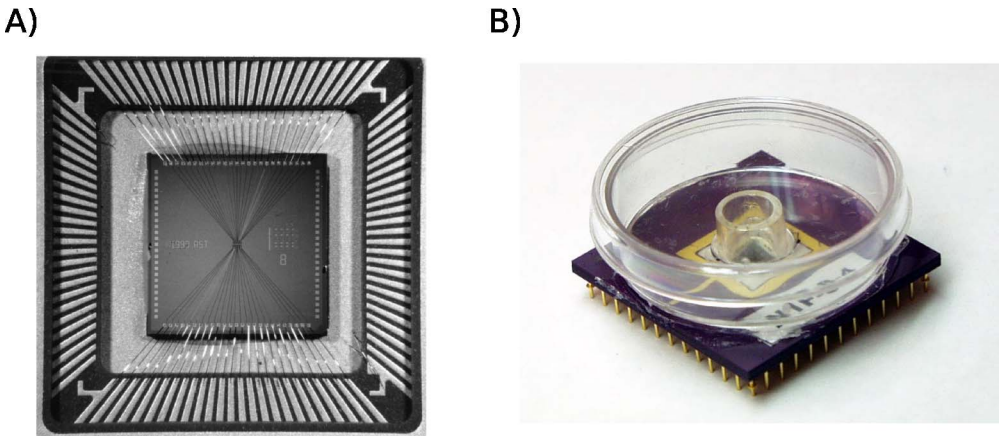

Figure 3.3: Passive neuro-array. A) 8 μm array in ceramic PGA, B) Completed device, with an incubation chamber attached by AST Inc. The petri dish on top of the chamber was used to maintain sterility of the neuron culture between tests [Strong04].

rophysiological and neurochemical signaling is shown in Fig. 3.4. Cyclic voltammetry was used in this study to establish basal chemical concentration levels, and constant-voltage voltammetry was then used to monitor chemical concentrations in near real-time. The results from this study encouraged the investigation of in vivo chemical concentrations

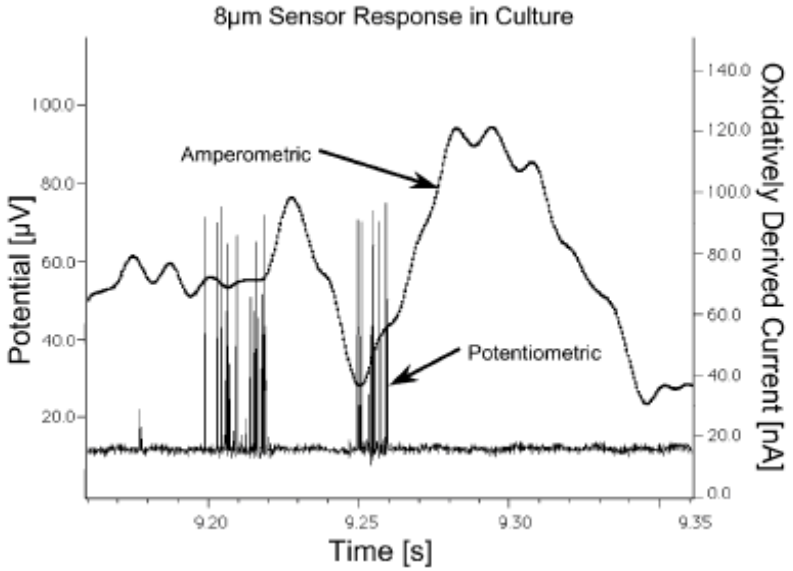

Figure 3.4: Correlated chemical and electrical signals. The amperometric signal represents dopamine concentrations, while the potentiometric signal demonstrates concomitant neuronal unit recording.

using similarly arrayed structures, and demonstrated the potential for in vivo neurotransmitter recordings.

Additionally, strong ties between VLSI digital and analog designs and microfabricated sensors have been forged within Dr. Brown's group. Previous work by Dr. Martin and Dr. Strong has resulted in tightly coupled systems with sensors fabricated on top of analog readout circuitry [Martin03, Martin05]. Dr. Brown's group has also produced several generations of a microprocessor known as the WIMS microprocessor which have been targeted at low-power mixed-signal sensing applications including environmental sensing, a cochlear prosthesis, and most recently a neural prosthesis.

Prior to the start of this research, researchers from Dr. Kipke's group at the University of Michigan reported on chemical sensing using retrofitted Michigan probes [Johnson03]. The probes were retrofitted by dip coating neural probes in Nafion, an cation exchange polymer. The study demonstrated the short-term biocompatibility of Nafion and

increased the selectivity of devices in the presence of interferants such as ascorbic acid. However, the dip coating process coats the entire probe and is therefore not suitable for work requiring the selective coating of individual sites. Additionally, when applied to fluid delivery probes, the dip coating process blocks the outlet port rendering the fluidic portion of the probe unusable. The success of this work motivated investigation of some of the alternative site selective coating strategies reported in Chapter 5. During the early stages of this work, strong ties were formed between Dr. Kipke's and Dr. Brown's research groups resulting in an NIH R21 grant to investigate voltammetric probes, and a large portion of the work reported here is a direct result of that collaborative effort.

3.5 Conclusion

Neurochemistry is a field with a rich history and more than a century's worth of research. However, new techniques and technologies are rapidly advancing the state of the art in this field. Voltammetry probes, one of these new technologies, enable new types of research through simultaneous electrophysiology and neurochemistry. Researchers at the University of Michigan have built the pieces needed to develop this new technology over the last twenty years. This work brings those pieces together to develop silicon-based voltammetry probes by adapting chemical sensing technologies to the Michigan neural probe platform.

Chapter 4

Iridium Oxide Reference Electrodes

4.1 Background

Various neurochemical sensors based on electrochemical detection methods such as cyclic voltammetry (CV), chronoamperometry, and potentiometry have been reported in the literature [Chung06, Johnson05, Strong01, Toner96]. These electrochemical sensors require at least two electrodes, a sensing electrode (referred to as either a working electrode or an indicator electrode depending on the detection method used) and a reference electrode (see Section 2.8 on page 24 for more information). Electrode materials for the sensing electrode have been widely studied; the electrode material should be tailored to favor a specific reaction at the surface of the electrode. Reference electrodes, on the other hand, are selected for stability and insensitivity to changes in the surrounding medium [Franklin07]. A good reference electrode is characterized by a well defined Nernst reaction at the surface of the electrode that sets the potential difference between the electrode and the surrounding medium to a predictable value. The surface reaction should also be a fast reaction that allows current to pass through the electrode without affecting its potential, and finally, the electrode should exhibit little to no dependence on temperature.

Ag/AgCl is one of the most popular reference electrodes for electrochemical sensors, and for in vivo work, Ag/AgCl electrodes have been the reference electrode of choice for most applications [Changeux93, Chung06, Mitala06, Pothos91, Tierney09]. Ag/AgCl forms a nearly ideal non-polarizable liquid-solid interface, and its Nernst reaction depends on the Cl^- concentration of the surrounding medium making it a good reference electrode in solutions with moderate to high concentrations of Cl^- including most biological fluids. But, there are several strong disadvantages to using Ag/AgCl electrodes in biological samples. First, AgCl is toxic and has been shown to cause widespread necrosis in biocompatibility studies [Moussy94, Stensaas78] making it suitable only for acute and short term chronic studies. Second, thiols such as cysteine and glutathione form very strong complexes with Ag ions causing the potential of bare Ag/AgCl electrodes to change dramatically in biological samples. Finally, Ag is a highly reactive material, making microfabrication of Ag based electrodes problematic, and the resultant Ag/AgCl films are often fragile and subject to delamination during tissue insertion [Strong04]. To counter these problems, Ag/AgCl reference electrodes are commonly placed on the surface of the brain instead of being implanted in order to minimize the Ag/AgCl's effect on the tissue of interest. Other experiments have replaced the Ag/AgCl with a pseudo-reference electrode such as stainless steel which lacks the long-term potential stability of a real reference electrode.

Several possible alternative reference electrodes were evaluated during this work including Iridium Oxide (IrO_x), chloride sensitive epoxy reference electrodes, and polymer encapsulation of Ag/AgCl electrodes. The epoxy reference electrodes were found to have a very high impedance requiring the addition of extra circuitry to stabilize the poten-

tiostat [Shin04], and while some polymer coatings such as hydrophylic polyurethane may have been used to improve the biocompatibility of Ag/AgCl electrodes for short periods of time [Moussy94, Shin01], the long term effects of these coatings have not been well studied, and it is probable that some of the Ag/AgCl will leach out over time and affect the surrounding tissue. In light of these issues, the decision was made to pursue IrO_x as the reference electrode of choice for this work [Franklin05, Yang03, Yang04].

4.2 Iridium oxide reference electrodes

IrO_x electrodes exhibit excellent charge injection properties (at least 3-5 mC/cm^2) [Cogan05, Meyer01], have been shown to be biocompatible during long-term in vivo studies, and are mechanically stable, avoiding problems with delamination during insertion [Slavcheva04, Weiland00, Weiland02]. IrO_x electrodes are especially attractive for use on neurochemical sensing probes, as IrO_x is commonly used as the electrode material for stimulation on microfabricated neural probes due to its high charge injection capabilities [Cogan02, Cogan04, Weiland00, Weiland02, Ziaie96].

IrO_x is characterized by the following reaction,

$$Ir_2O_3 + H_2O \Leftrightarrow 2IrO_2 + 2H^+ + e^-,$$

indicating a strong dependence on the H^+ concentration of the surrounding medium, and indeed IrO_x exhibits a Nernstian to Super Nernstian response to the concentration of H^+. Several researchers have exploited this dependence to fabricate IrO_x pH electrodes [Ges05], but in biological applications, where the pH is normally constrained to a narrow range, particularly in the brain where normal pH readings are within 7.2 and 7.4 [Johnson07], the H^+ dependence of IrO_x can also be used to set a stable reference potential

between the IrO_x electrode and the surrounding medium. This well defined potential coupled with IrO_x's excellent biocompatibility and wide use within the neuroscience community as a recording and stimulation electrode makes IrO_x an ideal reference electrode for studies in the brain.

IrO_x films are a non-stochiometric matrix of both IrO_2 and IrO_3 molecules, and the exact ratio of these molecules in the film affects both the physical properties (color, electrochromicity, roughness, etc.) and the electrochemical properties (open circuit potential [OCP], charge injection capacity, pH response, impedance, etc.) of the film. Due to the inexact nature of the IrO_x matrix, the method used to form the IrO_x film has a strong influence on the final properties of the film. Most of the methods reported for forming IrO_x films in the literature can be grouped into one of four categories: thermal growth of IrO_x on an Ir electrode, electrodeposition of IrO_x from an electrolyte solution, reactive sputter deposition of IrO_x films in an oxygen rich plasma (SIROF), and electrochemical formation of activated IrO_x films (AIROF) by anodic growth of IrO_x on Ir metal electrodes [Cogan04, Cogan07].

The work presented in this chapter concentrates on SIROF and AIROF electrodes due to their use on the two most common implantable electrode platforms—Michigan style neural probes (AIROF) and the Utah Electrode Array (SIROF). Two studies are presented in this chapter. The first study compared the OCP and electrochemical impedance stability of AIROF and SIROF films. The second study evaluated several activation protocols for stability and pH response.

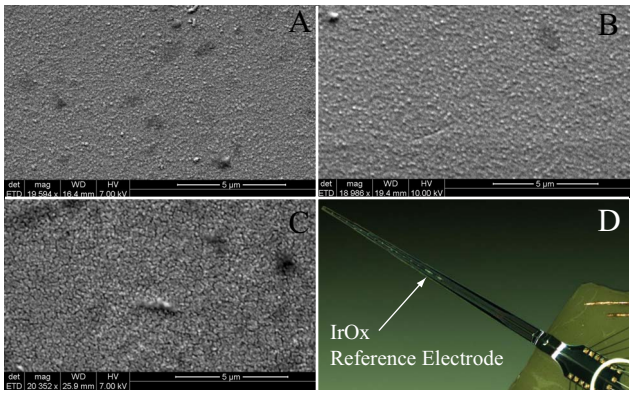

Figure 4.1: IrO_x SEMS. SEM Pictures of (A) PBS activated IrO_x (A1), (B) base activated IrO_x (A2), and (C) sputtered IrO_x (S1) films showing surface morphology. Picture of Michigan style neural probe (D) with on-chip AIROF electrode. ©2009 IEEE. Used with permission from [Franklin09].

4.3 Comparison of AIROF and SIROF films[1]

4.3.1 Electrode fabrication

500 μm diameter IrO_x electrodes were fabricated on silicon wafers by depositing and patterning a platinum interconnect layer. The interconnect layer was next encapsulated with a 250 nm layer of PECVD silicon nitride followed by a 100 nm layer of parylene. Contact openings were etched in the encapsulation with RIE, and a final layer of either Iridium (which was activated to form AIROF electrodes) or IrO_x (SIROF electrodes) was sputter deposited and patterned. Both types of electrodes were formed on the same wafer by masking half of the wafer during each deposition with a a layer of photoresist. Please see the run sheet in Appendix A for more information on the exact parameters used in the process. The final electrodes were examined in an FEI Quanta 600 FEG SEM to verify the presence of IrO_x on the fabricated electrodes (See Fig. 4.1).

1. Section 4.3 is based on "A Comparison of Fabrication Methods for Iridium Oxide Reference Electrodes," by R. Franklin et al. which appeared in Proceedings of IEEE Sensors 2009. Figures and portions of the text are ©2009 IEEE. Used with permission.

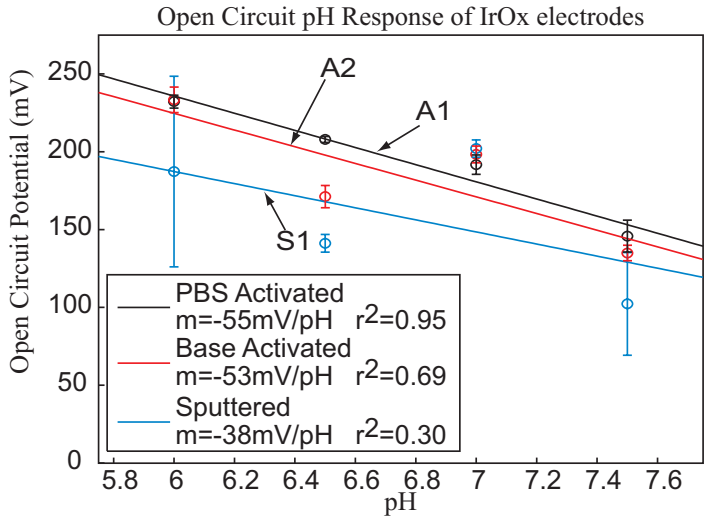

Figure 4.2: IrO_x pH response. pH response of AIROF and SIROF films (n=10) after formation of IrO_x films and soaking in PBS for 24 hours. An ideal Nernstian response would be 59 mV/dec. ©2009 IEEE. Used with permission from [Franklin09].

4.3.2 Iridium oxide formation

IrO_x films were prepared using three different methods:

1. Pulsed DC sputter deposition of IrO_x in an oxygen plasma (S1)
2. DC sputter deposition of Ir followed by activation in phosphate buffered saline (PBS) (A1)
3. DC sputter deposition of Ir followed by activation in Na_2HPO_4 (A2)

The A1 and A2 electrodes were activated by applying a 1 Hz Square wave between +0.9 to -0.85 V for 200 cycles [Johnson06]. The activation was performed using a Gamry FAS2 femtostat with respect to a Saturated Calomel Electrode (SCE). After activation the electrodes were soaked in PBS for 24 hours before further characterization.

After fabrication, all of the electrodes were initially characterized for pH response in phosphate buffer by varying pH from 6 to 7.5 (see Fig. 4.2). The AIROF films A1 and A2 were found to have a near Nernstian response of approximately -55 mV/dec and were tightly grouped with an average σ of less than 20 mV. In contrast, the SIROF film, S1, exhibited a smaller pH response of only -38 mV/dec, and exhibited much greater variabil-

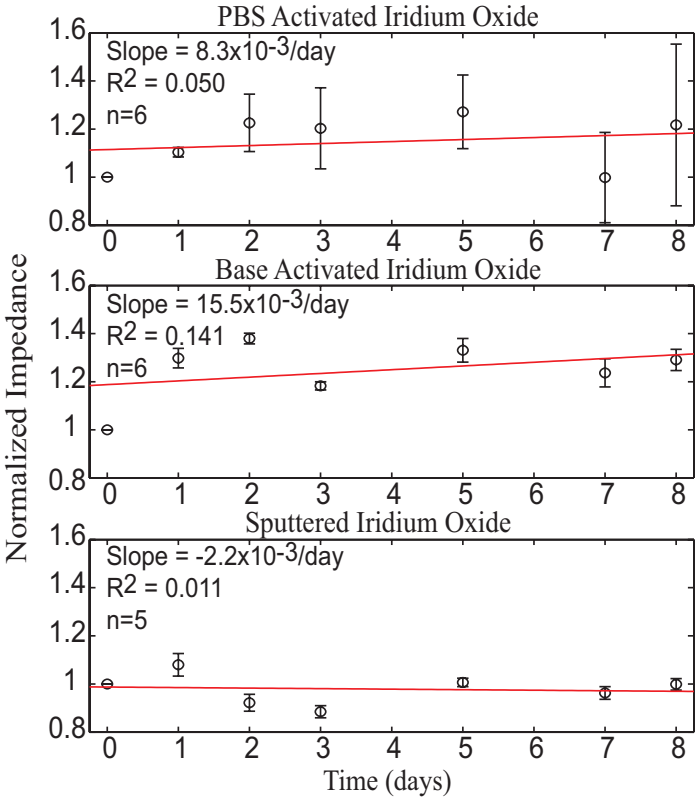

Figure 4.3: IrO_x impedance measurements. Normalized Impedance graphs for each of the three fabrication methods. SIROF films exhibited the least variation over time while PBS Activated films exhibited the widest variation. ©2009 IEEE. Used with permission from [Franklin09].

ity with an average σ of more than 80 mV. The S1 electrodes had an especially large variation at the low end of the pH scale (pH 6.5).

4.3.3 Results

After pH testing, the electrodes were subjected to soak testing in pH 7.4 PBS for a period of nine days. At regular intervals during the test, the electrochemical impedances of the electrodes were measured at 1 kHz (Fig. 4.3). The open circuit potentials (OCP) of the electrodes vs. SCE were also measured for each electrode in pH 7.4 PBS (Fig. 4.4). During the soak testing, the SIROF electrodes were found to have the least variance in impedance (< 0.3% change in impedance per day) while the AIROF electrodes, A1 and A2,

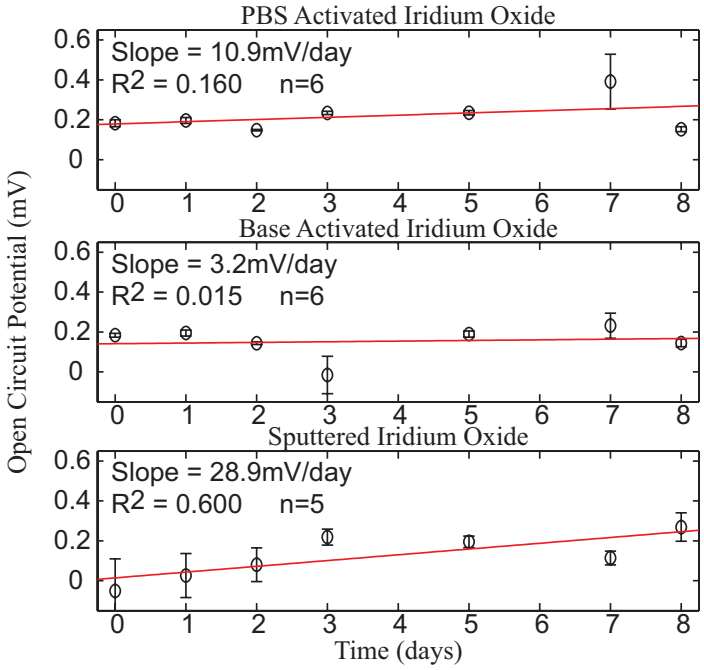

Figure 4.4: IrO_x EOC measurements. Open Circuit potential plots for the three fabrication methods. Open circuit potentials were measured using a Gamry FAS2 femtostat in pH 7.4 PBS. ©2009 IEEE. Used with permission from [Franklin09].

exhibited greater rates of change, 0.8% and 1.6% per day respectively. However, the OCP of the AIROF electrodes was more stable with A2 having the lowest rate of drift (3.2 mV/ day), A1 having 10.9 mV/day of drift, and S1 having a drift of 29 mV/day.

4.3.4 Dopamine detection

Based on the results of the soak test, a set of 1.5×10^3 μm^2 Ir electrodes were fabricated on probes with 30 μm diameter Platinum (Pt) working electrodes, and a 1.5×10^3 μm^2 Pt counter electrode. The Ir electrodes were activated in Na_2HPO_4 using the A2 protocol and then used to perform in vitro measurements of dopamine (DA). For this experiment, powdered dopamine hydrochloride was dissolved in phosphate buffer adjusted to pH 3.85 and stored in an opaque bottle to protect the DA from light induced chemical reactions [Strong04]. Fig. 4.5 shows CV scans for 10 mM DA solution in phos-

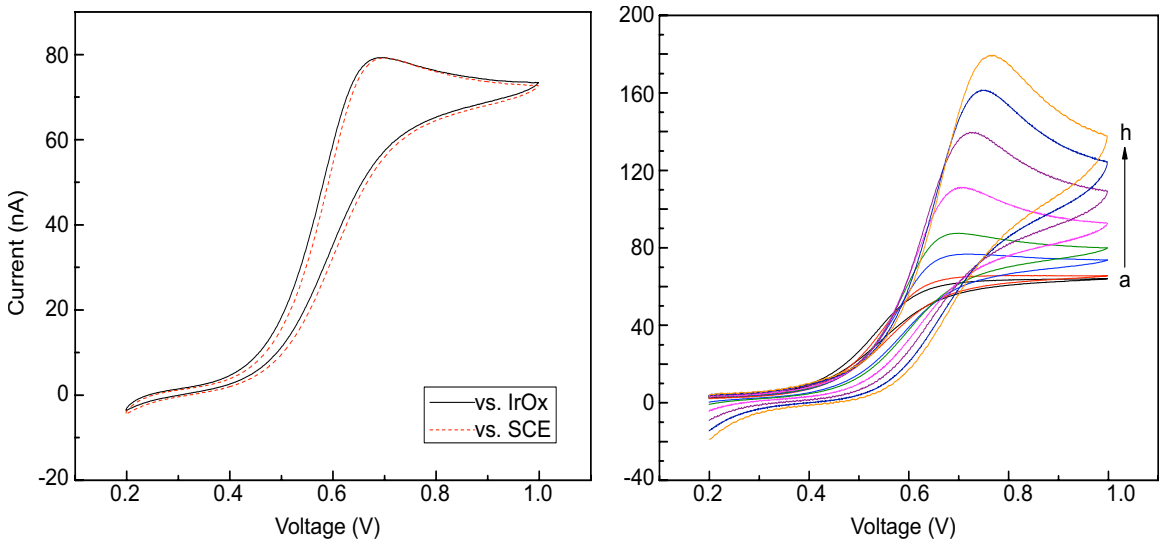

Figure 4.5: Dopamine CV measurements. Cyclic voltammograms (left) of 10 mM DA in PBS at pH 3.85 using IrO_x and SCE reference electrodes with a scan rate of 1000 mV/s. Cyclic voltammograms (right) of 10 mM DA in PBS at pH 3.85 with scan rate of: (a) 50 mV/s, (b) 100 mV/s, (c) 500 mV/s, (d) 1000 mV/s, (e) 2500 mV/s, (f) 5000 mV/s, (g) 7500 mV/s, (h) 10000 mV/s. ©2009 IEEE. Used with permission from [Franklin09].

phate buffer (at pH 3.85) versus both SCE and IrO_x reference electrodes. The scans are nearly identical except for a potential difference of 9 mV between two peak potentials representing the potential difference of the IrO_x electrode (+232 mV vs. standard hydrogen electrode (SHE)) at pH 3.85 and SCE (+241 mV vs. SHE). Fig. 4.5 also shows CV scans at various scan rates from 50 mV/s to 10,000 mV/s. Fig. 4.6 shows CV scans of DA in concentrations from 10 mM down to 0 mM at pH 3.85 with a scan rate of 1,000 mV/s. The second part of Fig. 4.6 is the calibration curve obtained by plotting the current values at 600 mV vs. IrO_x (n=3). The results show a linear increase of 5.85 nA/mM in response to an increase in DA concentration.

4.3.5 Conclusion

Based on the observations reported here, SIROF electrodes appear to be more stable in terms of electrochemical impedance, but for the purposes of establishing a stable

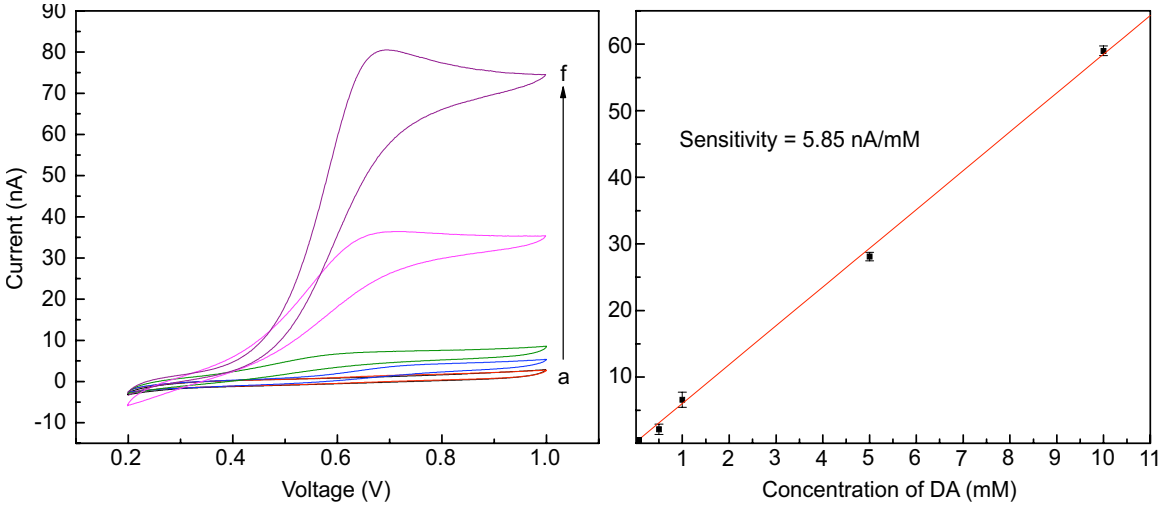

Figure 4.6: Dopamine CV characterization. Cyclic voltammograms (left) of DA solution in PBS at pH 3.85 with various concentrations: (a) PBS only, (b) 0.1mM, (c) 0.5mM, (d) 1 mM, (e) 5mM, (f) 10mM with scan rate of 1000 mV/s. (Right) Calibration curve for DA based on data. ©2009 IEEE. Used with permission from [Franklin09].

reference potential, AIROF electrodes can be considered superior due to their improved open circuit potential stability. This finding is in agreement with the more general studies reported in the literature [Hitchman88, Yuen83]. Additionally, this study is the first reported measurement of DA electrochemically using an integrated AIROF IrO_x reference electrode on a microelectrode array. The IrO_x electrode showed excellent characteristics as a reference electrode under the several conditions tested. The second study in this chapter expands upon these findings by comparing several different activation protocols and studying the chemical stability over time of each protocol vs. a commercial reference electrode.

4.4 AIROF activation protocols[1]

4.4.1 Probe fabrication

Two types of probes were fabricated for the comparison of activation protocols. The first type (Fig. 4.7A) was fabricated as part of a batch of standard Michigan neural probes [Drake88]. A single extra metal mask was added to the process flow in order to allow for the inclusion of both Ir and Pt electrodes on the probes. The eight-site probes include a 1.5×10^3 μm^2 IrO_x reference electrode, a 1.5×10^3 μm^2 Pt counter electrode, three circular Pt working electrodes for electrochemical recording, and three circular IrO_x electrodes for electrical recording. A second batch of "test" probes (Fig. 4.7B) were fabricated using a simplified set of processing steps. All boron diffusion steps were removed from the standard Michigan probe process and Pt was used for the interconnect instead of polysilicon. The final devices were separated using a dicing saw, wire-bonded onto a printed circuit board, and encapsulated in Nusil MED-4211 in the same fashion as normal Michigan probes. These probes also included a single 1.5×10^3 μm^2 IrO_x reference elec-

Figure 4.7: Micrographs of chemical probes. These are micrographs of the probes fabricated for this project. The probe in the picture on the left shows a Michigan style neural probe with integrated reference and counter electrodes. The probe on the right is one of the test structure probes with SU-8 rings for site specific coatings. ©2005 IEEE. Used with permission from [Franklin05].

1. Section 4.4 is based on "Iridium oxide reference electrodes for neurochemical sensing with MEMS microelectrode arrays," by R. Franklin et al. which appeared in Proceedings of IEEE Sensors 2005. Figures and portions of the text are ©2005 IEEE. Used with permission.

trode, a single 1.5×10^3 μm^2 Pt counter electrode, and six circular Pt working electrodes ranging in radius from 4 to 50 μm. All of the in vitro results reported in this section were recorded using these probes.

4.4.2 Methods

Amperometry experiments were performed using a Gamry FAS2 femtostat. Cyclic Voltammetry experiments operated at scan rates of 10 V/s with a sampling interval of 5 ms. Experiments were performed in 40 mL of 0.1 M Phosphate Buffered Saline (PBS) solution (Sigma-Aldrich). Injection solutions contained dopamine-hydrochloride (Fisher Scientific). An anodically chloridized Ag wire was used as a control reference electrode for comparison during the experiments.

pH response experiments were performed using a high input impedance 16-channel analog-to-digital converter (Multi pH/ion meter KST101B, Kosentech, Busan, Korea) which serially transferred the measured data to a PC. The response of the electrodes to varying pH was examined by adding aliquots of NaOH to a solution of 11.4 mM boric acid / 6.7 mM citric acid / 10.0 mM Na_2HPO_4 at room temperature. All measurements were made in a magnetically stirred solution.

AIROF electrodes were used for all of the experiments presented here. During probe fabrication, a seed layer of Ir was sputter deposited and photolithographically patterned. After releasing the probes, the Ir electrodes were “activated” using one of three protocols in 0.1 M Na_2HPO_4:

1. CV for 10 cycles from +0.8 V to 0.5 V vs. SCE
2. CV for 80 cycles from +0.8 V to 0.5 V vs. SCE
3. Pulsed Voltammetry (PV) for 200 cycles of +0.9 V and -0.85 V vs. SCE followed by activation protocol 2 (80 CV cycles)

4.4.3 Results

Cyclic Voltammograms were recorded using an external Ag/AgCl wire electrode and an on-chip IrO_x reference electrode (Fig. 4.8) in solutions containing 100 μM and 1 mM dopamine. Voltammograms obtained with the two electrodes were nearly identical except for an offset of 40 mV. This offset can be attributed to the difference in the reference potentials of Ag/AgCl (0.222V) and IrO_x (0.180V at pH 7.3) electrodes versus a SHE. During a 23 day soak test, the open circuit potentials of the activated IrO_x electrodes and a commercial glass pH electrode (control) were recorded versus a commercial double junction Ag/AgCl reference electrode (Orion). The electrodes activated using both CV and PV were found to have the most stable electrode potential, varying less than ±50 mV during the first 15 days of the test (Fig. 4.9b). This variance in reference potential is large enough to introduce significant errors in electrochemical measurements during long term chronic recordings unless the electrode is periodically calibrated. One possible solution

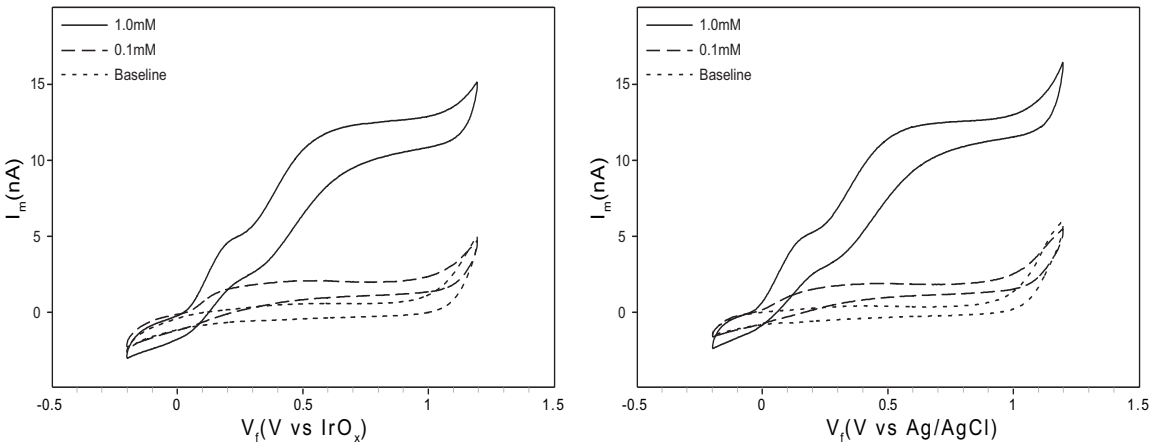

Figure 4.8: Comparison of IrO_x and Ag/AgCl reference electrodes. Cyclic Voltammograms of dopamine taken using an Ag/AgCl wire (right) and an on-chip IrO_x electrode (left). Both experiments gave similar results in both detection levels and half-wave potentials except for an offset of approximately 40 mV between the half-wave potentials of dopamine for the two different electrodes. ©2005 IEEE. Used with permission from [Franklin05].

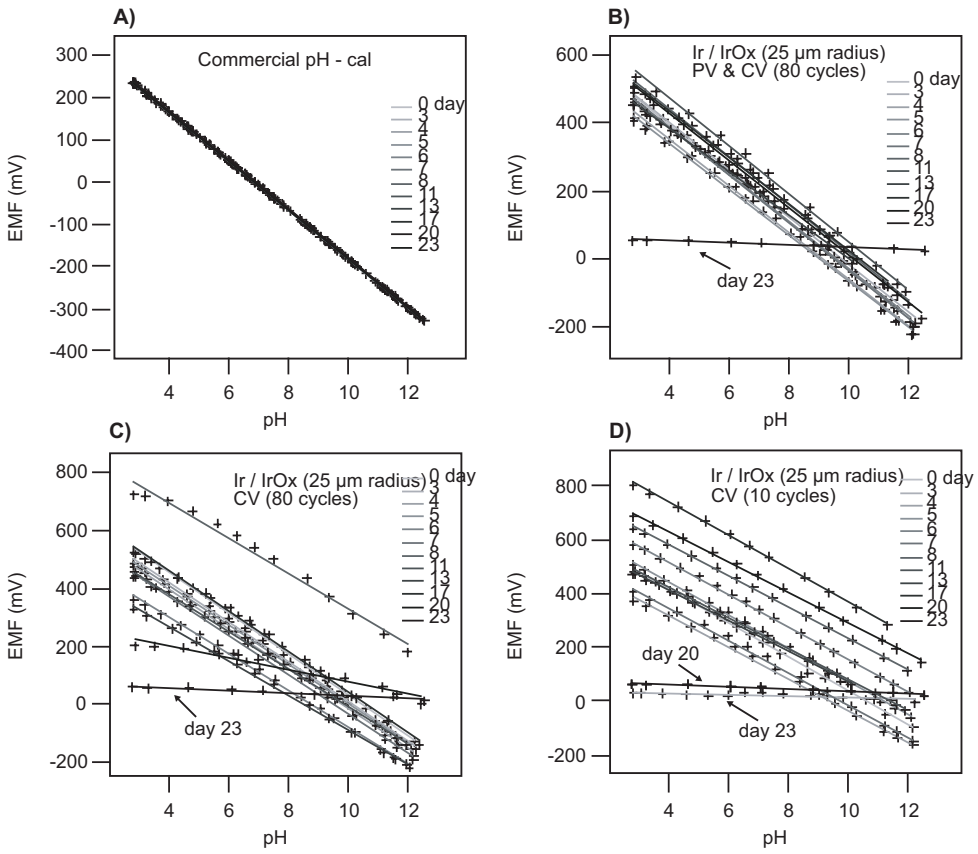

Figure 4.9: pH response of four electrode types. pH stability of a commercial glass electrode (a) and on-chip IrO_x electrodes during a 23 day trial. The IrO_x electrodes for this trial were activated by either (c, d) cyclic voltammetry (CV), or (b) a combination of both Cyclic Voltammetry and Pulse Voltammetry. The slope of the glass electrode was steady at 58 mV/pH while the slope of the best IrO_x electrodes (b) was found to be 68 mV/pH. All of the IrO_x electrodes failed on or before the 23rd day, terminating the test. The failure was most likely due to failure in the encapsulation. ©2005 IEEE. Used with permission from [Franklin05].

for in vivo calibration could involve periodic injections of calibration solution using a probe with an integrated microfluidic channel [Chen97]. All of the electrodes functioned properly until day 20, when a rapid deterioration in pH response was noted for all of the IrO_x electrodes (Fig. 4.9). This lifetime is significantly shorter than the lifetime (months to years) reported for other IrO_x electrodes [Cogan02, Ziaie96] and is most likely due to inferior encapsulation in both the SiN_x layer and water uptake of the MED-4211 silicone encapsulant.

4.5 Conclusion

This chapter has presented the feasibility of using IrO_x thin film electrodes as reference electrodes for in vivo neurotransmitter detection. The characteristics of IrO_x electrodes have been studied using in vitro preparations and several methods of fabricating suitable electrodes have been presented. Results from cyclic voltammetry studies of dopamine indicated the viability of this system, and soak testing showed that IrO_x electrodes fabricated according to the methods presented in this paper are viable for electrochemical work for periods of time less than two weeks. However, the effects of interfering redox species such as ascorbic acid still need to be studied. Other researchers have shown that IrO_x electrodes exhibit low sensitivity to these species, and Nafion coatings have been used successfully to further reduce the sensitivity of IrO_x pH electrodes to interferants such as ascorbic acid [Johnson07, Marzouk98], but further characterization of IrO_x in the specific context of in vivo reference electrodes still needs to be performed. Additionally, longer term studies and in vivo preparations still need to be done to understand the effects of biofouling on the electrode response and to identify ways of increasing the stability of the electrodes.

Chapter 5

Probe Design, Fabrication, and Testing

5.1 Introduction

During the course of this work, the author designed, fabricated, and tested several generations of probes, probe-like structures, and test structures. Most of these designs were created in collaboration with researchers from various labs including Dr. Daryl Kipke's lab at the University of Michigan and Dr. Hakhyun Nam and Dr. Geun Sig Cha's lab at Kwangwoon University in Korea. This chapter discusses the design, fabrication, and testing of these structures.

In selecting an appropriate technology to pursue in vivo electrochemical sensors, several competing technologies were evaluated. A microfabricated probe is desirable for this application in order to facilitate mass production and in order to improve reproduceability. Of the different microfabricated neural probes, Michigan style neural probes and the Utah Electrode Array are the most common. While the underlying chemical sensing technology can theoretically be applied to both types of neural probes, Michigan-style probes were chosen because their planar fabrication allows the placement of multiple electrode materials in close proximity (<10 μm between electrodes). This close proximity enables the simultaneous recording of electrical and chemical signals from a single popu-

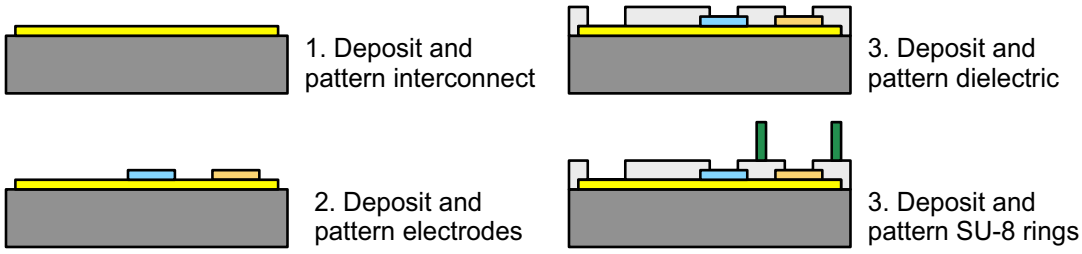

Figure 5.1: Simplified test structure fabrication process. (The fabrication of the test structures was kept as simple as possible to ease fabrication. The basic process had three masks plus one extra mask for each electrode material. Au was normally used for the interconnect with a PECVD silicon nitride dielectric layer. Electrodes were made from a variety of materials including Pt, Ir, IrO_x, and C.

lation of neurons and enables the study of chemical micro-gradients in a small area (see Figs. 5.5 and 5.15). Neither of these techniques would be possible using a larger technology like the Utah Neural Array (~100 μm between electrodes). Additionally, depositing more than a single electrode material on the Utah array can be tricky and would most likely require a complex electrodeposition step instead of a simpler PVD technique. In light of these advantages, the Michigan neural probe platform was chosen for the present work.

5.2 Test structures

During the course of this work, three generations of test structures were fabricated. The fabrication process for these test structures was kept as simple as possible in order to facilitate rapid development and testing. The process is shown in abbreviated form in Fig. 5.1. For a more detailed description of the process, please see the sample run sheet for the third generation of structures in Appendix A. The test structures were primarily geared at bench top in vitro testing, and were part of an iterative process used to develop methods and materials for in vivo testing.

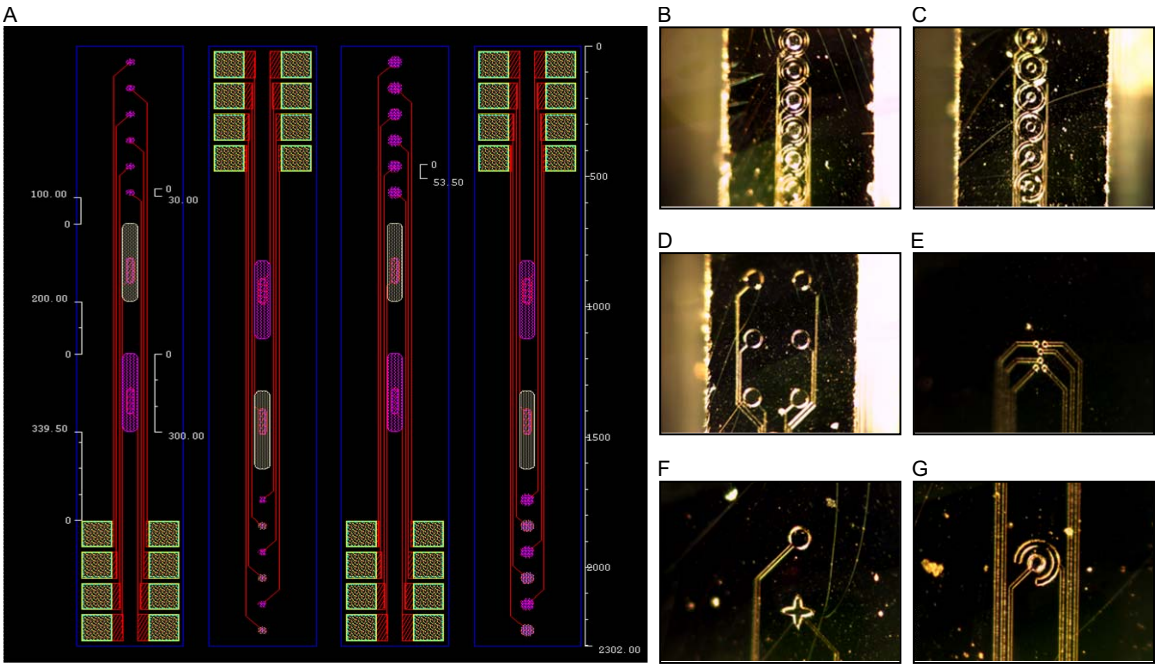

Figure 5.2: Gen1 test structures. (A) Shows the layout and dimensions for some of the Gen1 probe designs. (B)-(G) Show micrographs of the first generation of test structures. (B) & (C) were designed to study site selective coatings and the effect of electrode sizing on the measured faradaic current. (D) & (E) were designed to measure chemical gradients and test electrophysiology and chemical recordings in close proximity. (F) was designed to increase the steady state current of the electrode by increasing the perimeter to surface area ratio. (G) was designed to study the effect of placing the working electrode and counter electrode in close proximity.

5.2.1 Gen1 test structures

The first generation of test structures were geared at a wide array of experiments including measuring chemical micro-gradients, determining sensitivity and diffusion coefficients, and developing site selective coating processes. The layout and several example electrode structures are shown in Fig. 5.2. The Gen1 structures as well as the Gen2 structures were designed to mimic the form factor of Michigan neural probes, but were singulated using a dicing saw instead of an EDP release. The form factor was kept as similar as possible to the standard form factor of the Michigan neural probes in order to facilitate porting the designs to Michigan neural probes as described in Section 5.3 and to keep any

parasitic effects (such as the interconnect resistance) as similar as possible to those of the actual probes. These probes were used in a variety of studies investigating methods for detection of dopamine and choline. Some examples of the studies done with these probes which demonstrate their ability to detect neurochemicals are described in the following two sections.

5.2.1.1 Dopamine studies using the Gen1 probes[1]

Using the Gen1 probes, Nafion coatings were studied and optimized to improve selectivity to dopamine in the presence of common interferants such as ascorbic acid. The resulting improvements to sensitivity and selectivity are shown in Fig. 5.3. The process as well as several results from the following paragraphs were reported in detail in [Johnson05] and the author gratefully acknowledges the help of Dr. Matt Johnson in collecting this data. Several different coating processes were evaluated during this work including dip coating, syringe dispensing onto individual sites, and electrodeposition. Each of these processes has advantages and disadvantages. For example, the dip coating is the easiest, but it coats all of the electrodes on the probe eliminating the possibility of site specific coatings. The final process selected for this work involved electroplating the working electrode sites with platinum black at 20 mA/cm^2 for 600 s in Kohlrausch's solution (0.025 N HCl with 3% PtCl) followed by electro-depositing a Nafion coating on individual electrodes [Johnson05]. Before, during, and after the coating, platinum sites designated for neurochemical detection were calibrated for dopamine. Dopamine sensitivity increased by 52% following platinum black electroplating and by an additional 22%

1. Section 5.2.1.1 is based on "Neural probes for concurrent detection of neurochemical and electrophysiological signals in vivo," by M. Johnson et al. which appeared in Proceedings of the IEEE Engineering in Medicine and Biology Society. ©2005 IEEE. Used with permission.

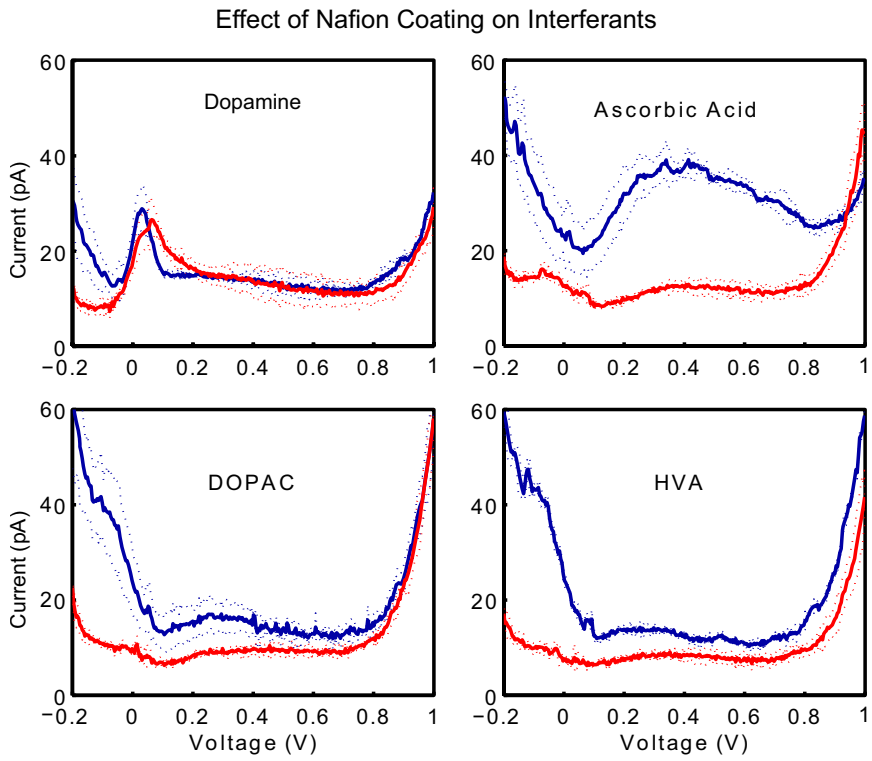

Figure 5.3: Effect of Nafion coatings on dopamine and interferant detection. Differential pulse voltammetry demonstrated enhanced dopamine (50 μM) selectivity after Nafion deposition. Interferants included ascorbic acid (400 μM), DOPAC (50 μM), and HVA (50 μM). Blue lines represent unmodified platinum; red lines signify Nafion-coated sites. Dotted lines represent standard deviations (n=4). ©2009 IEEE. Used with permission from [Johnson05]

following Nafion deposition (Fig. 5.4A). Sensitivity for dopamine on processed sites was 20.8 pA/μM with an R^2 of 0.98.

Both the electroplating and the Nafion coating processes had little effect on adjacent sites as shown in Figs. 5.4B and 5.4C. Electrochemical Impedance Spectroscopy (EIS) performed on platinum sites demonstrated a decrease in impedance after electroplating and a resistive shift after Nafion electro-deposition. While the modifications decreased the 1 kHz impedances of platinum sites by 201% (0.598 to 0.199 MΩ, paired t-test, $p<0.001$, $n=4$), adjacent iridium sites had only a 16% attenuation (1.33 to 1.14 MΩ, paired

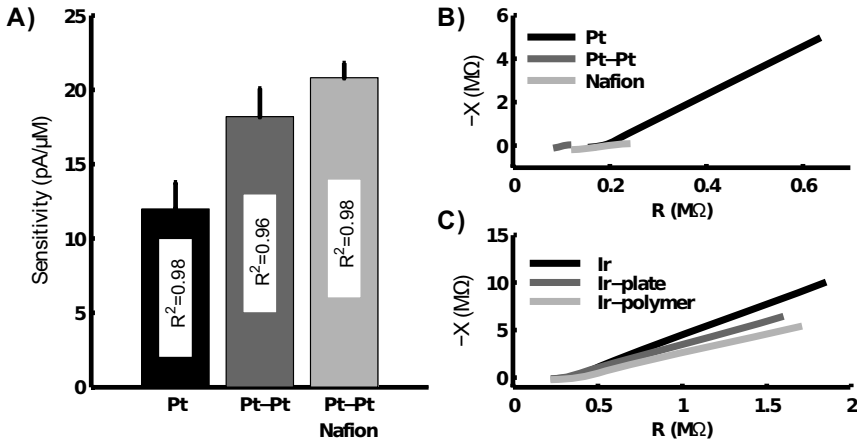

Figure 5.4: Sensitivity following Nafion coating. Calibration analysis. (A) Dopamine sensitivity increased significantly after platinum-black electroplating (paired t-test, p=0.009, n=4) and Nafion electro-deposition (paired t-test, p=0.002, n=4). Error bars represent standard deviations. (B) Impedance spectroscopy curves of an unmodified (black), electroplated (dark gray), and Nafion-coated (light gray) platinum site. (C) Little change in impedance spectroscopy curves was evident on adjacent iridium electrode sites. ©2005 IEEE. Used with permission from [Johnson05].

t-test, p=0.01, n=6). Such impedances are well within the normal range used for recording electrophysiological activity [Johnson05B].

Common interferants to the detection of dopamine include ascorbic acid (AA), 3,4-dihydroxyphenylacetic acid (DOPAC), and homovanillic acid (HVA). In order to improve detection limits in the presence of these interferants, the electrode surface must be modified to either change the oxidation potential of the interferant or to prevent the interferant from reaching the platinum surface. The Nafion coatings facilitate both of these modifications. After Nafion electro-deposition, sensitivity to interferants decreased on average by 89.3% for AA, 92.7% for DOPAC, and 92.2% for HVA. In contrast, sensitivity to dopamine increased by 16.4%. This increase in selectivity is due to the cation exchange properties of Nafion which allow transport of cations such as Dopamine to the electrode surface while rejecting anions such AA. Examples of individual analyte infusions prior to and after Nafion electro-deposition were shown earlier in Fig. 5.3.

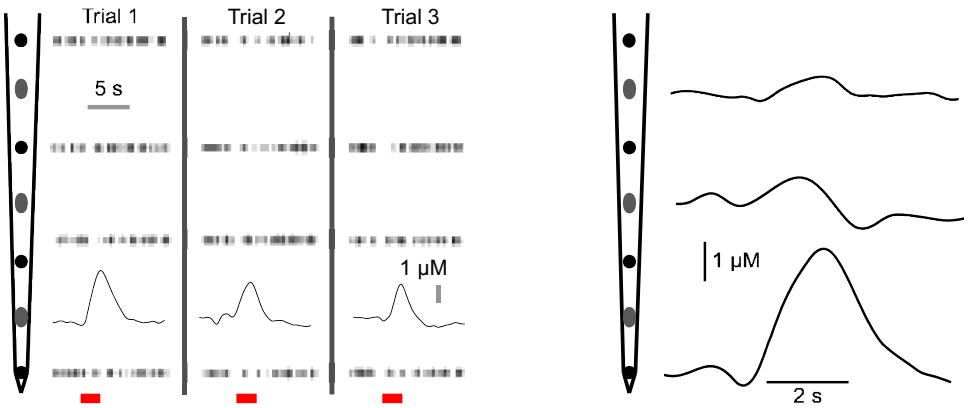

Figure 5.5: Concurrent dopamine and electrical recordings. Concurrent multi-modal recordings during anesthesia (left). Unit spiking activity was recorded across four Ir sites (black) concurrently with dopamine measurements at a Pt site (grey). Spiking activity is represented by the bars next to each electrode. The dopamine efflux was repeatable across three trials. Measurement at multiple sites was used to determine the presence of dopamine gradients along the probe shank for consecutive stimulation trials (right). These data support the existence of phasic dopamine concentration gradients within 300 μm. Traces are scaled to account for small variances in site sensitivity.

This process was first optimized using the Gen1 probes and then migrated to the implantable chemical sensing neural probes described earlier and used for several acute in vivo studies in Dr. Kipke's lab. These studies examined pathways important to the pathology of Parkinson's Disease. Examples of the in vivo results are shown in Figs. 5.5 and 5.6. These studies demonstrated concurrent detection of dopamine and neuronal spiking activity and laid the groundwork for the more detailed studies reported later in Section 5.5.

5.2.1.2 Choline studies using the Gen1 probes

The Gen1 probes were also used by collaborators in Dr. Kipke's lab to perform preliminary studies on choline sensors. These sensors utilized the enzyme choline oxidase to catalyze the conversion of choline to betaine aldehyde via the following reaction:

$$\text{Choline} + O_2 \Leftrightarrow \text{betaine aldehyde} + H_2O_2 \ .$$

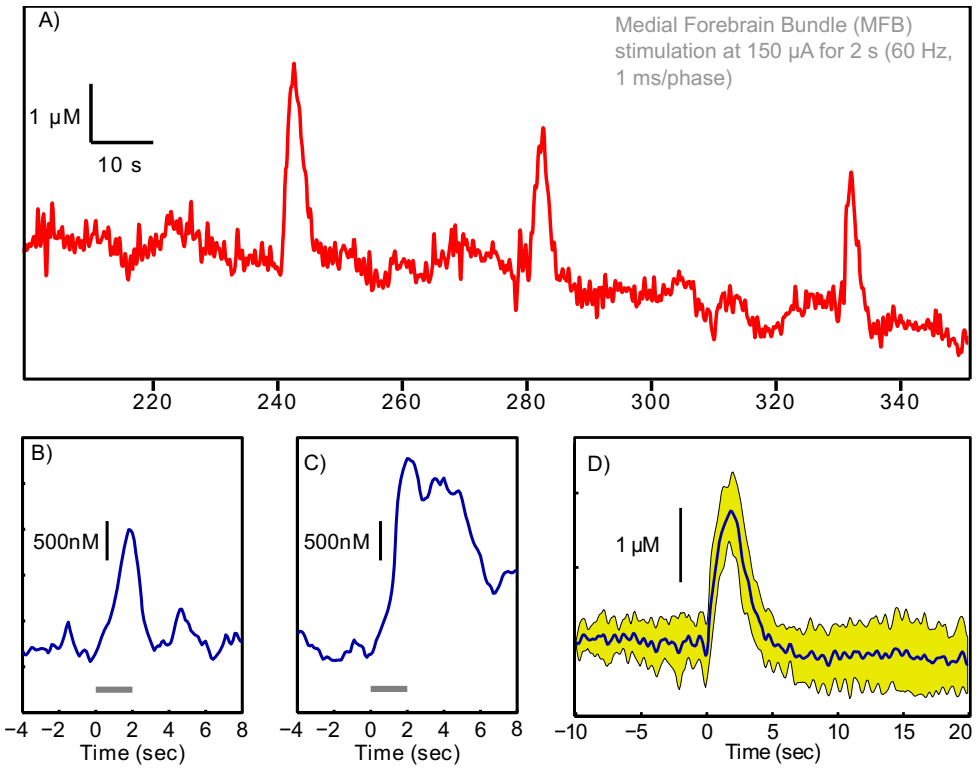

Figure 5.6: Dopamine recordings during MFB stimulation. Examples of dopamine efflux during medial forebrain bundle (MFB) stimulation. (A) shows a raw electrochemical trace of three stimulus-induced dopamine efflux sessions. (B) and (C) Demonstrate the effect of intraperitoneal injection of nomifensine, a dopamine reuptake inhibitor. The measured dopamine efflux was significantly less before injection (B) than it was 15 minutes after the injection (C). (D) shows an average of six dopamine efflux waveforms (blue line) with the standard deviations shown in yellow. For this implant location, peak dopamine was ~2.5 µM

The H_2O_2 by-product of the reaction is able to be adsorbed and oxidized at the electrode surface to produce a faradaic current. Figs. 5.7 and 5.8 show preliminary in vitro and in vivo data which were reported at an internal WIMS IAB conference in 2006. The data includes calibration data for choline biosensors as well as in vivo data collected from the prefrontal cortex. These sensors still need further characterization. In particular, ascorbic acid and other redox species present in the brain are significant interferants for these sensors and their effects will need to be addressed in future work. One possible solution may be to use size selective coatings to screen out larger molecules (e.g. ascorbic acid) while

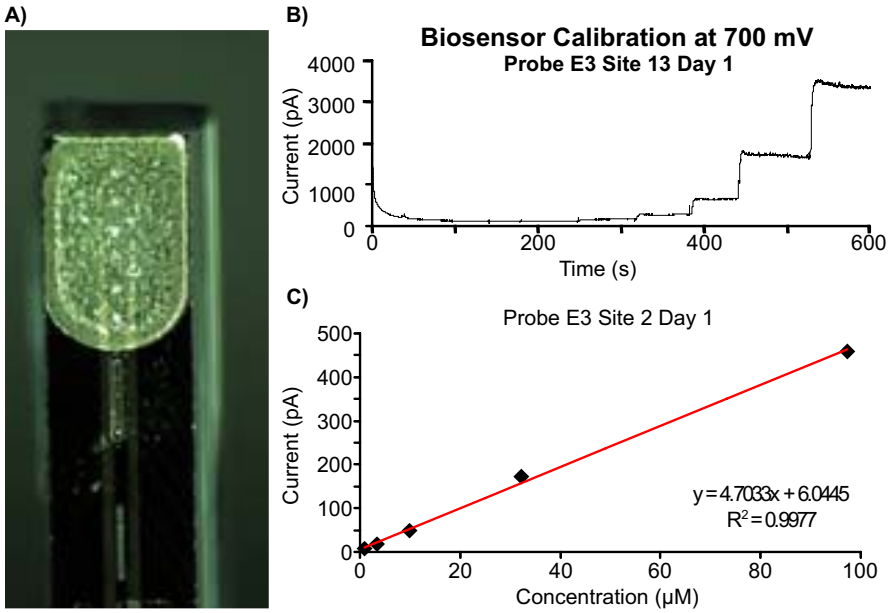

Figure 5.7: Choline recording electrodes. Micrograph of a test structure device coated with a cross-linked enzyme mixture for choline detection (A). Calibration curves on the right (B,C) demonstrate a sensitivity of 4.7 pA/μM

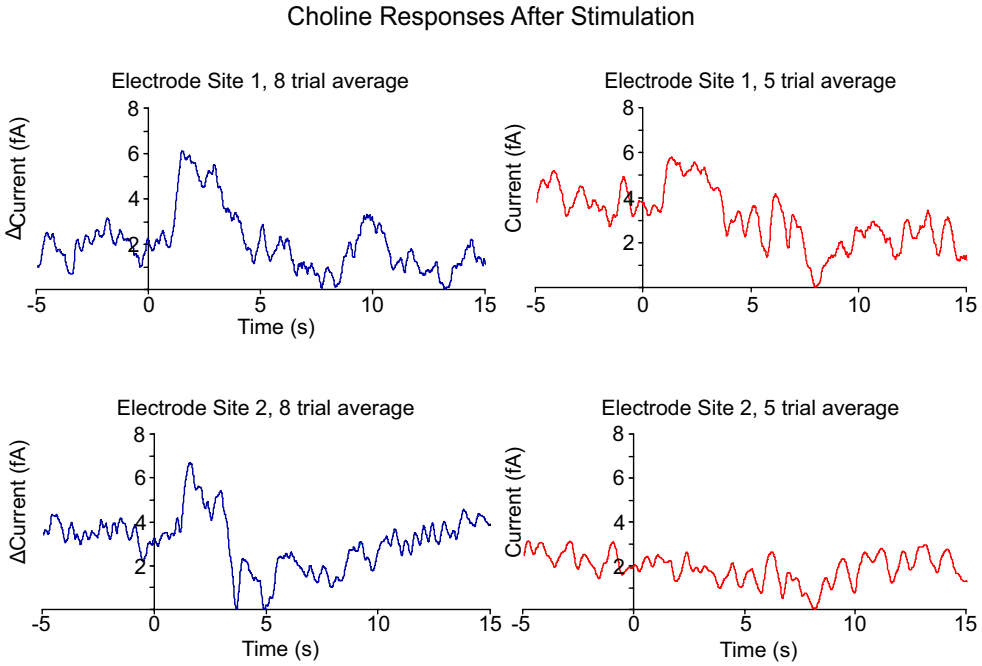

Figure 5.8: In vivo choline detection. Stimulation of the substantia innominata, a cholinergic cell group in the basal forebrain that projects to the prefrontal cortex, revealed transient peaks in cortical choline. Choline efflux was heterogeneous across the array. This pathway is involved in the pathology of Alzheimer's Disease.

still allowing smaller molecules such as H_2O_2 to reach the surface of the electrode. The author gratefully acknowledges Dr. Matt Johnson and Matt Gibson for their assistance in collecting these data.

5.2.2 Gen2 test structures

The second generation of test probes was redesigned based on feedback from researchers that used the first generation of test structures. A layout of the probes is shown in Fig. 5.9. There were three basic designs in this generation: stereotrode probes, super-sizeme probes, and tetrode probes. The stereotrode probes were designed for simultaneous recording of both electrical and chemical signals and exploration of self referenced chemical sensing techniques [Burmeister01]. The SuperSizeMe probes were designed to provide several different size electrodes on a single probe for examining the effect of sizing on measured faradaic current. The SuperSizeMe electrodes also included SU-8 rings to ease application of site selective coatings. The Tetrode probes were designed to monitor

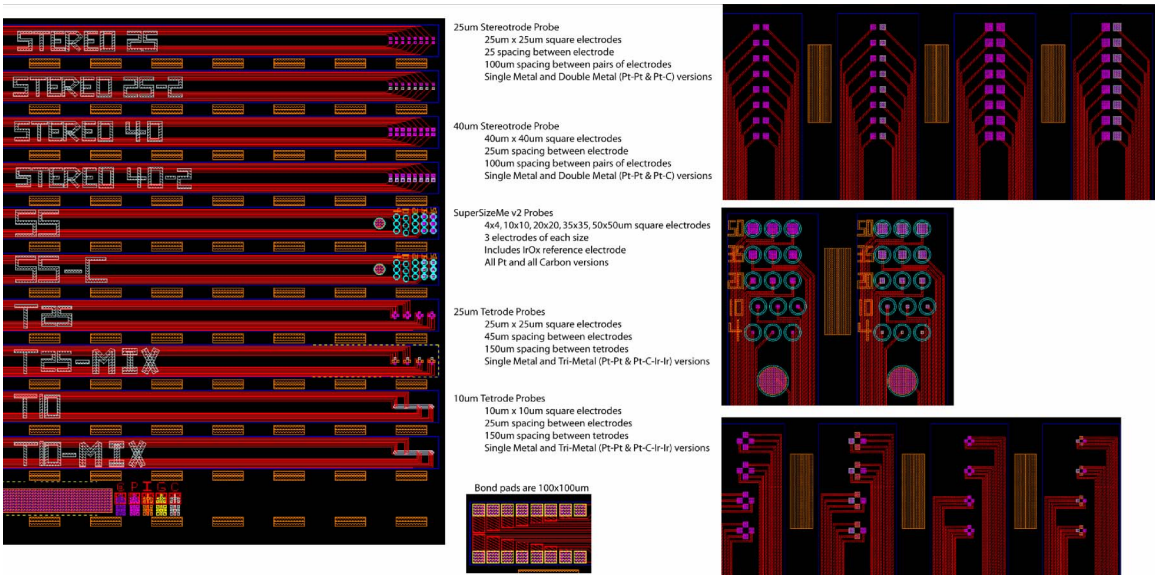

Figure 5.9: Gen2 test structures. Full layout of the Gen2 test structures. The text in the middle describes the size and materials used for each design.

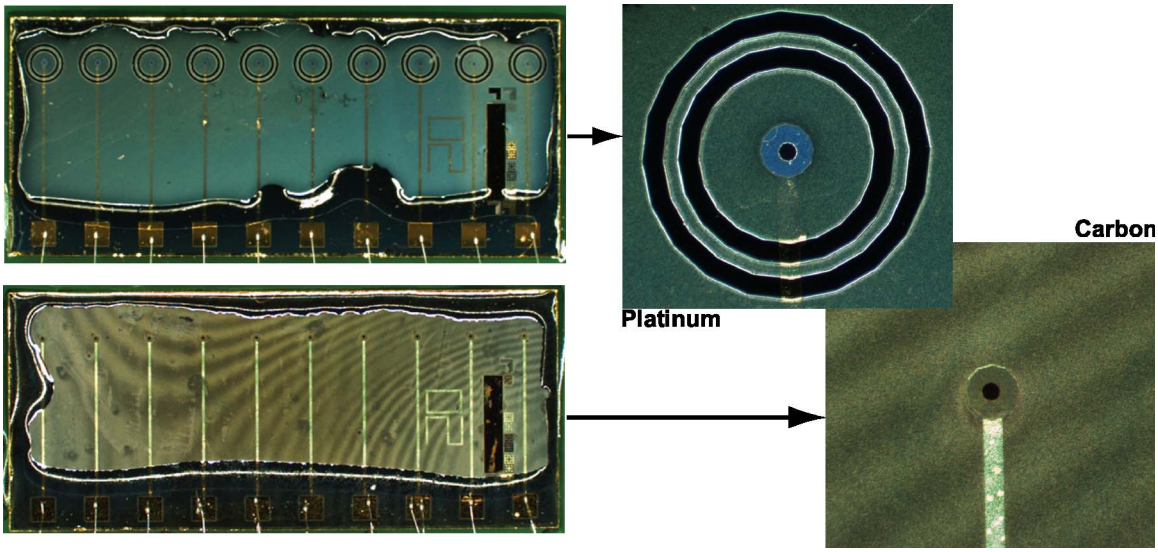

Figure 5.10: Gen3 test structures. The micrographs above show Gen3 test structures with both carbon and platinum electrodes. Each die had ten 20 μm diameter disk electrodes.

chemical gradients, multiple site selective coatings, and tightly spaced electrical and chemical electrodes. Of the three designs in the second generation, the tetrode probes were the most successful and were eventually used on in vivo parylene probes [Pellinen05] and a batch of silicon chemical sensing probes fabricated by NeuroNexus. These test structures were also used for the IrO_x studies reported in Section 4.4 on page 51.

5.2.3 Gen3 test structures

While the first two generations of test structures were geared primarily at testing various geometries and electrode configurations, the third generation of test structures was geared at testing electrode materials. The primary materials studied on these electrodes were sputtered carbon films, platinum, and IrO_x. Micrographs showing both carbon and platinum electrodes are shown in Fig. 5.10. These test structures were fabricated using almost the same process as was used for the Gen1 and Gen2 test structures. The process used three masks to define the interconnect layer (Au), the electrode sites (C, Pt, or IrO_x),

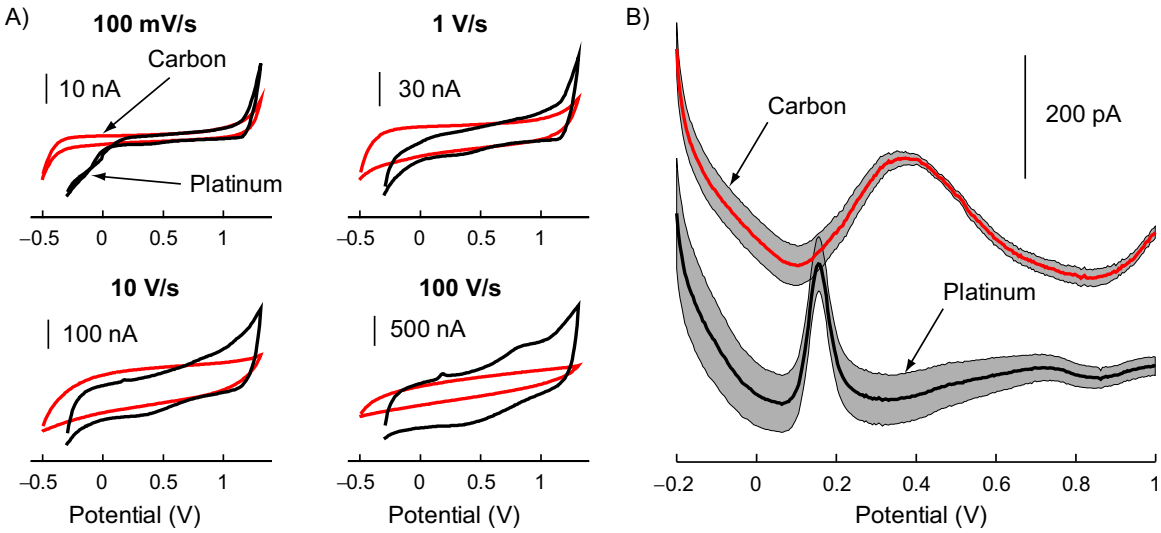

Figure 5.11: Comparison of platinum and carbon electrodes. These figures show a comparison of carbon and platinum electrodes using Gen3 test structures. (A) compares of the dynamic range of each material and the effect of scanning voltage in 0.1 M PBS. (B) demonstrates the detection of dopamine of each material using pulsed voltammetry in a 0.1 M PBS solution with 100 mM of dopamine. The author would like to acknowledge Dr. Matt Johnson for his assistance in collecting these data.

and the contact openings for the electrodes and bond pads. An additional mask was also used on a couple of runs to add SU-8 rings to the devices. The Gen3 devices were also designed as larger die to facilitate handling and packaging. The largest change to the Gen3 fabrication process was that in addition to the SiN_x dielectric layer used on the Gen1 and Gen2 test structures, a thin layer (<1 μm) of parylene was added to the dielectric covering on the structures. This parylene was added to fill any small pin holes in the PECVD SiN_x layer and to prevent dissolution of the SiN_x in saline during long term soak testing [Maloney05]. Detailed fabrication steps including equipment used and deposition parameters for the Gen3 test structures with IrO_x electrodes can be found in Appendix A.

Results comparing dopamine detection on both carbon and platinum electrodes can be seen in Fig. 5.11. A 250 nm thick layer of sputtered carbon was used for these stud-

ies. The carbon film was deposited in a Denton Discovery 18 sputtering system (80 mW, 25 mT, 45 min). Cyclic voltammetry experiments with the carbon electrodes showed that they were more polarizable than similar platinum electrodes (Fig. 5.11A). The carbon electrodes also had a greater overpotential for the detection of dopamine using pulsed voltammetry (Fig. 5.11B), and for the same scan rates, the carbon electrodes had a much broader peak, indicating a slower surface reaction than at the surface of the platinum electrodes. Because of these initial poor results, sputtered carbon was not investigated further as an electrode material. However, carbon is still an interesting electrode material and carbon fiber electrodes are in many ways the gold standard for in vivo voltammetry. Alternative deposition methods such as packing carbon paste into an SU-8 ring or using an all CVD diamond probe [Chan09] may still create superior electrodes and these methods merit further investigation.

Several studies were also conducted on IrO_x films using the Gen3 test structures. The results of these studies were discussed in Section 4.3 on page 45 and reported in [Franklin09]. Additionally, the Gen3 test structures were used by Dr. Kipke's group to study membranes for glutamate sensors and other enzyme modified electrodes. Finally, Dr. Hakhyun Nam's research group at Kwangwoon University in Korea is currently using the test structures for development of a new epoxy-based micro-reference electrode.

5.3 Implantable probes

Based on feedback from users of the test structures, a set of implantable silicon probes were designed and fabricated. The designs were based on the University of Michigan's current probe designs and were fabricated as part of a probe run by the Center for

Neural Communication Technology (CNCT). Two masks were added to the process to add Pt and Ag electrodes in addition to the standard Ir electrodes on the CNCT probes.

Layouts for the probes are shown in Fig. 5.12. The probes shanks varied in length from 4.35 mm to 10 mm with channel counts of 6, 16 or 32 channels. The electrical recording electrodes were Ir which was activated to form IrO_x after fabrication, and the

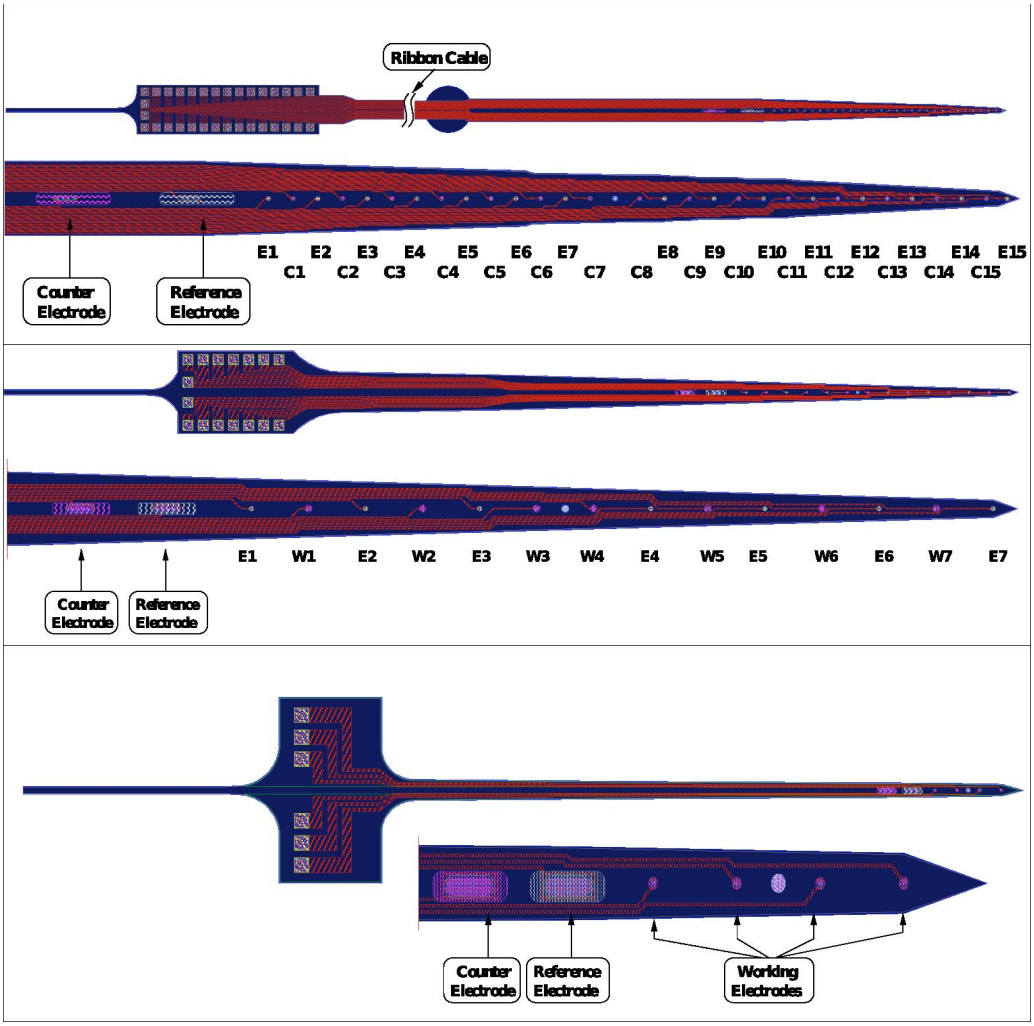

Figure 5.12: Implantable chemical probes. The layout for three implantable chemical probes is shown. Each electrode is 16 μm in diameter with a center-to-center spacing of 100 μm.
(Top) A 32-channel chronic probe with 15 chemical recording electrodes, 15 electrical recording electrodes, and integrated reference and counter electrodes. The probe has a 14 mm long silicon ribbon cable and 7 mm long shank.
(Middle) A 16-channel acute probe with 7 chemical recording electrodes, 7 electrical recording electrodes, and integrated reference and counter electrodes. The probe has a 10 mm long shank.
(Bottom) A 6-channel acute probe with 4 chemical recording electrodes and integrated reference and counter electrodes. The probe has a 4.25 mm long shank.

chemical recording electrodes were Pt. Both types of electrodes alternated down the shank of the probe and were spaced 100 μm apart. The electrodes were sized at 16 μm in diameter giving a total exposed surface area of 201 μm^2. The probes also featured integrated counter and reference electrodes (1000 μm^2). The counter electrodes were Pt and the reference electrodes were either Ag (post processed to form Ag/AgCl) or Ir (post processed to form IrO_x). These probes were used in the IrO_x study described previously in Section 4.4 on page 51 as well as in the in vivo studies which comprise the remainder of this chapter.

5.4 Discussion

Several generations of probe and probe-like structures have been discussed in this chapter. The development of those materials has enabled studies of in vivo chemical dynamics, comparisons of electrode materials and fabrication methods for carbon, platinum, and IrO_x electrodes, and the development of new membrane materials for chemical detection. Following the initial development of materials and methods described thus far, a series of in vivo experiments were carried out. The rest of this chapter follows a journal article that the author helped Dr. Matt Johnson to prepare for the Journal of Neuroscience Methods [Johnson08].

5.5 Implantable microelectrode arrays for simultaneous electrophysiological and neurochemical recordings

5.5.1 Introduction

The physiological basis for local field potentials (LFPs) is an increasingly significant question given the involvement of LFPs in neurological disorders [Bragin02], [Hammond07], the hemodynamic response of fMRI [Logothetis01, Mukamel05,

Niessing05], and neural prosthetic applications [Schwartz06]. Understanding the rhythmic generation and amplification of LFPs in the intact brain may benefit from techniques that can simultaneously monitor neurotransmitter dynamics. An approach to examine correlations between tonic neurotransmitter concentrations assessed through microdialysis and local field potentials (LFPs) has been suggested previously [Darbin06]. However, to examine high-frequency oscillations, which are often transient, sampling neurotransmitter levels requires a faster approach such as in vivo electrochemistry [Adams76, Boulton95].

Previous reports examining both electrochemical and electrophysiological signals in the same preparation have focused on single-unit spike activity and have employed either a 'serial' or a 'parallel' approach. The former consists of toggling between recording modalities with a single microelectrode [Armstrong84, Cheer05, Crespi95, Ikeda85, Stamford93, Williams90], while the latter involves continuously detecting each modality with separate, closely spaced microelectrodes [Bickford91, Hefti83, Su90]. The 'serial' approach has the advantage of sampling both types of signals from the same location, but it inevitably leads to under-sampling and can result in LFP filtering artifacts that can make concurrent recordings of low-frequency oscillations difficult to interpret. In combination with amperometric techniques, the 'parallel' approach resolves these issues, but can be problematic if the microelectrodes for each recording modality are not located within the same microenvironment. Developing a neural probe with precise and closely spaced microelectrode sites is a well-suited problem for microfabrication [Wise70].

Recent advances in microfabrication processes have enabled the development of microelectrode arrays with highly reproducible geometrical and electrical characteristics. These devices have facilitated sampling electrical activity of the same neuron from multi-

ple perspectives [Blanche05, Drake88] as well as different neurons across multiple microenvironments [Buzsaki04a, Csicsvari03]. Moreover, with certain microelectrode materials such as platinum [van Horne90] or carbon [Sreenivas96], these arrays are capable of detecting phasic changes in neurotransmitter levels in the extracellular space through electrochemical techniques such as amperometry [Burmeister00].

Here, we describe an intracranial, silicon-substrate probe that facilitates concurrent recordings of LFPs and spikes on one set of microelectrodes [Blanche05] and detection of extra-synaptic dopamine dynamics on an adjacent set of microelectrodes through constant potential amperometry [Kawagoe94, Pennington04]. These multi-modal probes were implanted in the striatum of urethane-anesthetized rats to examine (1) reciprocal influences of amperometry on neuronal activity and (2) spatiotemporal characteristics of dopamine efflux and LFP/spike activity following electrical stimulation of the medial forebrain bundle (MFB).

5.5.2 Materials and methods

5.5.2.1 Microsensor array fabrication

Microfabrication of silicon-substrate probes involved an eight-mask process, including selective boron diffusion in silicon to define the probe geometry; patterned deposition of thin-film dielectrics, traces, and conductors; and subsequent probe-wafer release in ethylenediamine-pyrocatechol [Drake88]. The devices developed for this study consisted of a single 7 mm long shank with a linear array of microelectrode sites (Fig. 5.13). Along the shank, the majority of sites alternated between iridium (177 μm^2) and platinum (450 μm^2) for transduction of electrophysiological and amperometric signals, respectively. Center to center site separation was 200 μm, which facilitated multi-modal record-

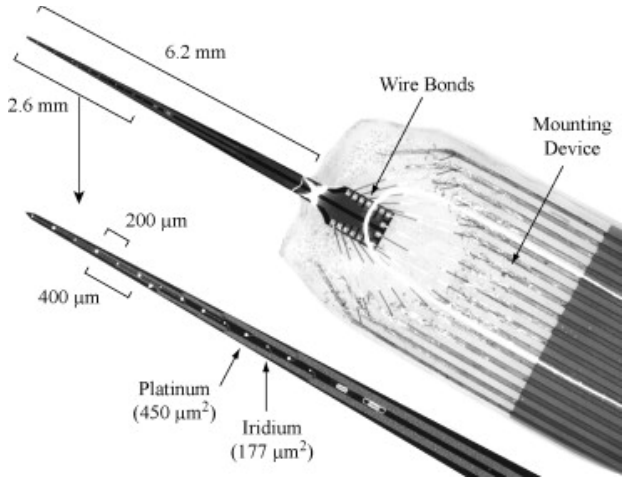

Figure 5.13: Micrograph of microelectrode arrays. Linear microelectrode arrays implanted in rat dorsal striatum recorded unit-spike and local field potential activity on iridium sites (177 μm^2) with adjacent platinum sites (450 μm^2) used for measuring electrochemical dopamine overflow signals through constant potential amperometry. Arrays were fabricated from a boron-doped, silicon substrate with metal contacts and phosphorus-doped polysilicon traces insulated with a multi-layer stack of silicon dioxide and silicon nitride.

ings while limiting putative amperometric cross-talk between channels [Yu00]. Arrays were attached to a 16-channel printed circuit board (PCB) with hot wax. Array bond pads were then wire-bonded with gold wire to the PCB and insulated with a silicone elastomer (MED-4211; Nusil Technology, Carpenteria, CA, USA).

5.5.2.2 Surgical procedures

Ten male Sprague-Dawley rats (250-350 g) were anesthetized with an intraperitoneal injection of urethane (1500 mg/kg), placed in a stereotaxic frame with a base heating pad (myneurolab.com, St. Louis, MO, USA), and supplied with a steady flow of oxygen. Heart rate and blood-oxygen levels were monitored with a pulse oximeter. The surgical procedure involved opening three craniotomies including two on the right hemisphere over coordinates for the striatum (AP: 0-2 mm, ML: 1-3 mm) and the medial forebrain bundle (AP: -4.6 mm, ML: 1.4 mm) and one on the left hemisphere (AP: 1-3 mm, ML:

3-4 mm) for placement of an Ag/AgCl wire reference electrode [Paxinos05]. To facilitate probe implantation, dura mater was resected over both right hemisphere craniotomies. A bipolar stimulating electrode (MS308, Plastics One, Roanoke, VA, USA) was then lowered to the MFB target (DV: 7.8-8.1 mm). Reference electrodes were positioned between the dura mater and a piece of saline-soaked gelfoam (Pfizer, New York, NY, USA). Four auxiliary 316SS bone screws were also secured on the contralateral hemisphere with another bone screw placed 1 mm posterior to lambda for an electrophysiological recording ground. The array was then inserted quickly (0.5-1.5 mm/s) into the striatum through a micromanipulator to reduce acute tissue damage [Bjornsson06, Johnson07]. Recordings were made at least 30 min after device insertion to allow for tonic dopamine levels to equilibrate. Each rat was maintained in the stereotaxic frame placed inside a Faraday cage. All procedures complied with the NIH guidelines for the care and use of laboratory animals and were approved by the University of Michigan Committee on Use and Care of Animals.

5.5.2.3 Electrochemical recordings

Probes were dipped three times in the perfluorinated ion-exchange resin Nafion (Sigma-Aldrich; St. Louis, MO, USA) and dried at 200 °C for 5 min to improve selectivity of platinum sites for dopamine [Gerhardt01]. Site impedances at 1 kHz after Nafion deposition were 1.611 ± 0.094 MΩ at iridium sites and 0.579 ± 0.022 MΩ at platinum sites. Prior to and after the surgical procedures, each Nafion-coated platinum microelectrode was characterized for its sensitivity to dopamine (Fig. 5.14A) and selectivity over confounding analytes. In separate solutions of 0.1 M phosphate-buffered saline (pH 7.4, warmed to 37 °C), the microelectrode arrays were challenged with infusions of dopamine

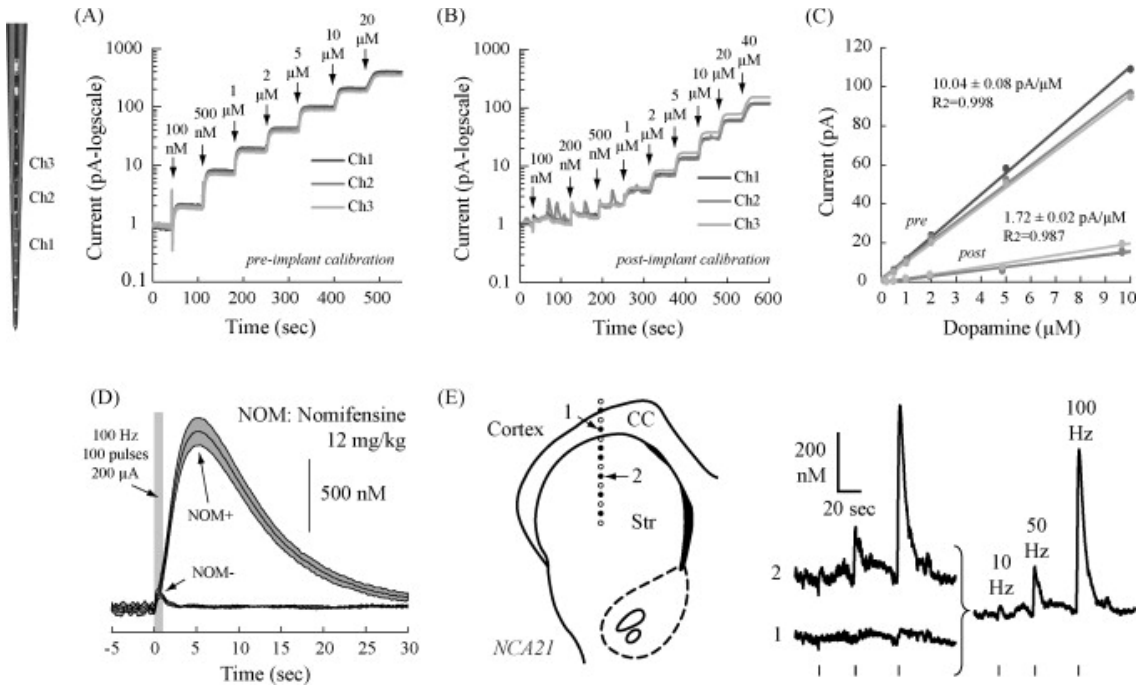

Figure 5.14: Dopamine measurements. Interfacial dopamine concentration was transduced at a platinum microelectrode with the constant potential amperometry technique, which involved applying a +500 mV potential with respect to an AgCl reference electrode. Simultaneous calibration across four channels of the array was performed (A) prior to and (B) after implantation with dopamine solution concentrations ranging from 100 nM to 20 mm. (C) In vivo amperometric recordings were transformed into a dopamine concentration with the post-implant calibration fits. Although sites were sensitive to dopamine after probe explantation, the sensitivity was decreased (paired t-test, $p = 0.013$, $n = 4$). (D) To verify that the electrically evoked in vivo electrochemical signals corresponded to changes in extra-synaptic dopamine concentrations, rats were injected i.p. with a dopamine uptake inhibitor (nomifensine, 12 mg/kg). Response curves represent an average of five trials with standard errors indicated by the gray fills. (E) MFB stimulation did not elicit detectable dopamine transients when a microelectrode site was positioned in the corpus callosum (CC), which contrasted with the large peaks observed simultaneously in the striatum (Str). Shown are three stimulation trials for 1 s long consecutive pulse trains using frequencies of 10, 50, and 100 Hz (150 mA, 2 ms duration biphasic waveforms). Subtraction of the two recordings decreased common noise between the two platinum microelectrodes.

(DA, 20 nM to 50 μm), ascorbic acid (AA, 1-200 μm), dihydroxyphenylacetic acid (DOPAC, 1-200 μm), and homovanillic acid (HVA, 1-200 μm). These analytes were detected through constant potential amperometry at +500 mV in reference to an Ag/AgCl glass body electrode [Kawagoe94, Pennington04]. Devices typically achieved selectivity ratios greater than 100:1 for AA, DOPAC, and HVA and DA detection limits of 200 nM

post-implantation, which were defined as current steps with a signal-to-noise ratio greater than three.

In vivo amperometry consisted of applying the same anodic potential versus an Ag/AgCl reference electrode and sampling the resulting current at 60 Hz through either a four-channel potentiostat (Biostat System, ESA, Chelmsford, MA, USA) or a single-channel potentiostat (PGSTAT12 Autolab, Eco Chemie, Utrecht, The Netherlands). Experimental stimulation of the MFB began once the non-faradaic charging current at each platinum site had reached approximately 1-5 pA (or ~30-60 min post-implantation). Electrochemical measurements were digitized and stored for offline analysis in MATLAB (Mathworks, Natick, MA, USA). Analysis of the arrays' sensitivity prior to implant and after explant showed a significant decrease in sensitivity from 10.04 ± 0.08 to 1.72 ± 02 pA/μM (Fig. 5.14A-C). Consistent with previous studies, we used the post-implant calibrations for assessing in vivo dopamine concentrations [Phillips03].

While confirmation that the amperometric currents corresponded exclusively to dopamine was unattainable [Phillips03], we did employ metrics to increase our confidence in the detected waveforms including verifying that the sensor selectivity ratios were greater than 100:1 for other oxidizable analytes. In vivo experiments comprised of electrically stimulating a fiber bundle containing dopaminergic neurons and subsequent recording in distal regions innervated by those fibers. In addition, we observed increased amplitude and duration in the electrically evoked signals following intraperitoneal injection of the dopamine uptake inhibitor nomifensine (7-12 mg/kg) (Fig. 5.14D) [Wightman90]. For striatal implants in which the distal recording site resided in or near the corpus callosum, little to no dopamine signal was detected after MFB stimulation

(Fig. 5.14E). Hence, subtraction of the residual background signal on this site from more distal amperometric signals in striatum removed 'noise' common to both microelectrodes, which is an approach similar to the self-referencing technique proposed by [Burmeister01].

5.5.2.4 Electrophysiological recordings and stimulation

Local field potential and spike recordings were made continuously across seven 177 μm^2 iridium sites, which were referenced to a bone screw positioned posterior to the cranial lambda mark. The location of this reference was chosen because of its distance from brain regions of high amplitude field potentials that might bias field potential measurements [Berke04]. For each recording session, Medusa or Pentusa amplifiers sampled voltage-time series data sets at 25 kHz with 16-bit resolution and band-pass filtering from 0.1 to 100 Hz for LFPs and 500 to 5000 Hz for spikes (Tucker-Davis Technologies, Alachua, FL, USA).

The medial forebrain bundle was stimulated through a bipolar electrode with a biphasic pulse train (10-100 pulses, 10-100 Hz, 2 ms pulse duration, 30-300 μA, [Wightman90]) triggered by an RV8 base station (Tucker-Davis Technologies) and delivered through a stimulus isolator (A-M Systems Model 2200, Sequim, WA, USA). Since the duration of stimulation was fixed (1 s), the number of pulses within the stimulation train scaled with the frequency of the stimulation. Identical trials with inter-trial periods of at least 100 s were repeated 5-10 times for each location sampled within the striatum [Michael87], after which a different set of stimulation parameters were repeated such that the parameter sweep varied randomly among implant depths and animals. Time stamps of stimulation onset were recorded and used to examine peri-event activity.

5.5.2.5 Statistical analysis

Current measured at each recording site was converted into dopamine concentration with each site's post-implant sensitivity to dopamine as shown in Fig. 5.14s. Recordings were analyzed for the maximum stimulation-evoked dopamine concentration across multiple trials. Peak amplitudes were first normalized by subtracting the current 100 ms prior to stimulation onset and then assessing significant differences between trials (ANOVA with subsequent post hoc Tukey tests, $p < 0.05$).

Power spectral densities of recorded LFPs were calculated to investigate changes in oscillatory activity concurrent with electrically evoked dopamine overflow. Event-averaged spectrograms of the LFP data were generated in MATLAB utilizing a segmented multi-tapered Fourier transform function (1 s window, 0.5 s steps, $NW = 3$, $K = 5$) with results averaged across trials (www.chronux.com). Each frequency band of a given spectrogram was baseline-subtracted with the average spectral response 5-10 s prior to stimulation. Typical response windows were 20-50 s in duration.

Unit-spike activity before and after electrical stimulation was sorted in Offline Sorter (Plexon, Dallas, TX, USA) using a combination of automated t-distribution expectation maximization and manual clustering. Inter-spike interval histograms (ISIs) and cross-correlograms were examined for each sorted waveform to verify that sorting did not inadvertently group or divide neurons between sorting clusters. Peri-stimulus time histograms (PSTHs) and raster plots for each sorted waveform were generated in NeuroExplorer (Nex Technologies, Littleton, MA, USA). To examine possible changes in firing rates during constant potential amperometry, PSTHs with 100 ms bins were compared 20 s prior to and 20 s during the applied bias potential for each neuron. Wilcoxon rank-

sum tests were then used to assess significant changes in the average firing rates ($p < 0.05$).

5.5.2.6 Histology

Following each experiment, rats were perfused with 100 mL of 0.1 M PBS followed by 300 mL of a 5% paraformaldehyde solution. Explanted brains were blocked around the striatum and the medial forebrain bundle implants. Striatal blocks were sliced in 10 μm coronal sections with a cryostat, stained for cell nuclei (Hoescht 33342, Invitrogen, Carlsbad, CA, USA) and in some cases also tyrosine hydroxylase (32-2100, Invitrogen) and μ-opioid receptors (ab10275, Abcam, Cambridge, MA, USA), and imaged to locate the probe tracts. MFB blocks were sliced in 50-100 μm sections with a vibratome, stained with cresyl violet, and imaged to determine the final placement of the MFB bipolar electrode.

5.5.3 Results

5.5.3.1 Effects of constant potential amperometry on spike and local field potential activity

A previous study found that chronoamperometric pulses with amplitudes less than +0.55 V did not influence unit-spike activity [Hefti83]; however, the effects of constant potential amperometry on neuronal activity in vivo remain unclear. In our study, microelectrodes sites spaced 200 μm to 2.4 mm from a voltage-biased platinum site were used to record spike and LFP activity during constant potential amperometry. When the electrochemical bias potential was first applied, the adjacent recordings often exhibited a transient electrical artifact lasting 3-5 ms. Unlike other amperometric and voltammetric

waveforms, however, constant potential amperometry produced no residual artifacts on adjacent or distal microelectrode sites.

Single and multi-unit spike recordings were analyzed for reciprocal effects during constant potential amperometry at +250 mV (n = 32), +500 mV (n = 25), and +750 mV (n = 24). The mean firing rates across at least five trials for each cell were calculated for 20 s prior to and 20 s during the electrochemical recordings. Only microelectrodes spaced 200, 600, and 1000 μm from a voltage-biased platinum microelectrode were used in the analysis. For the large majority of recordings, neuronal activity during amperometry showed no change in average firing rate. At the 250 mV potential, 2/32 neurons had a slight but significant inhibition during amperometry (0.72-0.40 Hz, $p = 0.032$ and 1.28-0.92 Hz, $p = 0.024$, Wilcoxon rank-sum test). Only 1/25 cells exhibited a significant change in firing rate during the +500 mV trials (0.25-0.58 Hz, $p = 0.040$). At +750 mV, 3/24 neurons showed a decrease in firing rate (0.28-0.00 Hz, $p = 0.008$; 3.38-0.78 Hz, $p = 0.016$; and 3.67-2.07 Hz, $p = 0.016$). However, potentials up to +750 mV at individual 450 μm^2 platinum sites did not generally affect neuronal firing rates ($p > 0.05$, two-way ANOVA). In terms of concurrently recorded LFPs, no significant changes in the LFP power spectra were apparent during constant potential amperometry ($p > 0.05$).

5.5.3.2 Spatiotemporal heterogeneity of electrically evoked striatal dopamine dynamics

Following repeated MFB stimulation trials, we observed peak striatal dopamine overflow signals with nearly identical responses (Fig. 5.15). These responses were examined across a range of stimulation intensities and frequencies. Higher stimulation amplitudes evoked progressively larger dopamine overflow with peaks 95% larger at

150-175 μA than at 100-125 μA (ANOVA, $p = 0.004$, $n = 28$ for seven different implants). Increasing stimulation frequency also resulted in detection of greater response magnitudes with the highest magnitudes generated with pulse trains at or above 100 Hz.

The multi-channel potentiostat used in these experiments permitted sampling from only four microelectrodes at any one time, but the probes themselves provided up to eight distinct locations for detecting dopamine dynamics. Multiple four-channel recording configurations were examined in which spacing between platinum recording sites ranged between 200 μm to more than 1 mm along the dorsal-ventral axis of striatum. A representative example of these recordings is shown in Fig. 5.15, in which spatially heterogeneous dopamine overflow across multiple regions of striatum was observed following electrical stimulation of the MFB. These differences were repeatable for multiple stimulation trials

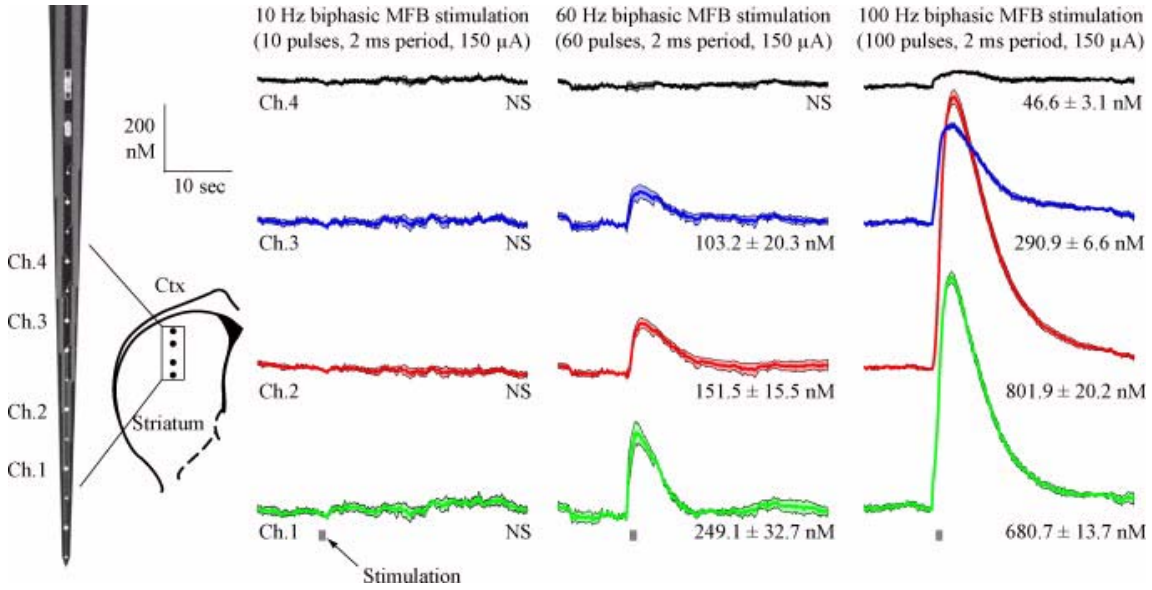

Figure 5.15: Concurrent electrochemical recordings. Concurrent electrochemical recordings across microelectrode sites within the striatum were characterized by spatially heterogeneous responses following MFB stimulation. Response curves exhibited different peak dopamine levels on sites as close as 200 μm and their magnitudes depended on stimulation frequency. Each trace corresponds to an average of five trials with fill bars indicating standard errors and gray bars indicating stimulus duration. Recordings reflect the presence of nomifensine (10 mg/kg).

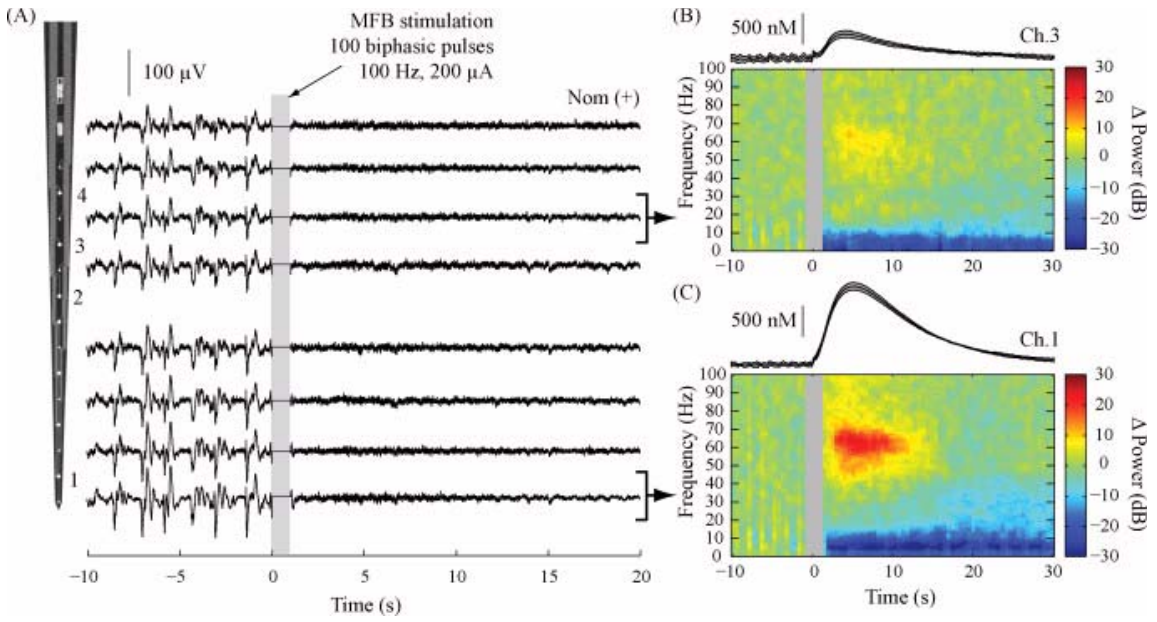

Figure 5.16: MFB stimulation elicited local field potential modulation in striatum. (A) The figure shows an example recording session sampled continuously during electrochemical recordings for dopamine on adjacent sites (indicated by numbers 1-4 next to the probe). Following MFB stimulation (indicated by the gray rectangle), slow-wave activity was suppressed considerably and coincided with the emergence of higher frequency activity. (B and C) event-averaged spectrograms showed significant modulation in the 0-20 and 40-90 Hz bands following stimulation (n = 5 trials). Above each plot is the event-averaged dopamine response recorded on an adjacent site. Recordings reflect the presence of nomifensine (10 mg/kg).

at the same striatal implant depth (n = 5 per location). Post-implant calibration of the platinum sites showed slight variation in sensitivity between sites; however, both raw amperometric measurements and calibration-converted waveforms demonstrated similar spatial response heterogeneity.

5.5.3.3 Concurrent recordings of dopamine overflow and striatal LFPs

Since platinum sites were held at a fixed potential, adjacent iridium microelectrodes could readily record local field potentials with no apparent cross-talk between conducting traces. Fig. 5.16 shows an example of these recordings during MFB stimulation, which induced transient and robust modulation of striatal LFPs. Prior to stimulation onset,

striatal LFPs exhibited slow-wave activity (0.1-4 Hz), which was characteristic of urethane anesthesia [Magill06] (Fig. 5.16A). After MFB stimulation, however, activity in this band was suppressed for more than 20 s. These responses were repeatable for consecutive stimulation trials provided that the trials were not performed more than once per minute [Michael87]. In general, stimulation at 10 Hz (10 pulses) depressed slow-wave activity for only 5-10 s, whereas stimulation at 100 Hz (100 pulses) reduced slow-wave activity for 30-60 s. In conjunction with these dynamics, the arrays often detected spatially heterogeneous gamma-band activity (40-90 Hz) and as shown in the baseline-subtracted spectrograms (Fig. 5.16B and C), regions with larger amounts of detected dopamine paralleled greater modulation of LFP activity.

5.5.3.4 Concurrent recordings of dopamine overflow and striatal spike activity

The majority of neurons in the striatum have been described as medium spiny projection cells (90-95%) with spike activity characterized by long-duration action potentials, firing rates less than 5 Hz, and non-bursting activity in the anesthetized state [Gerfen96]. Neuronal activity with these characteristics was readily apparent during recordings with the multi-modal arrays, though the observed proportion of cells of this type was slightly lower (81%, 55 of 68 cells). On occasion, the arrays also recorded other neurons with faster firing rates and bursting activity (19%, 13 of 68 cells).

When firing activity was modulated following MFB stimulation, most responses were excitatory. While the initial increase in firing rate may have resulted from antidromic stimulation [Nieuwenhuys82], the prolonged responses were likely due to a different mechanism. Fig. 5.17A shows an example of two different types of responses recorded simultaneously on the same microelectrode array. The unit in the top row exhibited base-

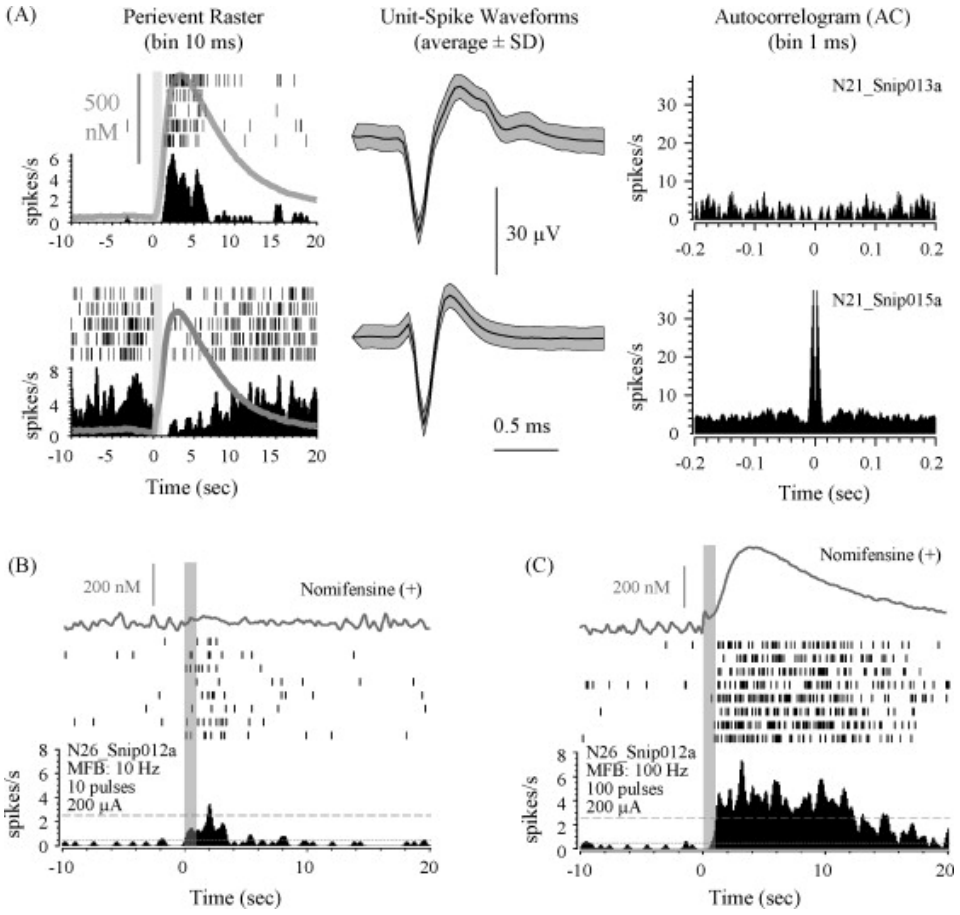

Figure 5.17: Responses to MFB stimulation. MFB stimulation evoked distinct changes in striatal spike activity as shown in representative examples of neurons recorded simultaneously along an implanted array. (A) This neuron responded with an excitatory response (top row) that paralleled the duration of elevated dopamine overflow. Other neurons (bottom row) exhibited an inhibitory response, which also paralleled dopamine overflow. This particular neuron exhibited a higher incidence of bursting than the neuron shown in the top row as indicated by the autocorrelograms. Recording modalities were separated by 200 μm. MFB stimulation consisted of a 100 pulse, 100 Hz train of 2 ms duration biphasic waveforms at 150 μA amplitude. (B and C) An example of neuronal firing rates and dopamine overflow depending on stimulation frequency for a striatal neuron excited during MFB stimulation. Both dopamine overflow and neuronal firing rates were smaller in magnitude and shorter in duration during randomized trials at (B) 10 Hz than at (C) 100 Hz. Recordings reflect the presence of nomifensine (10 mg/kg). Dashed lines represent 95% confidence intervals. Stimulation artifacts prevented including spikes during the 100 Hz stimulation train in the analysis.

line firing characteristics of a medium spiny cell and an increase in firing rate (0.2-4 Hz for approximately 6 s) following MFB stimulation. In this case, an adjacent microelectrode site recorded an electrochemical dopamine transient with an average peak response of 700 nM with elevated levels lasting for 8.8 s. Other cells exhibited prolonged inhibitory responses following MFB stimulation (Fig. 5.17A, bottom row). For this cell, the decreased firing rate also paralleled an increase in dopamine overflow that was significantly above baseline for 9.6 s.

The same neurons that were modulated at high intensity MFB stimulation also exhibited a dose-dependent relationship to electrical stimulation frequency (Fig. 5.17B and C). For an example cell with an excitatory response to MFB stimulation, 10 Hz pulse trains did not substantially modulate its firing rate above a 95% confidence interval (dashed line), but 100 Hz stimulation did lead to significant excitation lasting for 12 s. In parallel with these recordings, a negligible electrochemical dopamine signal was detected at 10 Hz stimulation, whereas significantly elevated dopamine levels were apparent following 100 Hz stimulation with durations similar to those observed in the firing rate analysis.

5.5.4 Discussion

We developed a microfabricated microelectrode array for simultaneous recording of electrophysiological and endogenous extra-synaptic dopamine signals. Recordings from these arrays in the striatum of urethane-anesthetized rats revealed spatial heterogeneity of electrically evoked dopamine and spatiotemporal parallels between recording modalities. While there are reports describing microdialysis measurements with LFP recordings made from electrodes implanted outside [Fried99, Ludvig92] or inside the

microdialysis tubing [Darbin06, Obrenovitch93], to our knowledge measuring neurotransmitter levels and LFPs at the same spatiotemporal scale through microfabricated arrays is a novel approach. In this parallel scheme, a constant bias potential sufficient to oxidize dopamine was applied independently at multiple platinum sites across the array with currents sampled every 16 ms. This fixed potential permitted the recording of wide-band electrophysiological activity simultaneously on adjacent iridium sites with no residual electrical artifact. The multi-modal concept was integrated into an array of microelectrodes fabricated on a thin silicon-substrate probe (15 μm × 80 μm cross-section) [Drake88].

A critical, and often overlooked, consideration with in vivo electrochemical techniques is the possibility that the applied potentials may influence neuronal activity [Stamford86]. Given the experimental challenges of concurrently recording both signal modalities, only a few studies have examined such effects and only in terms of modulations of spike rates [Armstrong84, Crespi95, Hefti83]. For example, the studies examining concurrent differential pulse or cyclic voltammetry have suggested that no concomitant changes in firing activity occur [Crespi95, Stamford93]. Another study observed neuronal inhibition (50% of the cells) for chronoamperometric pulses (1 s duration) at potentials between +0.6 and +1.0 V [Hefti83]. Since modulation was not evident at lower voltages in the Hefti and Felix study, the initially high non-faradaic currents (0.5-2 μA) at the larger applied potentials may have been responsible for the effects. We show in this study that applying constant potential amperometry to several 450 μm^2 microelectrodes in the striatum, which resulted in picoampere baseline currents, did not significantly modulate striatal activity within 200 μm of the sensors. Whether these findings are consistent in awake-

behavioral states or in other brain regions requires further examination. However, we believe the microfabricated arrays presented in this study offer a robust approach for further examination of the spatial distribution of influence, if any, that electrochemical waveforms may have on neuronal activity [Johnson05].

The multi-channel recordings showed significant spatial distribution of electrochemical dopamine transients following MFB stimulation with differences evident for microelectrode sites spaced as close as 200 μm apart. This is in agreement with previous studies examining dopaminergic stores ex vivo [Fallon78, Glowinski66] and overflow dynamics in vivo with a single carbon fiber along consecutive insertion depths [Bergstrom99, Garris94, May89] or at a single implant depth with a cluster of four carbon fibers [Dressman02]. These reports suggested that electrically evoked dopamine concentrations could vary over distances less than 100 μm within the striatum given the constraints imposed by diffusion, metabolism, and dopamine transporters [Cragg04, Peters00]. The increase and decrease of the dopamine signal recorded through the platinum microelectrode sites was of a longer duration than those reported in a previous study using a thin cylindrical carbon fiber microelectrode [Venton03], which suggests that a diffusion distance may have been present between the platinum microelectrode surface and release terminals. Narrowing the substrate width or placing the microelectrode sites on the lateral edges of the probe may facilitate closer proximity of the sensors to distal release sites.

The multi-channel measurements also provided evidence that the previously observed dopamine overflow heterogeneity was not simply a manifestation of tissue trauma induced during incremental insertions of a single microsensor [Westerink88]. It

should be emphasized that comparing dopamine responses with multiple microelectrodes requires detailed calibration in terms of sensitivity, response time, and selectivity. Though these metrics will inevitably vary slightly for any microelectrode [Kawagoe93], microfabrication processes are designed to limit this variance with reproducible microelectrode geometries and configurations with sub-micron precision [Burmeister01, Drake88, Najafi90].

While there is no one technique to identify an in vivo amperometric current as deriving exclusively from dopamine, there are ways to increase the confidence in the measurements [Phillips03]. Selectivity considerations are particularly important since electroactive metabolites are often present in higher extracellular concentrations than their neurotransmitter predecessors [Marsden84]. Arrays can include a number of components to improve selectivity. For example, layering of selective diffusion barriers, such as Nafion, over a microelectrode site can limit confounding analyte adsorption or shift its oxidation potential [Gerhardt84]. Patterns of identical microelectrode geometries on the same neural probe also provide an opportunity for differential recording methods in which a ‘reference’ site is pre-located in a region devoid of dopaminergic innervation such as in the corpus callosum. An analogous self-referencing approach had been proposed previously to increase signal-to-noise ratios for biosensor recordings [Burmeister01].

Identification of dopamine overflow can also benefit from certain experimental procedures, including stimulation of dopaminergic projection neurons (somatic or axonal) that directly innervate the targeted recording region [Garris97, Yeomans88]. Additionally, dopamine uptake inhibitors such as nomifensine can be used as selectivity indicators such that the electrically evoked responses after injection show larger peak amplitudes with

extended durations [Wightman88]. Delivery of such pharmacological agents would benefit from the integration of microfluidic channels within the microfabricated array [Johnson03, Rathnasingham04]. Finally, performing a more selective electrochemical approach such as differential pulse or fast-scan cyclic voltammetry with lower capacitance microelectrode materials, such as glassy carbon or diamond, prior to the multi-modal recordings would provide additional validation of the measurements [Kawagoe94].

The parallel recording approach facilitated simultaneous acquisition of electrophysiological signals with no residual electrical artifact. Striatal oscillations are typically smaller than those observed in more laminate brain regions including cortex [Buzsaki04b, Mitzdorf85] and hippocampus [Buzsaki02, Buzsaki92]. Nevertheless, studies have shown substantial modulation of striatal local field potentials during the sleep-wake transition [Gervasoni04], through behavioral tasks [Berke04], and in abnormal conditions [Boraud05, Costa06]. We observed modulation of oscillation frequencies following MFB stimulation, particularly in the low (<20 Hz) and occasionally in the gamma (40-90 Hz) bands. These modulations often paralleled the temporal response of dopamine overflow, which may reflect the emergence of synchronized activity within local striatal populations. Indeed, dopamine is thought to have a significant modulatory effect on corticostriatal processing at multiple spatiotemporal scales [Schultz07], which in the depleted state can lead to significant impairment of sensorimotor and motivational circuits as in evident in Parkinson's disease and dopa-responsive forms of dystonia. The multi-modal recording approach demonstrated in this study may thus be useful for investigating the role of neurotransmitters on abnormal oscillation dynamics in neurological disorders [Brown03, Lee03, McNamara94].

Future designs incorporating stereotrode and tetrode configurations on the silicon probe should help improve unit isolation, which is important for recording cells with low firing rates or from regions of high neuronal density [Blanche05]. Moreover, clusters of closely spaced microelectrodes will be important for studies that seek to robustly correlate spike activity with neurochemical dynamics. Lithographic processes facilitate designing implantable microelectrode arrays with customized recording site placement and substrate shape, high reproducibility of geometrical and electrical characteristics, and smaller cross-section profiles limiting the extent of gross tissue damage that insertion of multiple microwires may cause [Burmeister00, Hetke02, Wise04].

Chapter 6

Towards a Complete Chemical Recording System

6.1 Introduction

As System-on-a-Chip (SoC) applications continue to develop at a rapid pace, analog designers are required to design sensor interfaces for increasingly aggressive CMOS processes [Stork06, Gielen06]. While reducing device dimensions to the nanometer regime brings several key performance benefits to digital designs, analog designs are generally unable to take advantage of the same benefits, and the job of analog designers becomes increasingly difficult as CMOS technology moves rapidly into the nanoscale regime (sub-100 nm). The low power supply voltage available in these advanced processes reduces the headroom necessary for proper operation of many traditional circuits such as cascodes. This reduction in power supply levels combined with increased instability of process parameters makes high performance analog design at 65 nm and beyond a challenging and complex proposition [Gielen05, Lewyn09]. Additionally, several second order effects such as hot carriers are significantly increased and reduce the long term reliability of analog designs in short channel processes. Despite the challenges, successful SoC designs have been developed in these processes [Intel09].

For the past decade, students in Dr. Brown's research groups at both the University of Michigan and the University of Utah have developed and improved a SoC platform for wireless sensor nodes. In conjunction with the NSF sponsored WIMS ERC at the University of Michigan, this platform has become the WIMS Microcontroller. Thus far, two generations of WIMS Microcontroller have been designed and tested. The third generation WIMS microcontroller is currently under development, and is targeted at neural prosthetic and speech decode applications. The proposed system will be fully implantable and will be capable of recording both biopotential and biochemical signals, and then decoding those signals through software and dedicated DSP hardware. The decoded signals will then be transmitted through the skin via a radio or infrared transmitter [Kellis09]. A proposed top level architecture for the biochemical recording subsystem is shown in Fig. 6.1.

This chapter describes the design and testing of a potentiostat cell designed for use in this proposed third generation system. With the recent push towards a neural recording test bed, the platform was retargeted from the TSMC 180 nm CMOS process to the IBM

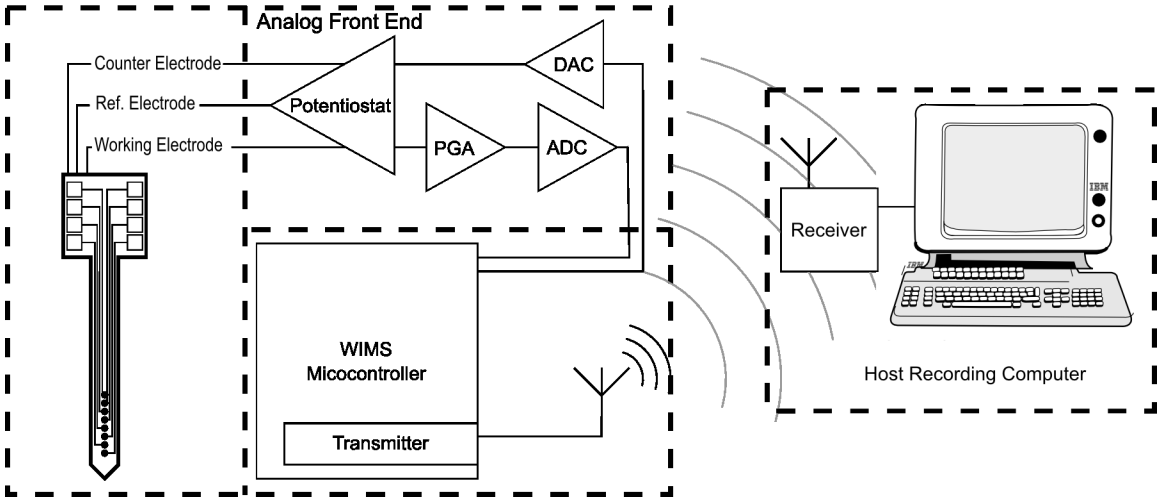

Figure 6.1: Proposed wireless neurochemical sensing system. The block diagram above shows the proposed wireless neurochemical sensing system including the WIMS Gen3 Microcontroller, UWB Radio, and Analog Front End

65 nm process. The decision to work in 65 nm was based on several key factors including increased digital performance, reduced power consumption, and reduced die area. These improvements will be key to several of the DSP and RF components of the system. However, working in a 65 nm process presents several challenges to analog circuit design. Of key importance is the 1 V power supply which restricts the sensing voltage of a single ended potentiostat to a swing of ±500 mV which in turn affects the range of detectable chemicals [Martin09].

Work is underway to port the WIMS microcontroller pipeline and many of the peripherals of the previous generation systems to the new technology. Additionally, several new components such as an I2C interface and the analog front end are being designed or redesigned from the ground up. One of these components is the potentiostat which is targeted at the neurotransmitters dopamine and serotonin (5-HT). These two examples as well as several other analytes of interest are electroactive at relatively low voltages (< +0.5 V) and are therefore good candidates for detection with a low voltage potentiostat which has a limited output voltage range.

6.2 Amperometric sensor circuits

Amperometric sensors consist of three electrodes forming an electrochemical cell—the working electrode, the reference electrode, and the counter electrode. The choice of material for both the working electrode and the reference electrodes is important in determining the electrochemical properties of the cell. The working electrode for neurochemical cells is commonly made from Pt or C and may be coated with a number of different membrane materials to increase selectivity to an analyte of interest [Johnson08,

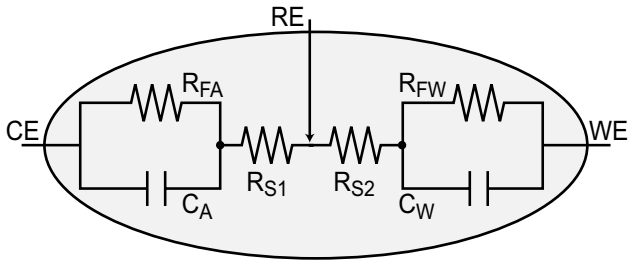

Figure 6.2: Equivalent circuit for an amperometric sensor. R_{FA} and R_{FW} represent faradaic resistances, and C_A and C_W are the double-layer capacitances associated with the counter electrode (CE) and the working electrode respectively. R_{S1} and R_{S2} are the resistances of the solution.

Yavich00]. The reference electrode should be one which forms a well defined Nernstian potential in the supporting electrolyte (in this case the brain). As discussed in Chapter 4 Ag/AgCl microwires and microfabricated disc electrodes are commonly used [Johnson08, Yavich00], and our recent work has identified IrO_x as a more biocompatible alternative to Ag/AgCl for in vivo work [Franklin09]. The choice of material for the counter electrode is less important but Pt is commonly used.

The electrochemical cell formed by these three electrodes can be modeled as shown in Fig. 6.2. At low frequencies, this model can be simplified by removing the two double layer capacitors C_A and C_W. Additionally R_{s1} and R_{s2} are normally small in strong electrolytes such as cerebral spinal fluid (CSF) and can be neglected for a first order analysis of the behavior of the system. Amperometric sensors work by manipulating the voltages shown in Fig. 6.3. The desired measurand for the sensor is the value of i_f for a particular v_w. The relationship of these two values is proportional to the analyte concentration at the surface of the electrode according to Eq. 2.5, and for a calibrated system the value of i_f can be used to determine the absolute concentration of the analyte in the system. However, as can be seen in Fig. 6.3 the applied voltage, V_a, has several components: v_w,

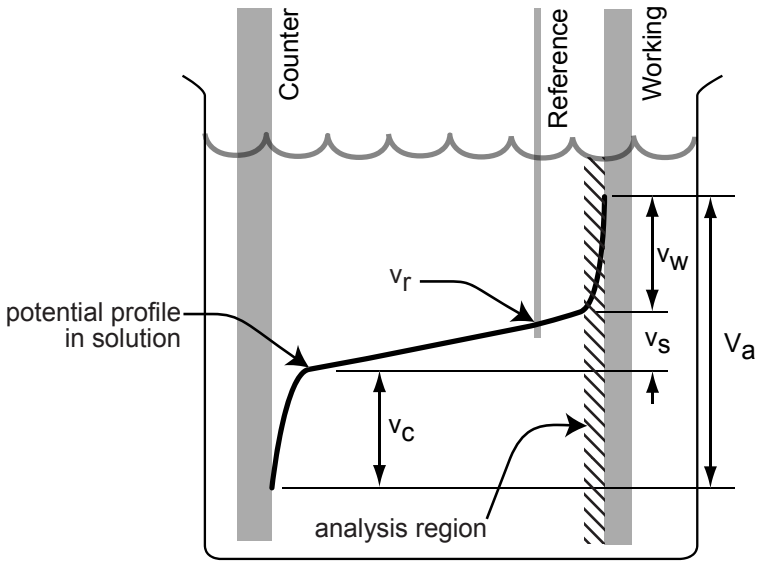

Figure 6.3: Potential drops. Three electrode system with all potential drops labelled. Previously presented as Fig. 2.8 and reprinted here for convenience.

v_s, and v_c, and each of these components can vary independently of the other components with regards to V_a. This variability makes determining v_w for a given V_a with only a counter electrode and a working electrode almost impossible. As a result, instrumentation is used to isolate v_w by adding a reference electrode and using feedback to control the voltage between the reference electrode and working electrode (V_{cell}), but only allowing current to flow between the counter electrode and the working electrode. Several voltage input waveforms can be used for detection in this configuration (see Section 2.7 on page 16), but all of them require a potentiostat circuit which can set the V_{cell} to an applied voltage, V_{src}, while applying the proper voltage on the counter electrode to support the faradaic current flow. In this case all of the current flows between the counter electrode and the working electrode, and ideally, zero current flows through the reference electrode.

6.3 Potentiostat circuit

6.3.1 Principle of operation

A basic potentiostat circuit is shown in Fig. 6.4. The basic principle of operation is to set $V_{cell} = V_{src}$ and measure i_{WE} (equivalent to i_f). Examining the circuit more closely reveals that OP_1 is configured as a voltage follower to buffer V_{RE}, OP_2 is configured for negative feedback through a path which includes the counter electrode, the reference electrode, and OP_1, and OP_3 is configured as an I-V converter for converting i_f to V_{out}. When V_{src} is applied to the circuit, current flows through the two R_1's so that *node a* is pulled to ground and the output of OP_1 is pulled to $-V_{src}$. Since OP_1 is a voltage follower, V_{RE} should also be $-V_{src}$ and the negative feedback path will cause OP_2 to adjust its output voltage (V_{CE}) so that enough current flows through the cell to let V_{RE} equal $-V_{src}$ and therefore $V_{cell} = V_{src}$. Assuming that all of i_f flows through R_f and since OP_3 will try to drive its negative terminal to ground to match the positive terminal, V_{out} will be equal to $-(V_f \cdot R_f)$. In order to achieve high accuracy with this circuit, all of the opamps need to have high gain and OP_3 should have very low input referred noise. For a more detailed analysis of this circuit especially noise sources, please refer to [Martin05].

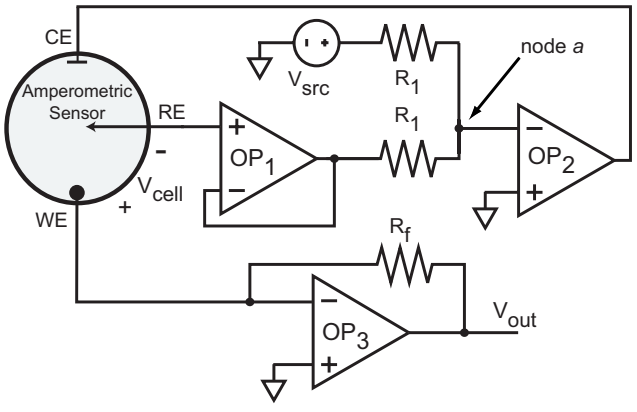

Figure 6.4: Potentiostat circuit.

6.3.2 Opamp design

The opamp design chosen for the potentiostat was based on a 180 nm design used in previous versions of the WIMS microcontroller analog front end. However, due to the reduced power supply voltage and smaller gate lengths, all of the transistors were resized to accommodate the new technology. The opamp was designed to have high gain for greater accuracy and low noise at the cost of increased current and area. The opamp is a folded cascode design with a dual n- and p-MOS input stage and a class AB output stage [Baker05]. The dual input stage was used to allow input voltages close to the rail for the maximum voltage swing when used as a unity gain buffer as in OP_1. Traditionally these input stages are used with constant g_m feedback to reduce distortion due to mismatches in g_m across the input voltage range and especially near the rails (the g_m varies by a factor of two across the input range). However, constant-g_m circuits introduce problems themselves due to additional feedback paths and mismatched transistors, and the introduced distortions can sometimes be worse than the distortion without the constant-g_m circuitry. Several constant-g_m circuits were evaluated for the design, but in the end the constant-g_m circuitry was left out of the design.

Throughout the layout (see Fig. 6.6), great care was taken to eliminate errors due to mismatches and process variations. All matched components in the design were kept as symmetrical as possible, and transistors were laid out in a one dimensional common centroid pattern. The four input transistors of the amplifier were laid out with a full two dimensional common centroid design.

After fabrication, the devices were tested to compare simulated performance with actual performance. Plots in Fig. 6.7 show samples of the opamp's output at 1 kHz and

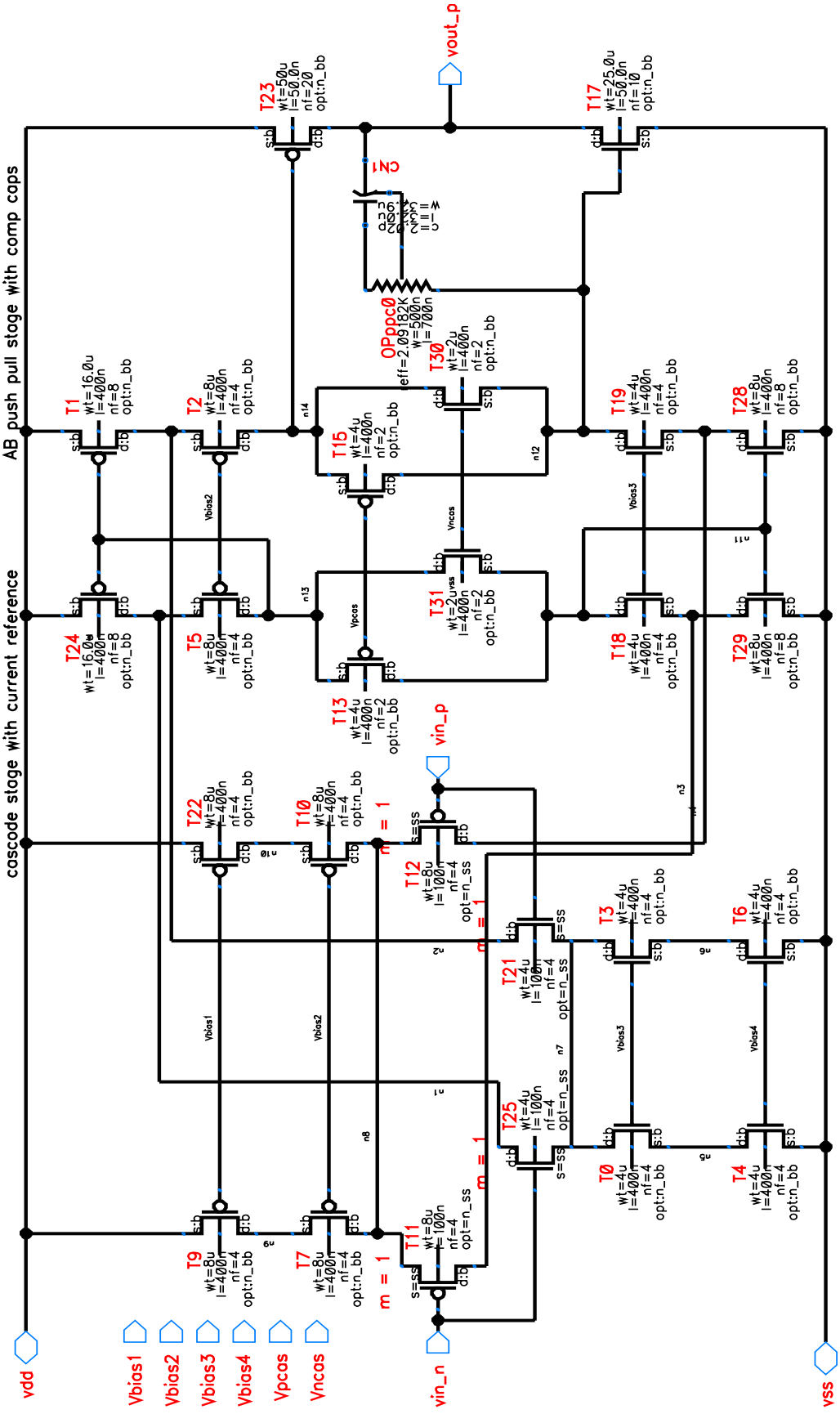

Figure 6.5: Folded cascode opamp design. All transistor sizes are as shown.

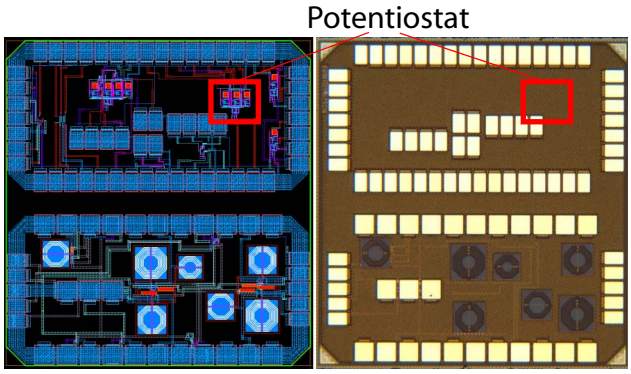

Figure 6.6: Layout and micrograph of test chip. Layout (left) and a micrograph (right) of the fabricated analog front end. The layout contains three test opamps (two single ended and a fully differential one), a single ended potentiostat (highlighted), and several test structures for process compensation. The potentiostat circuit occupies 0.015 mm^2.

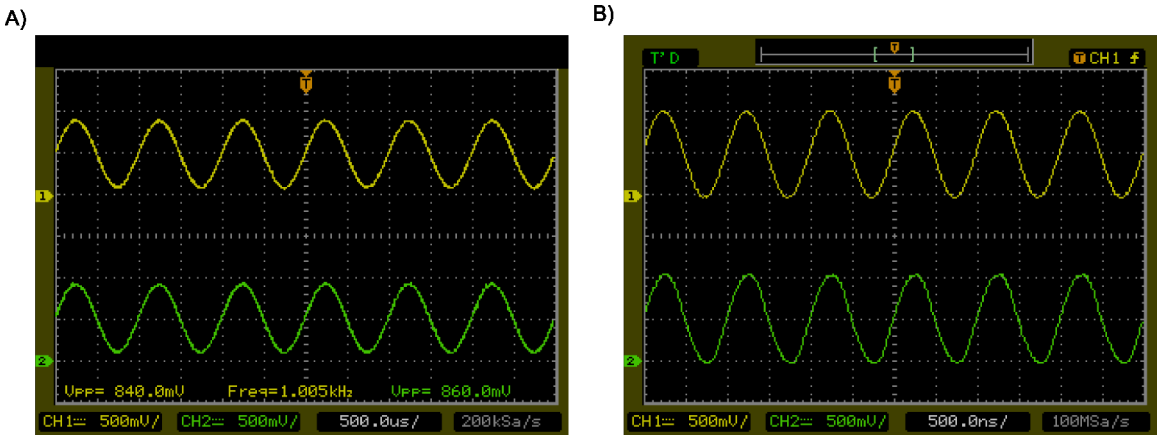

Figure 6.7: Screen captures of opamp in unity gain configuration. The screen captures show the input of the opamp (green) and the output of the opamp (yellow) at 1 kHz (a) and 1 MHz. Very little distortion is present in the signal and the measured gain is 0.997 V/V.

1 MHz. The opamp is configured as a unity gain buffer and the measured gain across 500 kHz of bandwidth is 0.997 V/V. A plot of the gain and phase across the entire bandwidth of the device can be seen in Fig. 6.8. The simulated bandwidth was 31.8 MHz while the measured bandwidth is only 2.44 MHz. This variation is most likely due to process variations causing a change in the g_m of the input transistors and an increase in the parasitic capacitance. The variation may also be due in part to the measurement technique.

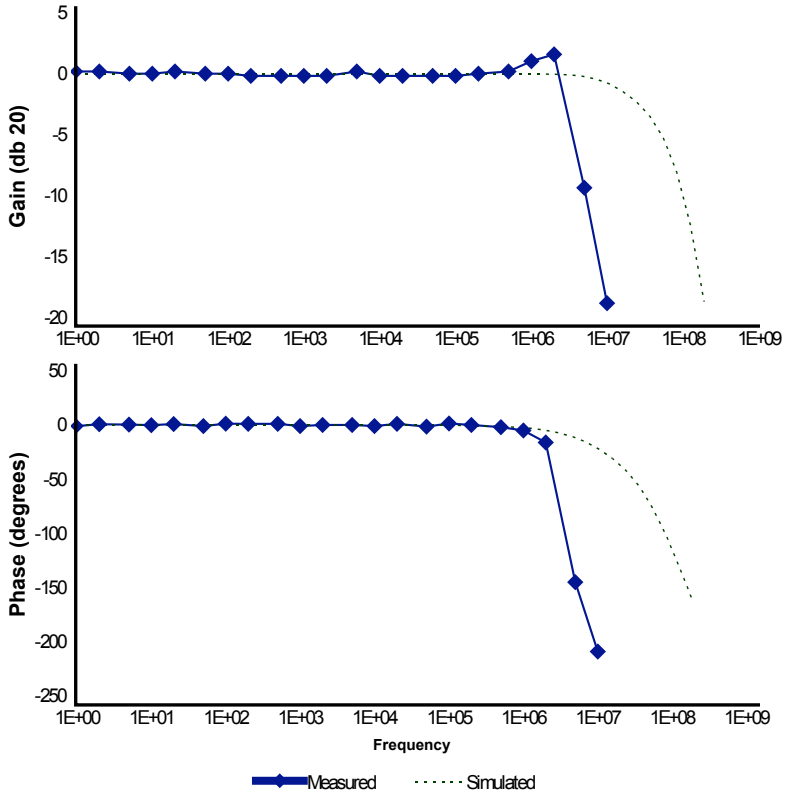

Figure 6.8: Opamp gain and phase response. The simulated and measured frequency responses of the opamp are plotted for the unity gain configuration. The bandwidth of the amplifier is 2.44 MHz which is smaller than the simulated bandwidth of 31.8 MHz.

Table 6.1: Measured values for opamp

Parameter	Simulated Value	Measured Value	Unit
Power Supply	1	1	V
I_{supply} (without bias circuit)	283	423	μA
Unity Gain Bandwidth	31.8	2.44	MHz
RMS Noise	N/A	< 1	μV RMS
Input referred noise @ 1kHz	N/A	10	nV/Hz
Offset voltage	0	<1	mV
Open Loop Gain	1278	950	V/V

Measurements of additional opamp characteristics are shown in Table 6.1. The measurements were taken using a Keithly 2062 Sourcemeter, an Agilent 33120A waveform generator, an SRS SR780 signal analyzer, and several custom LabView VIs written to automate testing. Most of the measured parameters were different from the simulated parameters, but all were within the desired parameters for the design. The amplifier was tested in a number of configurations and found to be fully functional for the purposes of its use in a potentiostat.

The largest discrepancy was the power consumption of the final device. Simulations indicated a power consumption of 283 μW, but the measured current was almost 2x bigger at 423 μW. Measurements of the beta multiplier voltage reference (see Liu98) showed that the reference current of the bias generator was also almost double the simulated bias current. The beta multiplier architecture was chosen due to its lack of substrate charge injection, a feature of the more common bandgap reference design. Minimizing substrate charge injection in this design was important for compatibility with the body biasing compensation techniques currently under development by our group and for reducing second order effects such as hot carriers [Ghosh08, Ghosh10].

A plot showing the simulated and measured results for the bias circuitry can be seen in Fig. 6.9. At a 1 V power supply, the expected bias current was 31 μA but the measured current was almost double that value at 54 μA. Despite this increase in current, feedback in the bias circuit maintains the voltage output at the desired level, and as can be seen in the plot, the measured output voltage tracks the simulated results almost perfectly. The large increase in bias current is most likely due to process variations in the g_m and V_T of the bias transistors from the expected normal values and increased gate leakage due to the

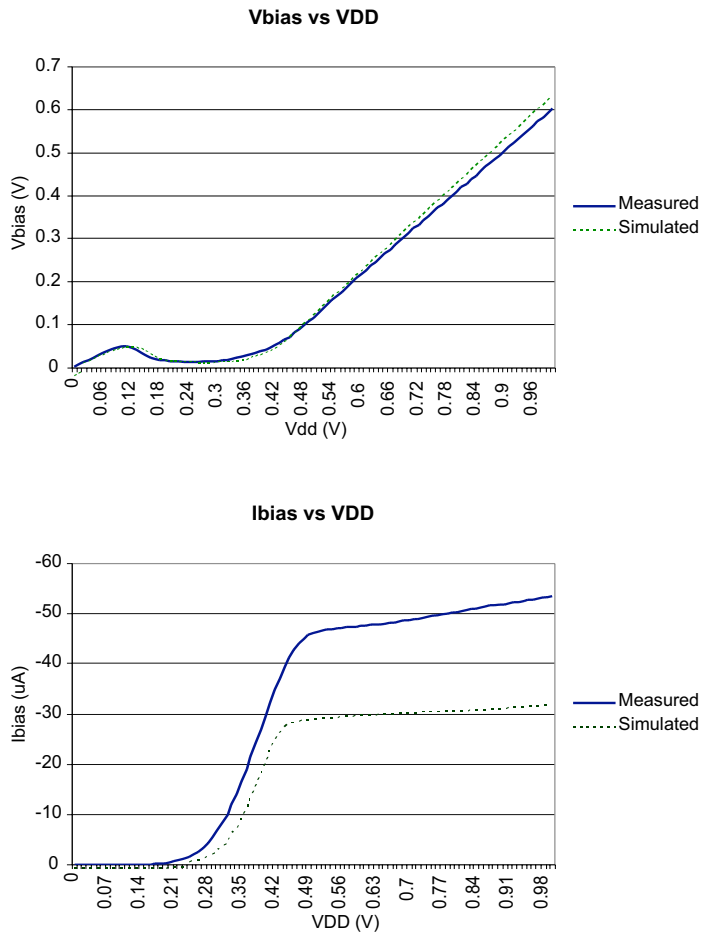

Figure 6.9: Measured bias generator output. The simulated and measured responses of the bias generator are plotted. The output voltage of the bias generator tracks simulated results almost perfectly, but the bias current is much higher than expected. Note that the plotted bias voltage is the positive output of the bias generator and is intended to be approximately 0.35 V below VDD which explains why it tracks VDD instead of flattening out like the bias current does.

very thin gate oxides used in the 65 nm process. As a side note, a test version of the Gen3 WIMS microcontroller was also fabricated in the same fabrication run as this test chip, and the measured power draw of that chip was also significantly higher than the simulated power. However, regardless of the cause for the increase in power, adding an external resistor to the bias circuit allowed for tuning of the circuit to match the simulated values better, and in a production run of this device, the accuracy would be greatly improved by using trimmed on-chip components.

6.3.3 Potentiostat circuit

The Opamp was incorporated as part of the potentiostat circuit shown in Fig. 6.4 with R_1 and R_f set to 10 kΩ. The circuit draws 2.2 mA of current at a 1 V supply and is operational with a 1.2 V to 850 mV supply voltage. The performance of the entire circuit was measured and found to perform as designed. To measure the input range of the potentiostat, a 13.3 kΩ resistor was placed between the RE and the WE terminals of the potentiostat, and the CE and RE terminals were shorted. A voltage ramp was then applied across the V_{src} terminals of the potentiostat using a Keithly 2602 Sourcemeter and the output voltage was measured using the same instrument. The output voltage was converted to a current by dividing the V_{out} by R_f(10 kΩ). The results in Fig. 6.10 show that the output of the potentiostat is linear between 29 μA and 82 μA (0.29 V-0.82 V), and using the Keithly Sourcemeter, current changes as small as 1 nA were measurable. A wider dynamic range for the potentiostat could be achieved by using a programmable gain amplifier for the I-V conversion of OP_3 as the current dynamic range is limited to the available output voltage swing which is in turn limited by the reduced supply voltage.

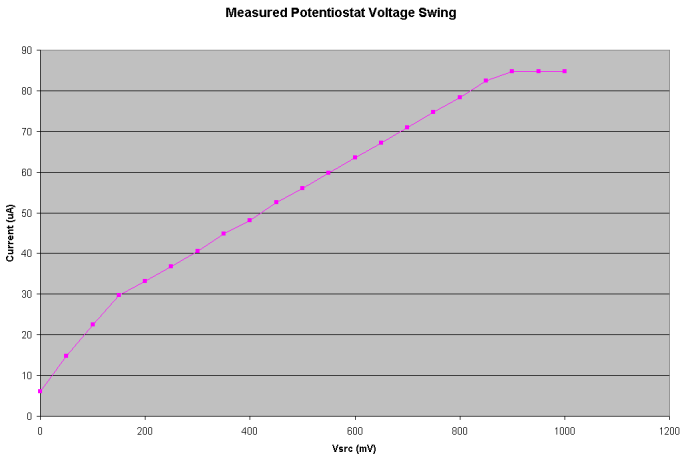

Figure 6.10: Output characteristics of the potentiostat. Measured current for a 1V voltage ramp using a 13.3kΩ resistor between RE and WE.

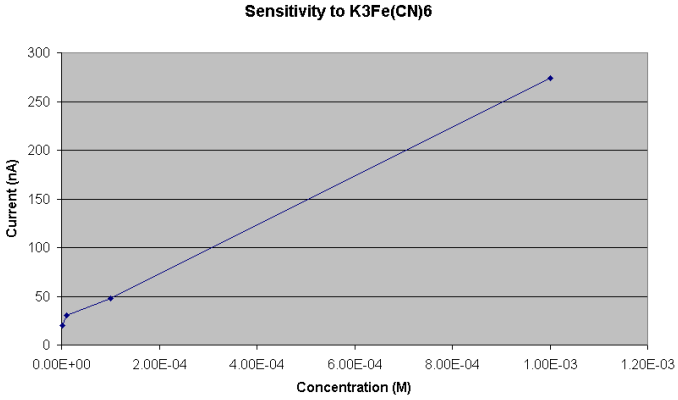

Figure 6.11: Measured sensitivity of potentiostat to $K_3Fe(CN)_6$. The output of the potentiostat was found to be linear for 1 μM to 1 mM concentrations of $K_3Fe(CN)_6$.

To test the functionality of the potentiostat, chronoamperometric measurements were made in 0.1X PBS using a 0.25 cm^2 platinum disk electrode (Bioanalytical Systems, Inc.) for the working electrode, a commercial Ag/AgCl reference electrode (Orion) for the reference electrode, and a Pt wire for the counter electrode. Aliquots of $K_3Fe(CN)_6$ were added to the PBS solution to bring the total concentration of the solution to a desired concentration (1 μM, 10 μM, 100 μM, 1 mM) and the solution was allowed to equilibrate for five minutes. After five minutes 0.5 V was applied to the V_{src} terminal and the output voltage was measured 8 s after applying the voltage. A background scan was also done in 0.1x PBS and the background current was subtracted from the measured results to determine an absolute value of the change in faradaic current due to each concentration. The results of the testing are shown in Fig. 6.11 and they indicate that the potentiostat is capable of detecting analyte concentrations as low as 1 μM. A comparison of power vs. area for the 65 nm potentiostat reported here and several other reported potentiostats is shown in Fig. 6.12. The potentiostat reported here is the smallest potentiostat reported, however it's power (1.3 mW) is significantly larger than the smallest reported power number of

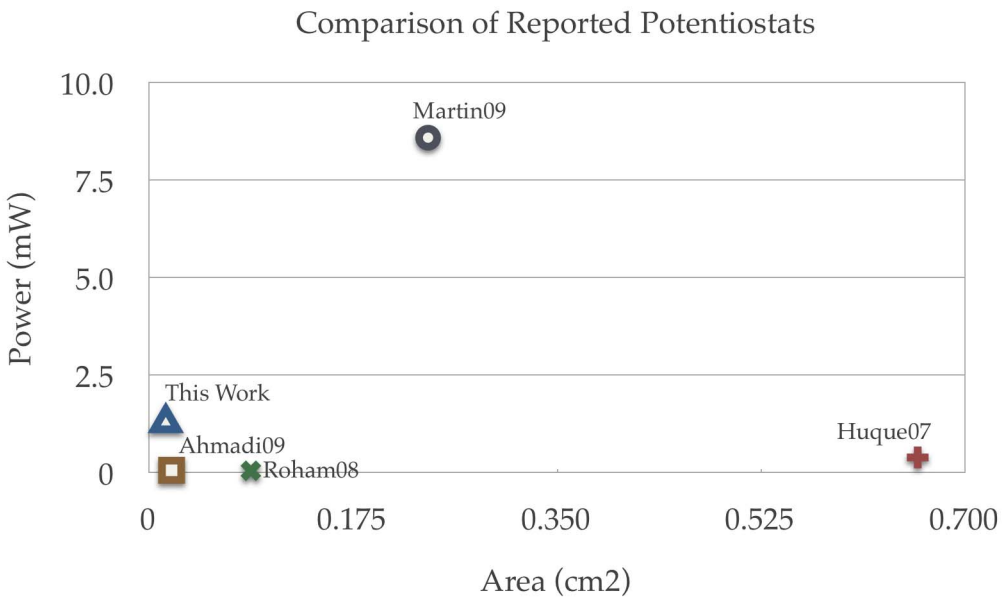

Figure 6.12: Comparison of reported potentiostats. The power and area for several recently reported potentiostats are reported.

0.57 mW [Roham08]. However, the present design was not optimized for power consumption and further optimizations should allow for a power consumption of 0.5 to 0.25 mW.

6.4 Discussion

The design and testing of a 65 nm potentiostat has been described. The individual components of the potentiostat were tested and found to function within specified parameters, with the exception of power which is twice the expected value. The completed potentiostat has been tested and used to measure $K_3Fe(CN)_6$. This design will form an important building block in the analog front end of the WIMS Gen3 microcontroller.

Additional characterization of the potentiostatiostat is ongoing. Additional data, including sensitivity to dopamine, ascorbic acid, and other neurotransmitters, will be collected. Finally, cyclic voltammetry scans using the potentiostat have not yet been recorded and will need to be recorded to fully characterize the system. The biggest hurdle in this

testing is the development of LabView VIs and instrumentation necessary to perform the experiments.

Chapter 7

Conclusion

In the introduction to this dissertation, two specific aims were outlined: (1) To fabricate and characterize multi-modal neural probes for sensing electroactive neurochemicals, and (2) to design and fabricate readout circuitry for the probes implementing functions necessary for multi-modal recordings. This chapter will examine how well those goals were met and summarize some of the more significant contributions of this work to advancing the state of the art.

7.1 Summary of contributions

7.1.1 Iridium oxide reference electrodes

Reference electrodes are key to any chemical sensing system. However, prior to the studies conducted in this work, no good solution for long term in vivo chemical sensing existed. Ag/AgCl, despite it's inherent bioincompatibility, is still widely used for in vivo work due to the unavailability of a good alternative reference electrode. The studies conducted in this work have shown the feasibility of IrO_x as an in vivo reference electrode for use in the brain. Beyond just demonstrating the viability of IrO_x reference electrodes, two different methods for fabricating the IrO_x films have been compared and

the fabrication methods for the better choice, Activated IrO_x Films (AIROF), have been optimized to produce the best results.

7.1.2 Development, fabrication, and testing of neural probes

At the outset of this work, neurochemical sensing on silicon microprobes was still in its infancy. This work has fabricated four different generations of probes and test structures. These devices were characterized extensively in vitro and were used to study a variety of analytes such as dopamine and choline and to develop new electrode materials. The testing culminated in a broad array of in vivo tests which demonstrated the feasibility of silicon neural probes for applications requiring simultaneous electrophysiological and neurochemical recordings.

7.1.3 65 nm potentiostat

To effectively use any new and potentially disruptive technology to maximum effect, new methods and tools are required. Although traditional methods exist for recording both chemical and electrophysiological signals, no good tool exists for doing both simultaneously, and the large bulky nature of the existing tools preclude their use in many chronic applications. Toward this end, analog circuits and amplifiers necessary for building a complete, miniature simultaneous recording system have been developed and tested as part of this work.

7.2 Future work

Despite the advances reported in this work, there are still many opportunities for advancement in this field. Two natural extensions of this work are further characterization of IrO_x electrodes in vivo and further development of a complete recording system. The IrO_x electrodes reported in this work were extensively characterized in vitro and they have

been used for short term pH studies in the brain, but they have not yet been fully characterized in vivo for long-term stability. More work needs to be done to determine the fidelity of recordings made using IrO_x reference electrodes over periods of days to weeks. The final piece which needs to be more fully implemented is a complete neurochemical recording system designed to allow chronic recording using wireless telemetry and large channel counts. Work is underway to develop such a system with the Gen3 WIMS microcontroller, and hopefully the completion of that system will allow integration of probes and electronics in new ways that will enable new types of experiments and allow researchers to more fully probe the complex reactions which make up the human nervous system.

Appendix A: IrO_x Comparison Run Sheet

This appendix contains the run sheet that was used for the IrO_x described in Section 4.3.1 on page 45.

Run # _____

Run General Description: Fabricate IrOx reference electrodes using both Sputter and Activated IrOx

Individual Purpose: _____ Results:_____

Done	Step	Name	Specification	Description	Quality Assurance	Comments
	4" Si wafers <100> p-type 1-3 ohm-cm					
	1	Pre-Furnace Clean	"*RCA Procedure*" •100:1 H_2O:HF, 30 sec •5:1:5 H_2O:NH_4OH:H_2O_2, 75 °C, 10 min •6:1:1 H_2O:HCL:H_2O_2, 75 °C, 10 min •Cascade Rinse until resistance peaks			This step skipped because starting with wafers with 1.2um of oxide already on them
	2	Lower Oxide	TCA Oxide •DWDTCA 5/200/5 min (dry/wet/dry) 1100 °C, 10 min setting time Target: 1.2um of SiO_2	The lower level oxide layer specifications are flexible		
	3	Lithography "Gold Mask"	•____ 5 min dehydration bake @ 120 °C •____ 1813 PR, 3k RPM for 30 sec •____ 70 s softbake @ 90 °C •____ EV Aligner, 10 sec exp,1 min MF352 develop •____ Oxygen Ash, 80 W, 1.5min, 250mT	Lift off enhanced by slightly over-developing, and using no post-bake step to prevent possible side-wall slumping. Target: 2.2um of PR	_____ Visually inspect	Date: Temp:
	4	Recess Etch	Buffered HF Etch (Target: 120nm of SiO_2 etched) •1.2 min etch in fresh BOE •4.0 min DI rinse	Recess the Au making it planar and enhancing lift-off.	_____ Visually inspect _____ Measured Depth on Profilometer	Date:
	5	Au Deposition	TMV Sputterer Target: 200 Å Ti Source #?? DC, 5mT, 45W, 3min Target: Au 4500Å Source #3 DC, 20mT, 90W, 9 min		Actual Ti/Au thickness: _____ using profilometer	Date: Run #:
	6	lift-off	Acetone lift-off Au •Soak 10 min •Ultrasonic 2min and repeat until pattern is defined •Rinse vigorously with Acetone, IPA, DI spraybottles	Perform lift-off with wafer upside down. Check carefully for redeposited material.	_____ Visually inspect	Date:

Run # _____

Done	Step	Name	Specification	Description	Quality Assurance	Comments
	7	Ash	Oxygen Ash, 150W, 5 min, 250 mT	Remove residual solvent films	_____ Visually inspect	Date:
	8	Lithography "Activated IrO_x Mask"	•____ 5 min dehydration bake @ 150 °C •____ Spin LOR-7B, 3k RPM for 50 sec. •____ 5 min bake @ 150 °C •____ Spin 1813, 3k RPM 50s •____ 3 min bake @95 °C in Oven •____ EV aligner 10 sec exp, •____ Develop for 1 min in 352 •____ Rinse 4 min in DI, spin dry		_____ Visually inspect pattern under scope after patterning	Date: Temp:
	9	Ti/Ir Deposition	TMV Sputterer Target: 200 Å Ti Source #?? DC, 5mT, 45W, 3min Target: 2000 Å Ir Source #?? DC, 5mT, 45W, 24min		Actual Ti/IrO_x thickness: _____ using profilometer	Date: Run #:
	10	Acetone Liftoff	Acetone lift-off Ti/Ir •Soak 10 min, ultrasonic 2min and repeat •Rinse with Acetone, IPA spraybottles, and DI		_____ Visually inspect	Date:
	11	Ash	Oxygen Ash, 150W, 5 min, 250 mT	Remove any residual solvent films	_____ Visually inspect	Date:
	12	Lithography "Sputtered IrO_x Mask"	•____ 5 min dehydration bake @ 150 °C •____ Spin LOR-7B, 3k RPM for 50 sec. •____ 5 min bake @ 150 °C •____ Spin 1813, 3k RPM 50s •____ 3 min bake @95 °C in Oven •____ EV aligner 10 sec exp, •____ Develop for 1 min in 352 •____ Rinse 4 min in DI, spin dry		_____ Visually inspect pattern under scope after patterning	Date: Temp:
	13	Ti/IrO_x Deposition	TMV Sputterer Target: 200 Å Ti Source #?? DC, 5mT, 45W, 3min Target: 2000 Å Ir Source #?? DC, 5mT, 45W, 24min, ?? sccm O2	Target 2200Å	Actual Ti/IrO_x thickness: _____ using profilometer	Date: Run #:

Run # _____

Done	Step	Name	Specification	Description	Quality Assurance	Comments
	14	Acetone Liftoff	Acetone lift-off Ti/IrO_x •Soak 10 min, ultrasonic 2min and repeat •Rinse with Acetone, IPA spraybottles, and DI		_____ Visually inspect	Date:
	15	Ash	Oxygen Ash, 150W, 5 min, 250 mT	Remove any residual solvent films	_____ Visually inspect	Date:
	16	Passiva-tion	Oxford PECVD Nitride (Sign up for 4 hr. time slot) Target: 2000 Å/8000 Å Nitride •SiO2:??? •SiN:???	Passivate sensors.	_____ Visually inspect _____ Measured Thick-ness using Monitor Wafer	Date: Run #:
	17	Lithogra-phy "Contact Mask"	•____ 5 min dehydration bake @ 120 °C •____ 1813 PR, 3k RPM for 30 sec. •____ 70s prebake @ 90 °C •____ EV aligner 10 sec exp, 1 min develop in 352 •____ Rinse 4 min in DI, spin dry •____ 70s hardbake @ 110 °C		_____ Visually inspect pattern under scope after patterning	Date: Temp:
	18	Contact Etch	Oxford Chamber #2 (Left) (2hr time slot) •____ O_2 descum, 5min O_2 50 sccm, 300 mT, 50 W •____ SiN etch, 12 min, wafer flats facing out O_2 1, CF_4 40 sccm, 100mT, 100 W •____ SiN etch, 12 min, wafer flats facing in	Remove the 1um of O2/SiN Voltage for SiN Etch: _____	_____ Probe openings with probe station.	Date: Run #:
	19	Ash	Asher, 150W, 5 min, 250 mT			Date:
	20	Resist Strip	PRS-2000, Heated for 15min, 4min DI rinse			Date:
	21	Passiva-tion	Spin 1813 •____ Spin 1813 for 30sec at 3 kRPM •____ Softbake on 105 °C hot plate for 1 min.			Date:

Run # _____

Comments:

_____

_____

_____

_____

_____

_____

_____

_____

_____

Bibliography

[Adams76] R.N. Adams, “Probing brain chemistry with electroanalytical techniques,” *Anal Chem*, vol. 48, pp. 1126-38, 1976.

[Agnati00] L.F. Agnati, K. Fuxe, C. Nicholson, and E. Syková, *Volume transmission revisited*. Amsterdam; New York: Elsevier, 2000.

[Ahmadi09] M. Ahmadi and G. Jullien, “Current-Mirror-Based Potentiostats for Three-Electrode Amperometric Electrochemical Sensors,” Circuits and Systems I: Regular Papers, IEEE Transactions on, vol. 56, pp. 1339-1348, 2009.

[Armstrong84] J.M. Armstrong and J. Millar, “High speed cyclic voltammetry and unit recording with carbon fibre microelectrodes,” in *Measurement of Neurotransmitter Release In Vivo*, C.A. Marsden, Ed. Chichester [West Sussex]/New York: Wiley, chapter 10, 1984.

[Armstrong83] M. Armstrong-James and K. Fox, “Effects of ionophoresed noradrenaline on the spontaneous activity of neurons in rat primary somatosensory cortex,” *J Physiol*, vol. 335, pp. 427-47, 1983.

[Bai00] Q. Bai, K. D. Wise, and D. J. Anderson, “A high-yield microassembly structure for three-dimensional microelectrode arrays,” *IEEE Trans Biomed Eng*, vol. 47, pp. 281-289, 2000.

[Baker05] R. Baker, H. Li, and D. Boyce, CMOS Circuit Design, Layout, and Simulation, Piscataway, NJ: IEEE Press, 2005.

[Bard00] Bard A and Faulkner L *Electrochemical Methods*. John Wiley & Sons, New York, NY, 2000.

[Bard01] A.J. Bard and M. Stratmann, *Encyclopedia of electrochemistry.* Weinheim: Wiley-VCH, 2001.

[Bartlett87] P.N. Bartlett and R.G. Whitaker, “Electrochemical Immobilization of Enzymes. 2. Glucose-Oxidase Immobilized in Poly-N-Methylpyrrole,” *J Electroanal Chem*, vol. 224, pp. 37-48, 1987.

[Bergstrom99] B.P Bergstrom and P.A. Garris, “Utility of a tripolar stimulating electrode for eliciting dopamine release in the rat striatum,” *J Neurosci Methods*, vol. 87, pp. 201-208, 1999.

[Berke04] J.D. Berke, M. Okatan, J. Skurski, and H.B. Eichenbaum, “Oscillatory entrainment of striatal neurons in freely moving rats,” *Neuron,* vol. 43, pp. 883-896, 2004.

[Bickford91] P. Bickford-Wimer, K. Pang, G.M. Rose, and G.A. Gerhardt, “Electrically-evoked release of norepinephrine in the rat cerebellum: an in vivo electrochemical and electrophysiological study,” *Brain Res*, vol. 558, pp. 305-11, 1991.

[Bjornsson06] C.S. Bjornsson, S.J. Oh, Y.A. Al-Kofahi, Y.J. Lim, K.L Smith, J.N. Turner, S. De, B. Roysam, W. Shain, S.J. Kim, “Effects of insertion conditions on tissue strain and vascular damage during neuroprosthetic device insertion,” *J Neural Eng*, vol. 3, pp. 196-207, 2006.

[Blanche05] T.J. Blanche, M.A. Spacek, J.F. Hetke, and N.V. Swindale, “Polytrodes: high-density silicon electrode arrays for large-scale multiunit recording,” *J Neurophysiol*, vol. 93, pp. 2987-3000, 2005.

[Boraud05] T. Boraud, P. Brown, J.A. Goldberg, A.M Graybiel, and P.J Magill, “Oscillations in the basal ganglia: the good, the bad, and the unexpected,” in *The Basal Ganglia*, Vol. 8, J.P. Bolam, C.A. Ingham, and P.J. Magill, Eds., New York: Springer, pp. 3-24, 2005.

[Boulton95] A.A. Boulton, G.B. Baker, and R.N. Adams, *Voltammetric methods in brain systems*. Totowa, N.J.: Humana Press, 1995.

[Bousse86] L.J. Bousse, P. Bergveld, H.J.M. Geeraedts, “Properties of Ag/AgCl electrodes fabricated with IC-compatible technologies”, *Sens Actuators B*, vol. 9, pp. 179-197, 1986

[Bragin02] A. Bragin, I. Mody, C.L. Wilson, and J. Engel Jr, “Local generation of fast ripples in epileptic brain,” *J Neurosci*, vol. 22, pp. 22:2012-21, 2002.

[Brown03] P. Brown, “Oscillatory nature of human basal ganglia activity: relationship to the pathophysiology of Parkinson’s disease,” *Mov Disord*, vol. 18, pp. 357-63, 2003.

[Burmeister00] J.J. Burmeister, K. Moxon, and G.A. Gerhardt, “Ceramic-based multisite microelectrodes for electrochemical recordings,” *Anal Chem*, vol. 72, pp. 187-92, 2000.

[Burmeister01] J.J. Burmeister and G.A. Gerhardt, “Self-referencing ceramic-based multisite microelectrodes for the detection and elimination of interferences from the measurement of L-glutamate and other analytes,” *Anal Chem*, vol. 73, pp. 1037-42, 2001.

[Burmeister02] J.J. Burmeister, F. Pomerleau, M. Palmer, B.K. Day, P. Huettl, and G.A. Gerhardt, “Improved ceramic-based multisite micro-electrode for rapid measurements of L-glutamate in the CNS,” *J Neurosci Methods*, vol. 119, pp. 163-171, 2002.

[Buzsaki92] G. Buzsaki, Z. Horvath, R. Urioste, J. Hetke, and K. Wise, “High-frequency network oscillation in the hippocampus,” *Science*, vol. 256, pp. 1025-7, 1992.

[Buzsaki02] G. Buzsaki, “Theta oscillations in the hippocampus,” *Neuron*, vol. 33, pp. 325-40, 2002.

[Buzsaki04a] G. Buzsaki, “Large-scale recording of neuronal ensembles,” *Nat Neurosci,* vol. 7, pp. 446-51, 2004.

[Buzsaki04b] G. Buzsaki and A. Draguhn, “Neuronal oscillations in cortical networks,” *Science*, vol. 304, pp. 1926-9, 2004.

[Chan09] H.-Y. Chan; D.M. Aslam, J.A. Wiler, B. Casey, “A Novel Diamond Microprobe for Neuro-Chemical and -Electrical Recording in Neural Prosthesis,” Microelectromechanical Systems, Journal of, vol.18, no.3, pp.511-521, June 2009

[Changeux93] J. Changeux, “Chemical Signaling in the Brain,” *Scientific American*, pp. 58-62, Nov. 1993.

[Cheer05] J.F. Cheer, M.L. Heien, P.A. Garris, R.M Carelli, and R.M Wightman, “Simultaneous dopamine and single-unit recordings reveal accumbens GABAergic responses: implications for intracranial self-stimulation,” *Proc Natl Acad Sci USA*, vol. 102, pp. 19150-5, 2005.

[Chen97] J. Chen, K.D. Wise, J.F. Hetke, and S.C. Bledsoe, Jr., “A multichannel neural probe for selective chemical delivery at the cellular level,” *IEEE Trans Biomed Eng*, vol. 44, pp. 760-9, 1997.

[Chung06] T.D. Chung, H.C. Kim, S.K. Kim, and H. Lim, “A miniaturized electrochemical system with a novel polyelectrolyte reference electrode and its application to thin layer electroanalysis,” *Sensors and Actuators B (Chemical)*, vol. 115, pp. 212-19, May. 2006.

[Cogan02] S.F. Cogan, “Stability of electroactive materials and coatings for charge-injection electrodes,” in *Proceedings of the IEEE Engineering in Medicine and Biology Society*, vol. 3, pp. 2062, 2002.

[Cogan04] S. Cogan, T. Plante, and J. Ehrlich, “Sputtered iridium oxide films (SIROFs) for low-impedance neural stimulation and recording electrodes,” in *Proceedings of the IEEE Engineering in Medicine and Biology Society*, pp. 4153-4156, 2004.

[Cogan05] S. Cogan, P. Troyk, J. Ehrlich, and T. Plante, “In vitro comparison of the charge-injection limits of activated iridium oxide (AIROF) and platinum-iridium microelectrodes,” *Biomedical Engineering, IEEE Transactions on*, vol. 52, pp. 1612-1614, 2005.

[Cogan07] S.F. Cogan, P.R. Troyk, J. Ehrlich, C.M. Gasbarro, and T.D. Plante, “The influence of electrolyte composition on the in vitro charge-injection limits of activated iridium oxide (AIROF) stimulation electrodes,” *J Neural Engineering*, vol. 4, pp. 79-86, 2007.

[Costa06] R.M. Costa, S.C. Lin, T.D. Sotnikova, M. Cyr, R.R. Gainetdinov, M.G Caron, M.A.L. Nicolelis, “Rapid alterations in corticostriatal ensemble coordination during acute dopamine-dependent motor dysfunction,” *Neuron*, vol. 52, pp. 359-69, 2006.

[Cragg04] S.J. Cragg and M.E. Rice, “Dancing past the DAT at a DA synapse,” *Trends Neurosci*, vol. 27, pp. 270-7, 2004.

[Crespi88] F. Crespi, K.F. Martin, and C.A. Marsden, “Measurement of extracellular basal levels of serotonin in vivo using nafion-coated carbon fibre electrodes combined with differential pulse voltammetry,” *Neuroscience*, vol. 27, pp. 885-96, 1988.

[Crespi95] F. Crespi, T. England, E. Ratti, and D.G. Trist, “Carbon fibre micro-electrodes for concomitant in vivo electrophysiological and voltammetric measurements: no reciprocal influences,” *Neurosci Lett*, vol. 188, pp. 33-6, 1995.

[Csicsvari03] J. Csicsvari, D.A. Henze, B. Jamieson, K.D. Harris, A. Sirota, P. Bartho, K.D. Wise, G. Buzsaki, “Massively parallel recording of unit and local field potentials with silicon-based electrodes,” *J Neurophysiol*, vol. 90, pp. 1314-23, 2003.

[Darbin06] O. Darbin, L. Newton, and T. Wichmann, “A new probe to monitor the effects of drugs on local field potentials,” *J Neurosci Methods*, vol. 155, pp. 291-5, 2006.

[Dendo94] I. Dendo, “Precision silver/silver chloride electrodes”, in *Proceedings of the IEEE Engineering in Medicine and Biology Society*, vol. 2, pp. 810-811, 1994.

[Drake88] K.L. Drake, K.D. Wise, J. Farraye, D.J. Anderson, and S.L. BeMent, “Performance of planar multisite microprobes in recording extracellular single-unit intracortical activity,” *IEEE Trans Biomed Eng*, vol. 35, pp. 719-32, 1988.

[Dressman02] S.F. Dressman, J.L. Peters, and A.C. Michael, “Carbon fiber microelectrodes with multiple sensing elements for in vivo voltammetry,” *J Neurosci Methods*, vol. 119, pp. 75-81, 2002.

[Ewing83] A.G. Ewing, J.C. Bigelow, and R.M. Wightman, “Direct in vivo monitoring of dopamine released from two striatal compartments in the rat,” *Science*, vol. 221, pp. 169-71, 1983.

[Fallon78] J.H. Fallon and R.V. Moore RY, “Catecholamine innervation of the basal forebrain. IV. Topography of the dopamine projection to the basal forebrain and neostriatum,” *J Comp Neurol,* vol. 180, pp. 545-80, 1978.

[Finlay00] J.M. Finaly and M.J. Zigmond, “A critical analysis of neurochemical methods for monitoring transmitter dynamics in the brain,” in *Psychopharmacology: The Fourth Generation of Progress*, F.E. Bloom and D.J. Kupfer (eds.), New York: Raven Press, pp. 29-39, 2000.

[Franklin05] R. Franklin, M. Johnson, K. Scottt, J.H. Shim, H. Nam, D. Kipke, and R. Brown, “Iridium oxide reference electrodes for neurochemical sensing with MEMS microelectrode arrays,” in *Proceedings of IEEE Sensors 2005*, Irvine, CA, Oct. 2005.

[Franklin07] R.K. Franklin, S.M. Martin and T.D. Strong, R.B. Brown, “Chemical and Biological Systems: Chemical Sensing for Liquids,” in *Comprehensive Microsystems*, Y.B. Gianchandani, O. Tabata, H. Zappe (eds.) Oxford: Elsevier Ltd, vol. 2, pp. 433-462, 2007.

[Franklin09] R. Franklin, S. Negi, F. Solzbacher, and R. Brown, “A Comparison of Fabrication Methods for Iridium Oxide Reference Electrodes,” in *Proceedings of IEEE Sensors 2009*, Christchurch, NZ, Oct. 2009.

[Fried99] I. Fried, C.L. Wilson, N.T. Maidment, J. Engel Jr, E. Behnke, T.A. Fields, K.A. MacDonald, J.W. Morrow, L. Ackerson, “Cerebral microdialysis combined with single-neuron and electroencephalographic recording in neurosurgical patients. Technical note,” *J Neurosurg*, vol. 91, pp. 697-705, 1999.

[Gaddum61] J. Gaddum, “Push-pull cannulae,” Journal of Physiology, vol. 155, p. 1P, 1961.

[Garguilo95] M.G. Garguilo and A.C. Michael, “Enzyme-modified electrodes for peroxide, choline, and acetylcholine,” *Trac-Trends in Analytical Chemistry*, vol. 14, pp. 164-169, 1995.

[Garris94] P.A. Garris, E.L. Ciolkowski, and R.M. Wightman, “Heterogeneity of evoked dopamine overflow within the striatal and striatoamygdaloid regions,” *Neuroscience*, vol. 59, pp. 417-27, 1994.

[Garris97] P.A. Garris, J.R. Christensen, G.V. Rebec, and R.M. Wightman, “Real-time measurement of electrically evoked extracellular dopamine in the striatum of freely moving rats,” *J Neurochem*, vol. 68, pp. 152-61, 1997.

[Gerfen96] C.R. Gerfen and C.J. Wilson, “The basal ganglia,” in *Handbook of Chemical Neuroanatomy*, Vol. 12, Integrated Systems of the CNS, Part III, L.W. Swanson, A. Bjorklund, and T. Hokfelt, Eds., London: Elsevier, pp. 371-468, 1996.

[Gerhardt84] G.A. Gerhardt, A.F. Oke, G. Nagy, B. Moghaddam, and R.N. Adams, “Nafion-coated electrodes with high selectivity for CNS electrochemistry,” *Brain Res*, vol. 290, pp. 390-5, 1984.

[Gerhardt01] G.A. Gerhardt and A.F. Hoffman, “Effects of recording media composition on the responses of Nafion-coated carbon fiber microelectrodes measured using high-speed chronoamperometry,” *J Neurosci Methods*, vol. 109, pp. 13-21, 2001.

[Gervasoni04] D. Gervasoni, S.C. Lin, S. Ribeiro, E.S. Soares, J. Pantoja, and M.A. Nicolelis, “Global forebrain dynamics predict rat behavioral states and their transitions,” *J Neurosci,* vol. 24, pp. 11137-47, 2004.

[Ges05] I.A. Ges, B.L. Ivanov, D.K. Schaffer, E.A. Lima, A.A. Werdich, and F.J. Baudenbacher, “Thin-film IrO_X pH microelectrode for microfluidic-based microsystems,” *Biosensors and Bioelectronics*, vol. 21, no. 2, p. 248, 2005.

[Ghasemzadeh91] B. Ghasemzadeh, J. Cammack, R.N. Adams, and B. Ghasemzedah, “Dynamic changes in extracellular fluid ascorbic acid monitored by in vivo electrochemistry,” *Brain Res*, vol. 547, pp. 162-166, 1991.

[Ghosh08] A. Ghosh, R. Rao, Ching-Te Chuang, and R. Brown, “On-Chip Process Variation Detection and Compensation Using Delay and Slew-Rate Monitoring Circuits,” in Proceedings of Quality Electronic Design 2008, 9th International Symposium on, pp. 815-820, 2008.

[Ghosh10] A. Ghosh, R. K. Franklin, and R. B. Brown, “Analog Circuit Design Methodologies to Improve Negative-Bias Temperature Instability Degradation,” in Proceedings of VLSI Design 2010, 23rd International Conference on, January 2010.

[Gielen05] G. Gielen, W. Dehaene, P. Christie, D. Draxelmayr, E. Janssens, K. Maex, and T. Vucurevich, “Analog and Digital Circuit Design in 65 nm CMOS: End of the Road?,” Proceedings of the conference on Design, Automation and Test in Europe - Volume 1, IEEE Computer Society, pp. 36-42, 2005.

[Gielen06] G. Gielen, “Design methodologies and tools for circuit design in CMOS nanometer technologies,” Solid-State Device Research Conference, 2006. ESSDERC 2006. Proceeding of the 36th European, pp. 21-32, 2006.

[Glowinski66] J. Glowinski and L.L. Iversen, “Regional studies of catecholamines in the rat brain. I. The disposition of [3-H] norepinephrine, [3-H] dopamine and [3-H] dopa in various regions of the brain,” *J Neurochem*, vol. 13, pp. 655-69, 1966.

[Hammond07] C. Hammond, H. Bergman, and P. Brown, “Pathological synchronization in Parkinson’s disease: networks, models and treatments,” *Trends Neurosci*, vol. 30, pp. 357-64, 2007.

[Hefti83] F. Hefti and D. Felix, “Chronoamperometry in vivo: does it interfere with spontaneous neuronal activity in the brain?,” *J Neurosci Methods*, vol. 7, pp. 151-6, 1983.

[Hetke94] J.F. Hetke, J.L. Lund, K. Najafi, K.D. Wise, and D.J. Anderson, “Silicon ribbon cables for chronically implantable microelectrode arrays,” *IEEE Trans Biomed Eng*, vol. 41, pp. 314-321, 1994.

[Hetke02] J.F. Hetke and D.J. Anderson, “Silicon microelectrodes for extracellular recording,” in *Handbook of Neuroprosthetic Methods*, W.E. Finn and P.G. LoPresti, Eds., Boca Raton, FL: CRC Press, 2002.

[Hitchman88] M.L. Hitchman and S. Ramanathan, “Evaluation of iridium oxide electrodes formed by potential cycling as pH probes,” *The Analyst*, vol. 113, pp. 35-39, 1988.

[Hu94] Y. Hu, K.M. Mitchell, F.N. Albahadily, E.K. Michaelis, and G.S. Wilson, “Direct measurement of glutamate release in the brain using a dual enzyme-based electrochemical sensor,” *Brain Res*, vol. 659, pp. 117-25, 1994.

[Huang02] I. Huang, R. Huang, “Fabrication and characterization of a new planar solid-state reference electrode for ISFET sensors”, *Thin Solid Films*, vol. 406, 255-261, 2002.

[Ikeda85] M. Ikeda, H. Miyazaki, and A. Matsushita, “Simultaneous monitoring of electrochemical and unitary neuronal activities by a single carbon fiber microelectrode,” *Jpn J Pharmacol*, vol. 37, pp.303-5, 1985.

[Intel09] Intel, “Intel Unveils 45nm System-on-Chip for Internet TV,” Intel Corporation, Santa Clara, CA, Press Release, Sept. 24 2009. [Online] Available: http://www.intel.com/press-room/archive/releases/20090924 comp_b.htm. [Accessed: Oct. 14, 2009].

[Johnson03] M.D. Johnson, J.C. Williams, M. Holecko, and D.R. Kipke, “Chemical sensing capability of MEMS implantable multichannel neural microelectrode arrays,” *Proceedings of the IEEE Engineering in Medicine and Biology Society*, vol. 4, pp. 3333-3336, 2003.

[Johnson05] M.D. Johnson, R.K. Franklin, K.A. Scott, R.B. Brown, and D.R. Kipke, “Neural probes for concurrent detection of neurochemical and electrophysiological signals in vivo,” in *Proceedings of the IEEE Engineering in Medicine and Biology Society*, vol. 1, pp. 7325-8, 2005.

[Johnson05B] M. D. Johnson, K. J. Otto, and D. R. Kipke, “Repeated voltage biasing improves unit recordings by reducing resistive tissue impedances,” *IEEE Trans Neural Syst Rehabil Eng*, vol. 13, 2005.

[Johnson06] M. Johnson, N. Langhals, and D. Kipke, “Neural interface dynamics following insertion of hydrous iridium oxide microelectrode arrays,” in *Proceedings of the IEEE Engineering in Medicine and Biology Society,* pp. 3178-3181, 2006.Tae13bo.

[Johnson07] M.D. Johnson, O.E. Kao, and D.R. Kipke, “Spatiotemporal pH dynamics following insertion of neural microelectrode arrays,” *J Neurosci Methods*, vol. 160, pp. 276-87, 2007.

[Johnson08] M.D. Johnson, R.K. Franklin, M.D. Gibson, R.B. Brown, and D.R. Kipke, “Implantable microelectrode arrays for simultaneous electrophysiological and neurochemical recordings,” Journal of Neuroscience Methods, vol. 174, pp. 62-70, 2008.

[Justice87] J.B. Justice, *Voltammetry in the neurosciences: principles, methods, and applications*. Clifton, NJ: Humana Press, 1987.

[Kawagoe93] K.T. Kawagoe, J.B. Zimmerman, and R.M. Wightman, “Principles of voltammetry and microelectrode surface states,” *J Neurosci Methods*, vol. 48, pp. 225-40, 1993.

[Kawagoe94] K.T. Kawagoe and R.M. Wightman, “Characterization of amperometry for in vivo measurement of dopamine dynamics in the rat brain,” *Talanta*, vol. 41, pp. 865-74, 1994.

[Kellis09] S. Kellis, N. Gaskin, and P. House, “An Embedded System for Neural Prosthetics,” The 17th IFIP/IEEE International Conf. on VLSI (VLSI-SoC), Florianopolis, Brazil: October 2009.

[Kissinger73] P.T. Kissinger, J.B. Hart, and R.N. Adams, “Voltammetry in brain tissue--a new neurophysiological measurement,” *Brain Res*, vol. 55, pp. 209-13, 1973.

[Kissinger96] P.T. Kissinger, C. Preddy, R. Shoup, and W. Heineman, “Laboratory techniques in electroanalytical chemistry, 2nd edn. revised and expanded.” P. Kissinger and W. Heinerman (eds.). New York, NY: Marcel Dekker, Inc., 1996

[Lee03] K.H. Lee, L.M. Williams, M. Breakspear, and E. Gordon, “Synchronous gamma activity: a review and contribution to an integrative neuroscience model of schizophrenia,” *Brain Res Rev*, vol. 41, pp. 57-78, 2003.

[Lewyn09] L.L. Lewyn, T. Ytterdal, C. Wulff, and K. Martin, “Analog Circuit Design in Nanoscale CMOS Technologies,” *Proceedings of the IEEE*, vol.97, no.10, pp.1687-1714, 2009.

[Liu98] Song Liu and R. Baker, “Process and temperature performance of a CMOS beta-multiplier voltage reference,” Circuits and Systems, 1998. Proceedings. 1998 Midwest Symposium on, pp. 33-36, 1998.

[Logothetis01] N.K. Logothetis, J. Pauls, M. Augath, T. Trinath, and A. Oeltermann, "Neurophysiological investigation of the basis of the fMRI signal," *Nature*, vol. 412, pp. 150-7, 2001.

[Ludvig92] N. Ludvig, P.K. Mishra, Q.S. Yan, S.M. Lasley, R.L. Burger, and P.C. Jobe, "The combined EEG- intracerebral microdialysis technique: a new tool for neuropharmacological studies on freely behaving animals," *J Neurosci Methods*, vol. 43, pp. 129-37, 1992.

[Magill06] P.J. Magill, A. Pogosyan, A. Sharott, J. Csicsvari, J.P. Bolam, and P. Brown, "Changes in functional connectivity within the rat striatopallidal axis during global brain activation in vivo," *J Neurosci*, vol. 26, pp. 6318-29, 2006.

[Maloney05] J.M. Maloney, S.A. Lipka, and S.P. Baldwin, "In Vivo Biostability of CVD Silicon Oxide and Silicon Nitride Films" in *Micro- and Nanosystems—Materials and Devices*, C.S. Ozkan, D.A. LaVan, M. McNie, and S. Prasad (eds), vol 872, Warrendale, PA: Mater. Res. Soc., pp. J14.3, 2005.

[Marsden84] C.A. Marsden, *Measurement of Neurotransmitter Release In Vivo*, New York: Wiley; 1984.

[Marsman06] E. Marsman, R. Senger, G. Carichner, S. Kubba, M. McCorquodale, and R. Brown, "DSP architecture for cochlear implants," Circuits and Systems, 2006. ISCAS 2006. Proceedings. 2006 IEEE International Symposium on, pp. 657-660, 2006

[Martin03] S.M. Martin, R.M. Senger, E.D. Marsman, F.H. Gebara, M.S. McCorquodale, K.L. Kraver, M.R. Guthaus, and R.B. Brown, "A Low-Power Microinstrument for Chemical Analysis of Remote Environments," NASA Symposium on VLSI Design, Coeur d'Alene, Idaho, May 28-29, 2003, pp. 1-4.

[Martin05] S.M. Martin, "CMOS-Integrated Liquid Chemical Microdetection Systems," Ph.D. Dissertation, University of Michigan, Ann Arbor, MI, 2005.

[Martin09] S. Martin, F. Gebara, T. Strong, and R. Brown, "A Fully Differential Potentiostat," *Sensors Journal, IEEE*, vol. 9, pp. 135-142, 2009.

[Marzouk98] S.A.M. Marzouk, S. Ufer, R.P. Buck, T.A. Johnson, L.A. Dunlap, and W.E. Cascio, “Electrodeposited Iridium Oxide pH Electrode for Measurement of Extracellular Myocardial Acidosis during Acute Ischemia,” Analytical Chemistry, vol. 70, pp. 5054-5061, 1998.

[May89] L.J. May and R.M. Wightman, “Heterogeneity of stimulated dopamine overflow within rat striatum as observed with in vivo voltammetry,” *Brain Res*, vol. 487, pp. 311- 20, 1989.

[McNamara94] J.O. McNamara, “Cellular and molecular basis of epilepsy,” *J Neurosci,* vol. 14, pp. 3413- 25, 1994.

[McNaught97] A.D. McNaught, A. Wilkinson, *Compendium of Chemical Terminology*, Malden, MA: Blackwell Science, 1997.

[Meyer01] R.D. Meyer, S.E. Cogan, T.H. Nguyen, and R.D. Rauh, “Electrodeposited iridium oxide for neural stimulation and recording electrodes,” *IEEE Transactions on Neural Systems and Rehabilitation Engineering*, vol. 9, no. 1, 2001, 2-11.

[Michael87] A.C. Michael and M. Ikeda, “Justice Jr JB. Mechanisms contributing to the recovery of striatal releasable dopamine following MFB stimulation,” *Brain Res,* vol. 421, pp. 325-35, 1987.

[Mitala06] J. Mitala Jr. and A. Michael, “Improving the performance of electrochemical microsensors based on enzymes entrapped in a redox hydrogel,” *Analytica Chimica Acta*, vol. 556, pp. 326-332, 2006.

[Mitzdorf85] U. Mitzdorf, “Current source-density method and application in cat cerebral cortex: investigation of evoked potentials and EEG phenomena,” *Physiol Rev*, vol. 65, pp. 37-100, 1985.

[Moussy94] F. Moussy and D.J. Harrison, “Prevention of the rapid degradation of subcutaneously implanted ag/agcl reference electrodes using polymer coatings,” *Anal Chem*, vol. 66, no. 5, pp. 674-9, 1994.

[Mukamel05] R. Mukamel, H. Gelbard, A. Arieli, U. Hasson, I. Fried, and R. Malach, “Coupling between neuronal firing, field potentials, and FMRI in human auditory cortex,” *Science*, vol. 309, pp. 951-4, 2005.

[Najafi90] K. Najafi, J. Ji, and K.D. Wise, “Scaling limitations of silicon multichannel recording probes,” *IEEE Trans Biomed Eng,* vol. 37, pp. 1-11, 1990.

[Nam03] H. Nam, G.S. Cha, T.D. Strong, J. Ha, J.H. Sim, R.W. Hower, S.M. Martin, and R.B. Brown, “Micropotentiometric sensors,” *Proceedings of the IEEE*, vol. 91, pp. 870-80, 2003.

[Niessing05] J. Niessing, B. Ebisch, K.E. Schmidt, M. Niessing, W. Singer, and R.A. Galuske, “Hemodynamic signals correlate tightly with synchronized gamma oscillations,” *Science*, vol. 309, pp. 948-51, 2005.

[Nieuwenhuys82] R. Nieuwenhuys, L.M. Geeraedts, and J.G. Veening, “The medial forebrain bundle of the rat. I. General introduction,” *J Comp Neurol*, vol. 206, pp.49-81, 1982.

[Obrenovitch93] T.P. Obrenovitch, D.A. Richards, G.S. Sarna, and L. Symon, “Combined intracerebral microdialysis and electrophysiological recording: methodology and applications,” *J Neurosci Methods*, vol. 47, pp. 139-45, 1993.

[Paxinos05] G. Paxinos and C. Watson, “The rat brain in stereotaxic coordinates,” *Burlington: Elsevier Academic*; 2005.

[Pellinen05] Pellinen DS, Moon T, Vetter RJ, Miriani R, and Kipke DR. “Multifunctional flexible parylene-based intracortical microelectrodes.” Proceedings of the 27th International IEEE-EMBS Conference, Shanghai, China, pp. 5272-5275. 2005.

[Pennington04] J.M. Pennington, J.C.P. Millar, L.J. Owesson, C.A. McLaughlin, and D.P.J.A. Stamford, “Simultaneous real-time amperometric measurement of catecholamines and serotonin at carbon fibre ‘dident’ microelectrodes,” *J Neurosci Methods*, vol. 140, pp. 5-13, 2004.

[Perlin09] G. Perlin and K. Wise, “Ultra-compact integration for fully-implantable neural microsystems,” 22nd IEEE International Conference on Micro Electro Mechanical Systems, MEMS 2009, January 25, 2009 - January 29, 2009, Sorrento, Italy, pp. 228-231.

[Peters00] J.L. Peters and A.C. Michael, “Changes in the kinetics of dopamine release and uptake have differential effects on the spatial distribution of extracellular dopamine concentration in rat striatum,” *J Neurochem*, vol. 74, pp. 1563-73, 2000.

[Phillips03] P.E.M. Phillips and R.M. Wightman, “Critical guidelines for validation of the selectivity of in-vivo chemical microsensors,” *Trac-Trends in Analytical Chemistry*, vol. 22, pp. 509-514, 2003.

[Pothos91] E. Pothos, P. Rada, G.P. Mark, and B.G. Hoebel, “Dopamine microdialysis in the nucleus accumbens during acute and chronic morphine, naloxone-precipitated withdrawal and clonidine treatment,” *Brain Research*, vol. 566, pp. 348-350, Dec. 1991.

[Rathnasingham04] R. Rathnasingham, D.R. Kipke, S.C. Bledsoe, and J.D. McLaren, “Characterization of implantable microfabricated fluid delivery devices,” *IEEE Trans. in Bio. Eng.*, vol. 51, pp. 138-145, 2004.

[Robinson91] T.E. Robinson and J.B. Justice, *Microdialysis in the neurosciences*. Amsterdam; New York: Elsevier, 1991.

[Roham08] M. Roham, J.M. Halpern, H.B. Martin, H.J. Chiel, and P. Mohseni, “Wireless amperometric neurochemical monitoring using an integrated telemetry circuit,” IEEE Transactions on Bio-Medical Engineering, vol. 55, pp. 2628-2634, Nov. 2008.

[Sawyer95] D.T. Sawyer, A. Sobkowiak, L. Julian, and J.L. Roberts Jr., *Electrochemistry for Chemists* New York, NY: Wiley, 1995

[Schultz07] W. Schultz, “Multiple dopamine functions at different time courses,” *Annu Rev Neurosci*, vol. 30, pp. 259-88, 2007.

[Schwartz06] A.B. Schwartz, X.T. Cui, D.J. Weber, and D.W. Moran, “Brain-controlled interfaces: movement restoration with neural prosthetics,” *Neuron*, vol. 52, pp.205-20, 2006.

[Senger03] R.M. Senger, E.D. Marsman, M.S. McCorquodale, F.H. Gebara, K.L. Kraver, M.R. Guthaus, and R.B. Brown, “A 16-bit mixed-signal microsystem with integrated CMOS-MEMS clock reference,” Proceedings of the 40th annual Design Automation Conference, Anaheim, CA, USA: ACM, 2003, pp. 520-525.

[Senger06] R.M. Senger, E.D. Marsman, M.S. McCorquodale, and R.B. Brown, “A 16-bit, low-power microsystem with monolithic MEMS-LC clocking,” Proceedings of the 2006 Asia and South Pacific Design Automation Conference, Yokohama, Japan: IEEE Press 2006, pp. 94-95.

[Shin01] J.H. Shin, Y.S. Choi, H.J. Lee, S.H. Choi, J. Ha, I.J. Yoon, H. Nam, and G.S. Cha, “A planar amperometric creatinine biosensor employing an insoluble oxidizing agent for removing redox-active interferences,” *Anal. Chem*, vol. 73, no. 24, pp. 5965-5971, 2001.

[Shin04] J.H. Shin, H.L. Lee, S.H. Cho, J. Ha, H. Nam, and G.S. Cha, “Characterization of Epoxy Resin-Based Anion-Responsive Polymers: Applicability to Chloride Sensing in Physiological Samples,” Analytical Chemistry, vol. 76, pp. 4217-4222, July 2004.

[Slavcheva04] E. Slavcheva, R. Vitushinsky, W. Mokwa, and U. Schnakenberg, “Sputtered iridium oxide films as charge injection material for functional electrostimulation,” *Journal of The Electrochemical Society*, vol. 151, no. 7, pp. E226, 2004.

[Sreenivas96] G. Sreenivas, S.S. Ang, I. Fritsch, W.D. Brown, G.A. Gerhardt, and D.J. Woodward, “Fabrication and characterization of sputtered-carbon microelectrode arrays,” *Anal Chem*, vol. 68, pp. 1858-64, 1996.

[Stamford86] J.A. Stamford, “In vivo voltammetry: some methodological considerations,” *J Neurosci Methods*, vol. 17, pp. 1-29, 1986.

[Stamford93] J.A. Stamford, P. Palij, C. Davidson, C.M. Jorm, and J. Millar, “Simultaneous real-time electrochemical and electrophysiological recording in brain-slices with a single carbon-fiber microelectrode,” *J Neurosci Methods*, vol. 50, pp. 279-290, 1993.

[Stensaas78] S.S. Stensaas and L.J. Stensaas, “Histopathological evaluation of materials implanted in cerebral-cortex,” *Acta Neuropathologica*, vol. 41, pp. 145-155, 1978.

[Stork06] J. Stork, “Balancing SoC Design and Technology Challenges at 45nm,” VLSI Technology, 2006. Digest of Technical Papers. 2006 Symposium on, 2006, pp. 1-2.

[Strong01] T.D.Strong, H.C. Cantor, and R.B. Brown, “A microelectrode array for real-time neurochemical and neuroelectrical recording in vitro”, *Sensors and Actuators A: Physical*, vol. 91, no. 3, pp. 357-362, 2001.

[Strong04] T.D. Strong, “Microfabricated Voltammetric Neuro-arrays for Use in vitro,” Ph.D. Dissertation, University of Michigan, Ann Arbor, MI, 2004.

[Su90] M.T. Su, T.V. Dunwiddie, and G.A. Gerhardt, “Combined electrochemical and electrophysiological studies of monoamine overflow in rat hippocampal slices,” *Brain Res*, vol. 518, pp. 149-58, 1990.

[Tierney09] S. Tierney, B.M. Hasle-Falch, D.R. Hjelme, and B.T. Stokke, “Determination of glucose levels using a functionalized hydrogel-optical fiber biosensor: Toward continuous monitoring of blood glucose in vivo,” *Analytical Chemistry*, vol. 81, pp. 3630-3636, 2009.

[Toner96] C.C. Toner and J.A. Stamford, “‘Real time’ measurement of dopamine release in an in vitro model of neostriatal ischaemia, *J Neurosci Methods*, vol. 67, no. 2, pp. 133-40, 1996.

[Ungerstedt91] U. Ungerstedt, “Introduction to intracerebral microdialysis,” Microdialysis in the Neurosciences, T.E. Robinson and J.B. Justice, eds., New York: Elsevier Science Publishers, 1991, pp. 3-18.

[van Horne90] C.G. van Horne, S. Bement, B.J. Hoffer, and G.A. Gerhardt, “Multichannel semiconductor-based electrodes for in vivo electrochemical and electrophysiological studies in rat CNS,” *Neurosci Lett*, vol. 120, pp. 249-52, 1990.

[Venton03] B.J. Venton, H. Zhang, P.A. Garris, P.E. Phillips, D. Sulzer, and R.M. Wightman, “Real-time decoding of dopamine concentration changes in the caudate-putamen during tonic and phasic firing,” *J Neurochem*, vol. 87, pp. 1284-95, 2003.

[Vetter04] R.J. Vetter, J.C. Williams, J.F. Hetke, E.A. Nunamaker, and D.R. Kipke, “Chronic neural recording using silicon-substrate microelectrode arrays implanted in cerebral cortex,” *IEEE Trans Biomed Eng*, vol. 51, pp. 896-904, 2004.

[Wang99] J. Wang, “Amperometric biosensors for clinical and therapeutic drug monitoring: a review,” *J Pharm Biomed Anal*, vol. 19, pp. 47-53, 1999.

[Weiland00] J.D. Weiland and D.J. Anderson, “Chronic neural stimulation with thin-film, iridiumoxide electrodes,” *IEEE Trans Biomed Eng*, vol. 47, no. 7, pp. 911-8, 2000.

[Weiland02] J.D. Weiland, D.J. Anderson, and M.S. Humayun, “In vitro electrical properties for iridiumoxide versus titanium nitride stimulating electrodes,” *IEEE Trans Biomed Eng*, vol. 49, no. 12Pt 2, pp. 1574-9, 2002.

[Westerink88] B.H. Westerink and J.B. De Vries, “Characterization of in vivo dopamine release as determined by brain microdialysis after acute and subchronic implantations: methodological aspects,” *J Neurochem*, vol. 51, pp. 683-7, 1988.

[Wightman88] R.M. Wightman, C. Amatore, R.C. Engstrom, P.D. Hale, E.W. Kristensen, W.G. Kuhr, L.J. May, “Real-time characterization of dopamine overflow and uptake in the rat striatum,” *Neuroscience*, vol. 25, pp. 513-23, 1988.

[Wightman90] R.M. Wightman and J.B. Zimmerman, “Control of dopamine extracellular concentration in rat striatum by impulse flow and uptake,” *Brain Res*, vol. 15, pp. 135-44, 1990.

[Williams90] G.V. Williams and J. Millar, “Concentration-dependent actions of stimulated dopamine release on neuronal activity in rat striatum,” *Neuroscience,* vol. 39, pp. 1-16, 1990.

[Wise70] K.D. Wise, J.B. Angell, and A. Starr, “An integrated-circuit approach to extracellular microelectrodes,” *IEEE Trans Biomed Eng*, vol. 17, pp. 238-47, 1970.

[Wise71] K.D. Wise and J.B. Angell, “A Microprobe with Integrated Amplifiers for Neurophysiology,” IEEE Int. Solid-State Circuits Conf., 1971, pp. 100-1.

[Wise04] K.D. Wise, D.J. Anderson, J.F. Hetke, D.R. Kipke, and K. Najafi, “Wireless implantable microsystems: high-density electronic interfaces to the nervous system,” *P IEEE*, vol. 92, pp. 76-97, 2004.

[Wise08] K.D. Wise, A.M. Sodagar, Y. Ying, M.N. Gulari, G.E. Perlin, and K. Najafi, “Microelectrodes, Microelectronics, and Implantable Neural Microsystems,” *Proceedings of the IEEE*, vol. 96, 2008, pp. 1184-1202.

[Wise09] K. Wise, G. Perlin, Y. Ying, K. Najafi, and A. Sodagar, “An Implantable 64-channel wireless microsystem for single-unit neural recording,” *IEEE J Solid-State Circuits*, vol. 44, Sept. 2009, pp. 2591-604.

[Yang03] H. Yang, S.K. Kang, D.H. Shin, H. Kim, and Y.T. Kim, “Microfabricated iridium oxide reference electrode for continuous glucose monitoring sensor,” in *Proceedings of Transducers, Solid-State Sensors, Actuators and Microsystems*, 2003, vol. 1, pp. 103-106.

[Yang04 H. Yang, S.K. Kang, C.A. Choi, H. Kim, D.H. Shin, Y.S. Kim, and Y.T. Kim, “An iridium oxide reference electrode for use in microfabricated biosensors and biochips,” *Lab Chip*, vol. 4, pp. 42-6, 2004.

[Yavich00] L. Yavich and J. Tiihonen, “In vivo voltammetry with removable carbon fibre electrodes in freely-moving mice: dopamine release during intracranial self-stimulation,” Journal of Neuroscience Methods, vol. 104, Dec. 2000, pp. 55-63.

[Yeomans88] J.S. Yeomans, N.T. Maidment, and B.S. Bunney, “Excitability properties of medial forebrain bundle axons of A9 and A10 dopamine cells,” *Brain Res*, vol. 450, pp. 86-93, 1988.

[Yu00] P.G. Yu and G.S. Wilson, “An independently addressable microbiosensor array: what are the limits of sensing element density?” *Faraday Discuss*, pp. 305-17, 2000.

[Yuen83] M.F. Yuen, I. Lauks, and W.C. Dautremont-Smith, “pH dependent voltammetry of iridium oxide films,” *Solid State Ionics*, vol. 11, Sept. 1983, pp. 19-29.

[Ziaie96] B. Ziaie, J.A. VonArx, and K. Najafi, “Micro-fabricated planar high current irox stimulating microelectrode,” in *Proceedings of the IEEE Engineering in Medicine and Biology Society*, 1996, p. 270.